Surface and Interfacial Studies of Perovskite Oxides Grown by Hybrid Molecular Beam Epitaxy

By

Suresh Thapa

A dissertation submitted to the Graduate Faculty of
Auburn University
in partial fulfillment of the
requirements for the Degree of
Doctor of Philosophy

Auburn, Alabama
May 7, 2022

Keywords: hMBE, RHEED, XPS, XRD, AFM, STO, SNO

Approved by

Ryan Bradley Comes, Chair, Assistant Professor, Department of Physics
Marcelo Kuroda, Associate Professor, Department of Physics
Michael W Gramlich, Assistant Professor, Department of Physics
Wencan Jin, Assistant Professor, Department of Physics
Masoud Mahjouri-Samani, Assistant Professor, Department of Electrical Engineering

Abstract

Perovskite oxides are well known for their intriguing properties such as ferroelectricity, ferromagnetism, and superconductivity that can be tuned by different crystalline degrees of freedom. $SrTiO_3$ (STO) is a perovskite oxide with simple cubic structure which is compared to the silicon in the semiconductor field because of its suitable lattice parameter for widespread use as a substrate in thin-film perovskite oxide growth. In an STO-based system, photocatalytic capabilities are discovered in addition to the discovery of a quasi two-dimensional electron gas (2DEG). Previous work has shown that STO surface properties determine its applicability for catalytic and interfacial behavior. $SrNbO_3$ (SNO) is another interesting cubic perovskite oxide with lattice parameter of 4.0 Å is known for its strong electron donor capability and photocatalytic behavior. Recent reports on the strain-induced breaking of cubic symmetry of SNO producing large mobilities and large magnetoresistance and mobility in SNO/STO interface open the opportunity for SNO as a topological and quantum material. However, SNO synthesis is challenging due to the metastable nature of the d^1 Nb^{4+} cation and the limitations in the delivery of refractory niobium. This work focuses on the synthesis of SNO thin films by hybrid molecular beam epitaxy (hMBE) to address the growth challenges and application in high mobility 2DEGs.

A thin-film deposition technique, hMBE, in which transition metal cations are delivered using a metal-organic precursor, has emerged as the state-of-the-art approach to the synthesis of electronic-grade complex oxide films with a stoichiometric growth window. High-quality epitaxial STO and SNO thin films were grown on multiple substrates by hMBE approach. To address numerous unanswered questions regarding the chemical mechanisms of the growth process and

the surface properties of the resulting films, STO thin films were prepared on annealed STO and Nb-doped STO substrates by hMBE. While synthesizing STO thin film, a titanium tetraisopropoxide (TTIP) precursor used for Ti delivery and an elemental Sr source with varying TTIP:Sr flux ratios to examine the conditions for the reported stoichiometric growth window. This work demonstrates the growth of SNO thin films by hMBE for the first time using a tris(diethalamido)(tert-butylimido) niobium precursor for niobium. An elemental Sr source is used for supplying strontium and the synthesis is carried out on $GdScO_3$ and as prepared $BaSnO_3$ (BSO) films on Nb-doped STO substrates. To examine the preservation of the Nb $4d^1$ metastable charge state in atmospheric conditions, an insulating $SrHfO_3$ capping layer was deposited on top of SNO films. Furthermore, the charge transfer mechanism in the SNO/BSO interface is investigated by first-principles density functional theory and angle-resolved X-ray photoelectron spectroscopy to shed light on the possibility of high mobility 2DEG.

Acknowledgments

This long journey at Auburn University that led to this dissertation would not have been possible without the support and assistance from family, friends, mentors, and collaborators. I owe a debt of gratitude to each of these individuals for their contributions.

First and foremost, I would like to express my gratitude to Prof. Ryan Comes, who guided me during my stay at Auburn. I consider myself extremely privileged to have had the opportunity to work with Professor Ryan Comes on my Ph.D. research. He has always guided me to become a successful and competent professional in all aspects of research and life. He has been incredibly encouraging and supportive, giving me helpful feedback on my work and advice on how to address challenges in the lab. I have learned a lot from his leadership skills, which will help me throughout my career. Working with Dr. Comes taught me how to be an independent researcher, a troubleshooter, and a project leader. He has always radiated optimism in all aspects of research and life since the day I joined his research group. During my recent job search, his guidance and comments made the process more efficient. This project would not have been possible without his continuous support and encouragement, which has been invaluable. Thank you very much for all that you have done!

I would like to thank all my advisory committee members: Prof. Marcelo Kuroda, Prof. Michael W Gramlich, Prof. Wencan Jin and Prof. Masoud Mahjouri Samani for their significant contribution to this work. I am indebted to Prof. Marcelo Kuroda for his guidance on modeling

DFT calculations. Prof. Wencan Jin has always been a pleasure to talk to, and I am grateful for his insights into decision-making during critical experiments. I am thankful to Prof. Michael W Gramlich for helpful comments during my PhD proposal defense which helped me to better shape my dissertation.

Without the help of collaborators from other universities and national facilities, this project would not have been possible. During my visit to Brookhaven National Laboratory, I am grateful to Dr. Jerzy Sadwosky for performing LEED and LEEM measurements on my samples. I am indebted to Dr. Matthew Brahlek and Dr. Jason Lapano for HR-XRD measurements. Prof. Petra Reinka and her graduate student Devin Jessup from the University of Virginia conducted STM measurements to complete the story of my first lead author article, and I'd like to express my gratitude to them. Steve Heald from Argonne National Laboratory made a significant contribution to one of our ambitious projects by conducting XANES measurements on $SrNbO_3$ sample. Prof. Darrell Scholm and Dr. Hanjong Piak at Cornell University deserve special thanks for preparing BSO samples that allowed us to study interfacial charge transfer in the BSO/SNO interface. I'd like to express my gratitude to Prof. Boris Keifer of New Mexico State University and his graduate student Mr. Sharad Mahatara for their exceptional contributions to DFT modeling of the BSO/SNO heterostructure for interfacial charge transfer.

I'd like to express my heartfelt gratitude to everyone who made Auburn feel like home. I'd want to thank the Auburn University faculty and staff personnel who have taught, trained, and assisted me throughout my research and physics studies. I'm grateful to all of my friends who have supported me throughout my life, from childhood to graduate school. Dr. Sydney Provence's cooperation has

been invaluable in running the lab and troubleshooting technical issues as they arise. Mr. Miles Blanchet, Mr. Rajendra Paudel, Mr. Uchenna Ubeh, Mr. Patrick Gemperline, and Mr. Jibril Ahammad are some of my very helpful friends who have assisted me in a variety of ways to complete this work as quickly as possible.

Above all, my heartfelt gratitude and appreciation go to my loving parents, Sundar Thapa and Durga Thapa, who gave me my name, my life, and everything else in between. I adore them and am grateful for the efforts they have made to provide me with the life I have now. They're the reason I'm doing this; they're the reason I want to be a good person. Since my childhood, I have been grateful to my dear sisters Sunita Thapa and Sushma Thapa for their unwavering support.

My two wonderful sons, Yuvaan and Avaan, are another source of inspiration for me to complete my PhD. Yuvaan is a wonderful child to us, and Avaan is a priceless possession. You guys are my inspiration, and I can't thank you enough for being a part of our lives. Last but not least, I want to show my thankfulness to Karishma, my loving, supportive, encouraging, and caring wife. She has always been and continues to be the most encouraging, supportive, and motivational person I have ever met. When it comes to Karishma, there are no words that can express my thanks; I am forever grateful.

There are truly no words to express my gratitude for all of you who have patiently led, supported, and encouraged me throughout my PhD studies. Nonetheless, I attempted to say a few words.

Dedicated to my grandmother
Sita Devi Budhathoki

Table of Contents

List of Figures

List of Abbreviations

MBE	Molecular Beam Epitaxy
hMBE	Hybrid Molecular Beam Epitaxy
XPS	X-ray Photoelectron Spectroscopy
AFM	Atomic Force Microscopy
XRD	X-ray Difraction
LEED	Low Energy Electron Diffraction
LEEM	Low Energy Electron Microscopy
STM	Scanning Tunneling Microscopy
XAS	X-ray Absorption Spectroscopy
XANES	X-ray Absorption Near Edge Spectroscopy
QCM	Quartz Crystal Microbalance
RHEED	Reflection High Energy Electron Diffraction
TTIP	Titanium Tetraisopropoxide
TDTBN	Tris(diethalamido)(tert-butylimido) Niobium
2DEG	2-Dimensional Electron Gas
STO	Strontium Titanate
SNO	Strontium Niobate
Nb:STO	Niobium Doped Strontium Titanate
GSO	Gadolinium Scandate
BSO	Barium Stannate

SSO	Strontium Stannate
SHO	Strontium Hafnate
TSO	Terbium Scandate
CBM	Conduction Band Minimum
VBM	Valence Band Maximum

Chapter 1

Introduction

1.1 Perovskite Oxides

Oxides are ubiquitous, with uses in a wide range of hand-held electronic devices, such as display screens and transistor gate dielectrics. Oxides have a unique set of physical features that suit themselves to electronic applications. These oxides are usually binary, ternary or quaternary. Silicon dioxide (SiO_2) in field-effect devices [1] and indium-tin-oxide ($Sn:In_2O_3$) as transparent conductors [2] are two of the most often utilized binary oxides. Perovskite oxides, among other oxides, have attracted curiosity due to their diverse characteristics and wide applications. Perovskite oxides have a general chemical formula of ABO_3. In this structure, A-site cations are at corners of the cubic unit cell and the B-site cation is at the body center forming octahedra with six face-centered oxygens, as shown in Figure 1.1. In perovskite oxides, A-site cations can be alkali metals (1+ charge), alkaline earth metals (2+ charge), rare earth elements (3+ charge), or lanthanides (3+ charge) while B-site cations are usually transition metals or *p*- block elements such as Al, Sn. These combinations of A-site and B-site cations with oxygen cover almost 70% of the periodic table, making perovskite oxides a large material family [3]. Depending upon A-site cation, B-site cation could possess oxidation state +5 to +3. Due to its simplicity in structure and ease of analysis, the cubic lattice is one of the most widely used perovskite structures to study this material family. Because many perovskite oxides are chemically and structurally compatible, they can be

used to tailor electronic, magnetic, and optical properties in thin films in ways that are not possible in traditional semiconductors.

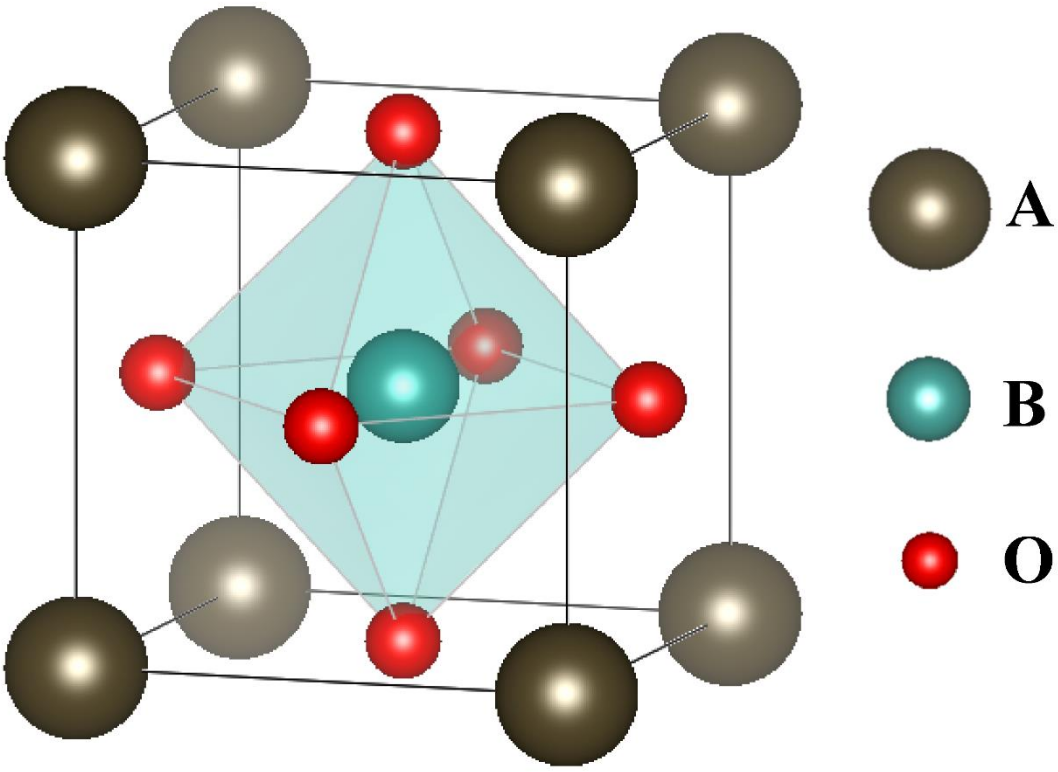

Figure 1.1: Ideal cubic perovskite oxide unit cell structure

Perovskite materials have a wide range of structures and compositions, and they exhibit a wide range of unique properties that have attracted significant interest in many applied and fundamental fields of material science. The Goldschmidt's tolerance factor (*t*) [4] ranges from 0.8 to 1.1 for the perovskite oxide structure to be stable which is related to the ionic radii of A-site cation (r_A), B-site cation (r_B), and oxygen anion (r_O) in the structure as,

$$t = \frac{r_A + r_O}{\sqrt{2}(r_B + r_O)}.$$

This large range of permissible tolerance factors that hold the atomic arrangement together suggests that the BO_6 octahedra can withstand a huge strain. The highest symmetry structure is cubic which has *t* close to 1.0 [5] though only a small number of perovskites have perfect cubic symmetry. If $0.9 < t < 1.0$ is true, the structure is normally cubic, which means there is no structural deformation. If $0.7 < t < 0.9$, the A-site cation is too small to cover the interstitial site, causing the perovskite structure to deform and have a lower symmetry group like orthorhombic or rhombohedral. If *t* is further lower than 0.7, the perovskite structure is no longer stable, and different crystal structures based on the stoichiometry of the compounds begin to develop. As the symmetry lowers another structure appears due to octahedra tilting, distortion, or both. This coupling between structure and ionic size also shows that crystal symmetry of perovskites can be manipulated by doping the A- or B-site with different cations.

1.2 Crystal Degrees of Freedom

Perovskite oxides are well known for their large varieties of properties such as ferromagnetism, ferroelectricity, and superconductivity. Structural deformation along with various degrees of freedom can be used to tailor these properties of a perovskite oxide.

1.2.1 *d*- Orbital Splitting

Many members of the perovskite oxide class are transition metal oxides (TMOs), which have transition metals occupying the B-site. The electrons in the *d*-orbitals control much of the physical and electronic features of TMOs. Hence, the electronic configuration of B-site cation is another

factor that affects the structural distortions in TMOs. Especially, TMOs with odd electron occupancy in *d*-orbitals are of great importance to observe this fine structural distortion. A crystal field created by oxygen octahedra removes the five-fold degeneracy of *d*-orbitals into doubly degenerate and triply degenerate groups. The doubly degenerate sub-group with higher energy is known as e_g orbitals, whereas the triply degenerate sub-group is known as t_{2g} orbitals [6]. However, the filling of electrons in these orbitals is not simple due to the role played by electron spin. A competition between the crystal field splitting parameter (Δ_o) and Hund's coupling energy (H_{ex}) determines the low spin or high spin electronic state of the system while filling electrons in these orbitals. Electrons occupy the lower energy t_{2g} orbitals first when filling these orbitals. After all three orbitals have been filled with one electron each, Δ_o prohibits higher energy e_g orbitals from being occupied and encourages electrons with opposing spins pairing. Hence, the overall spin angular momentum for this configuration is minimum and is known as the low spin state. As soon as the electrons are paired in t_{2g} orbitals, H_{ex} comes into play due to electrostatic repulsion between electrons. If $H_{ex} > \Delta_o$, it is energetically favorable for electrons to fill e_g state before pairing with t_{2g} electrons maximizing total angular momentum. This configuration is called the high spin state. This phenomenon plays a crucial role in determining the ground state properties of TMOs and act as a knob to tune electronic and magnetic properties if H_{ex} and Δ_o are closer. These degeneracies can be further lifted in some perovskite oxides by compressing or stretching the oxygen octahedra. Depending upon the electronic configuration of the *d*-orbitals, low symmetry octahedra are at lower energy than high symmetry octahedra giving distorted octahedra at equilibrium. This type of octahedral distortion is commonly known as Jahn-Teller distortion [7]. As shown in Figure 1.2,

depending on the type of distortion (elongation versus compression), these distortions are accompanied by further splitting of the e_g and t_{2g} orbitals.

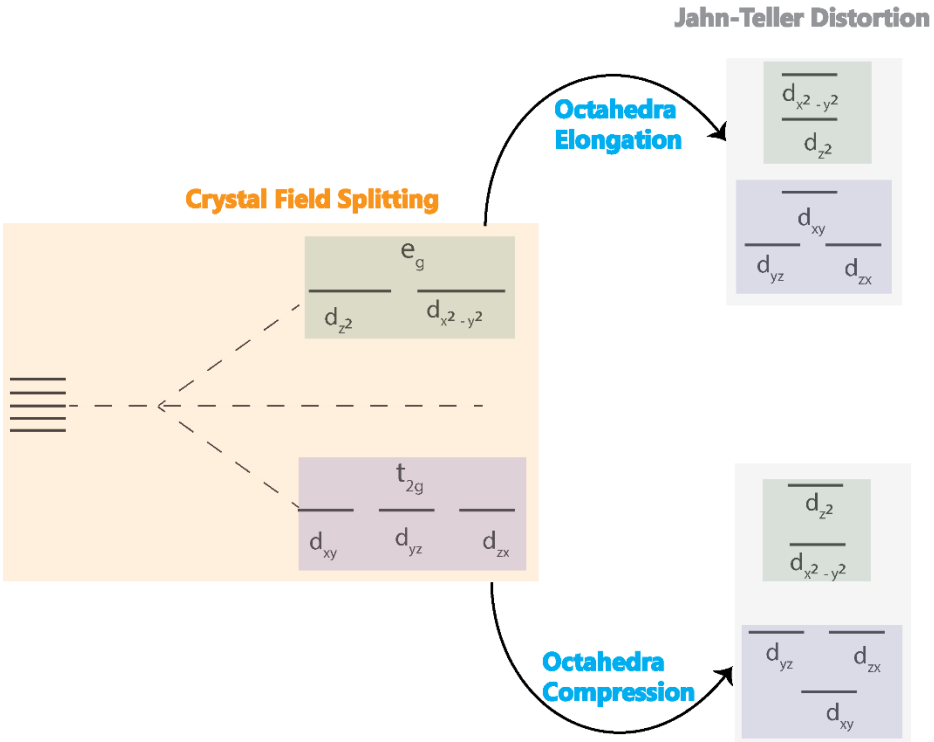

Figure 1.2: Crystal field splitting and Jahn-Teller distortion in d- orbital

1.2.2 Structural Features

Compared to the bulk, thin-film metal oxides must be considered differently due to their vulnerability to the external perturbation such as boundary conditions and point defects, which might be of higher energy and dominates the total energetics of the system that determine the final state of the system. As a result of the interaction between the thin-film material and the external boundary conditions, the crystal structure is distorted to achieve equilibrium. Some of the major structural features observed in perovskite oxide thin films are unit cell expansion/compression,

symmetry breaking through monoclinic/orthorhombic tilting, and oxygen octahedral rotations. The consistent change in lattice dimensions in three orthogonal directions is referred as lattice expansion/compression that results in a change in unit cell volume. For example, $BaTiO_3$ layers are under compressive strain in superlattices strained coherently to a $SrTiO_3$ (STO) substrate, which favors a ferroelectric state with an out-of-plane polarization [8]. When a crystal lattice is under shear deformation, tilting of the lattice takes place. When the deformation occurs along a single crystallographic axis, the tilting is called monoclinic; while if the lattice shears in three crystallographic directions, it is called triclinic. Tilting and bending of oxygen octahedra results in antiferrodistortive structural ordering, can relate to other modes in the system, generating structural and electrical phase changes [9]. Oxygen octahedra rotation on the other hand represents the displacement of the oxygen anion from face center of a unit cell but keeping negligible change octahedral edge length. Hence, this phenomenon is referred also referred as a rotation of the rigid octahedral cage. Many ABO_3 compounds rely heavily on the characteristics of oxygen octahedra. The B-O-B angle is reduced as a result of octahedral rotations, which has significant implications for the magnetic and transport properties of various conducting perovskites. The rare earth nickelate family is one of the most well-known examples for these phenomena, in which the Ni-O-Ni bond angle plays a key role [10].

1.2.3 Effect of Crystal Planes

Despite the structural changes that can be forced in the lattice of perovskite oxide thin films, structural changes can also be imposed on the thin film's surface. We refer to the surface of a thin film as the volume within 1-2 nm of the top surface. One of the evident examples of surface

manipulation can be found while slicing unit cells along different orientations of the same materials. The surface structure can be cubic lattice, rectangular lattice, or hexagonal lattice depending on whether the exposing crystal plane is (001), (110), or (111) respectively. A (100) orientation results in AO and BO_2 surfaces alternatingly, (110) orientation results in ABO and O_2 layers and (111) orientation results in AO_3 and B layers alternately. Having these features, thin - film perovskite oxides allow to tune their physical properties despite preserving the same chemical composition. It has been observed that the Curie temperature decreases by 170 K in $BaTiO_3$ epitaxial thin films grown on (110) compared to (100) STO substrates [11]. It has been reported that preferential reduction of Ag^+ and oxidation of Pb^{2+} takes place on (100) orientation of STO nanocrystals [12,13]. As a result, the authors concluded that the surfaces of type (100) are the most active compared to polar surfaces (110) and (111) of STO.

1.2.4 Doping and Strain

Along with all the above-discussed lattice degrees of freedom, doping in perovskite oxide is another crucial knob to dial multiple interactions. La is a popular doping element for divalent A-site in perovskite oxides such as STO and $BaSnO_3$ (BSO) [14–16]. This doping has changed the semiconducting nature of STO and BSO to the conductor both in thin film and bulk structure. Another example is the Nb doping on STO, which is popular for thin-film growth as a conducting substrate with lattice parameters close to the STO. Many crucial measurements to characterize the grown films require conducting substrates where niobium doped STO (Nb:STO) comes into a big play as substrate. This conducting nature of the substrate helps to alleviate the charging effect on the sample in a handful of measurements such as X-ray photoelectron spectroscopy (XPS),

scanning tunneling microscopy, low energy electron diffraction, low energy electron microscopy etc. Due to the obvious heightened sensitivity of doping level to device performance, doping for device application must be done with extreme caution. A semiconductor may not be effective for device purposes unless it is doped, which comes at the cost of negative effects such as dopant scattering. In modern times, these insights have led to the pursuit of a dopant-free, clean interfacial system [17,18].

The lattice mismatch between the two materials governs strain in heteroepitaxial development with a film and substrate. The lattice mismatch f can be calculated as:

$$f = \frac{2(a_f - a_s)}{a_f + a_s} \sim \frac{a_f - a_s}{a_f}$$

where a_s is the substrate lattice parameter and a_f is the film lattice parameter [19]. Among different growth modes, when layer-by-layer growth occurs, the film grows with an in-plane lattice parameter equal to the substrate's lattice parameter which is referred to as coherent strain and results in biaxial strain in the film. Strain energy is highly dependent on film thickness and is another important factor that determines the possible strain a grown film must go through. Usually, small film thickness compared to the substrate is good enough to maintain coherent strain. The elastic strain energy increases in direct proportion to the thickness of the film. The strain energy becomes too high to maintain coherent epitaxial growth at a critical thickness, and misfit dislocations occur to relax the strain. Because the strain energy is inadequate to support enough dislocations to fully release away all strain, dislocations form with a low density at first. But the dislocation density increases as the thickness of the film increases, reducing strain and pushing the

film's lattice parameter closer to the bulk value. Hence the choice of the substrate to grow one oxide on another is also another aspect to tune functionalities and morphology in perovskite oxides.

1.3 Heterostructure

The sample surface is the most basic interface with vacuum. Since early predictions of unique electronic surface states, physical phenomena at solid surfaces and interfaces have sparked intensive research interest which has generated applications that have transformed our way of life. The metal-oxide-semiconductor field-effect transistor (MOSFET), which lies at the heart of every electronic device, is probably the most notable example. When two materials are combined, interesting phenomena emerge at the interface. The technological advances in semiconductor heterostructures overlapped with the discovery of novel quantum phenomena. Transition metal oxides are a type of material that has a wide range of functional properties not found in ordinary semiconductors. One of the most essential aspects of a heterojunction is the band offsets at the interface of two semiconductors. Understanding the link between interface physical structure, electronic structure, and charge transfer requires precise band offset measurements. For years, it has been known that combining core-level and valence band XPS is one of the straightforward experimental approaches for measuring valence band offsets [20].

The presence of an interface can have an impact on electronic degrees of freedom, potentially resulting in novel and fascinating physical phenomena. The interface impacts the properties of oxides through different mechanisms such as symmetry breaking, charge transfer, and strain. Ordering and mutual interaction of several degrees of freedom such as charge, spin, orbital, and lattice are involved in the unique features of oxide materials. Translational and inversion symmetry

are violated at the interface as two different materials must share the same platform. This situation gives rise to the modified band structure due to the altered hybridization of the ionic orbitals. The interface can play a major role in resetting the Fermi level, resulting in charge transfer and non-equilibrium transport behaviors. Another intriguing feature is the atomic reconstruction at the interface, which can allow oxygen octahedra in perovskite oxides to rotate in the perfect cubic structure of the bulk oxide, changing its conducting and magnetic properties. One of the highly studied systems formed by deposition of $LaAlO_3$ (LAO) on STO (100) turns out non-polar STO to be carrying layers of free carriers at the interface [21–23]. Though LAO and STO are insulating and non-magnetic oxides, their interface shows a two-dimensional electron system with high electron mobility, superconductivity at low temperatures [24] and electric-field-tuned metal–insulator and superconductor–insulator phase transitions [25]. Complex oxides are highly sensitive to defects, such as the cationic defect observed at the LAO/STO interface, which can limit transport properties [26] or create magnetic interfaces [27] out of non-magnetic complex oxides. Due to their narrow range of cell dimensions (3.85 - 4.1 Å), perovskite oxide heterostructures, on the other hand, are relatively easy to stack one on top of another for the heterostructure purpose. On the other hand, thin-film deposition technology has advanced to the point that it is now able to customize oxide heterostructures with sub-nanometer precision. These advancements in technology have advanced the research of clean interfaces at metal oxide heterostructures, paving the way for unique future applications.

1.4 Two Dimensional Electron Gas

Moving towards the low dimensions allows broader dynamics of buried phenomena where surfaces and interfaces come into play. Compared to the bulk, large varieties of properties can be tuned at the interface of various heterostructures including traditional semiconductors and transition metal oxides (TMOs). The polar discontinuity has been one of the key phenomena observed in semiconductor interface since the early eighth century. It was observed in the growth of GaAs on (001)-oriented Ge, where both semiconductors have the same crystal structure and nearly exact lattice parameters [28,29]. Indeed, the introduction of interfaces in semiconductor structures stimulated the discovery of many other exciting physical phenomena, leading to the development of several semiconductor devices that dominate modern technology. High-quality heterostructures generated by molecular beam epitaxy (MBE) in conventional III–V and group-IV semiconductors have led to several scientific discoveries, including the fractional quantum Hall effect [30]. The effective mass model is used to describe the phenomenon governed by states around the conduction band minima in traditional semiconductor heterostructures with wide band gaps. Carrier mobility has long been utilized as a highly sensitive metric of material and heterostructure quality in traditional semiconductor heterostructures. Surprisingly, the behavior of traditional semiconductors like silicon is less intriguing in the bulk of the material. Because oxide materials already have more complex physics in the bulk, we can expect physical phenomena at oxide interfaces to be far more stunning than those seen at normal semiconductor interfaces. On the other hand, quantum-confined states occur in many oxides and involve carriers in narrow d-bands that are usually significantly filled and are subject to strong electron-electron correlation effects and exchange coupling, which ultimately dominate the transport parameters [31–33].

Oxide heterointerfaces exhibit a wide range of emergent behaviors not found in their bulk constituents due to spontaneous interactions of charge, spin, lattice, and orbital degrees of freedom in correlated complex oxides [34,35]. Scattering from different imperfections, such as ionized donors or acceptors, impurities, dislocations, interface roughness, cation and oxygen vacancies, and other defects, inhibits mobility at low temperatures. Generally, binary oxides such as SnO_2, ZnO, In_2O_3 shows similar characteristic wide bands and low effective masses as traditional semiconductors. A high mobility 2DEG in TMO heterostructure at low temperature is believed to be mainly restricted by scattering due to ionized impurity. As there are different parameter that can tune the mobility, high-mobility perovskite oxide heterostructures are still in the early stages of development compared to typical semiconductor heterostructures [36,37].

Since progress in this area was delayed for many years by challenges in synthesizing epitaxial oxide multilayers, the physics of oxide interfaces is still under exploration. New deposition techniques such as pulsed laser deposition (PLD), MBE, and hybrid MBE (hMBE) have been developed to solve this problem. Ultraclean oxide heterostructures with atomically clean surfaces may be grown using these approaches. They are grown layer by layer as thin as one atomic layer, as confirmed by in situ reflection high-energy electron diffraction (RHEED). To access the 2DEG in oxide interfaces, different approaches have been employed including polar catastrophe [21]. Another approach implemented to enhance mobility and carrier concentrations is delta doping in oxides [38–40]. Delta doping has long been employed in conventional semiconductor systems investigating the introduction of several subbands to enhance the mobility and carrier concentrations [41]. Delta doping is mostly understood as a thin layer of dopant semiconductor on

top of another semiconductor. Along with the thickness of the doping layer, the capping layer has a significant role in performing 2DEG characteristics [40]. To optimize the interfacial charge transfer mechanism, charge carriers must be isolated from the scattering center in heterostructure engineering. Due to the purity provided by segregated carriers and donor sites, modulation doping is widely used these days. On the other hand, carriers and mobility tunability is another important feature of modulation doping. One of the exemplary systems recently studied for modulation-doped perovskite oxide grown by hMBE is the stannate interface $SrSnO_3$ (SSO)/BSO [42]. The thin layer of SSO between the La-doped SSO donor and the BSO active layer functions as a spatial separation, resulting in a modulation-doped system. To pursue high mobility devices, the goal is to synthesize interfaces with low cation diffusion to reduce impurity and interfacial scattering. Although the presence of a buffer layer is not unusual to stop cation interdiffusion in device technology, it might be counterproductive if the buffer layer is not chosen properly. It would be fascinating to have an interfacial system with a large number of free carriers, such as $SrNbO_3$ (SNO) as a donor, where cation interdiffusion to the active layer is not a factor.

Understanding the charge transfer mechanism is crucial due to its wide applicability in high mobility electronics. When two oxides are layered together to form an interface, charge transfer takes place to balance the electron chemical potentials and Fermi level of both materials. This phenomenon is primarily responsible for the rich physics seen in traditional semiconductor heterostructures, which led to the development of devices such as the p-n junction, Schottky diodes, and high-mobility transistors based on 2DEG. Perovskite oxide, like classical

semiconductors, exhibits a variety of phenomena that are made even more intriguing by the addition of d-orbital cations and spin degrees of freedom.

Novel interfacial phenomena continue to emerge in perovskite oxide heterostructures, in addition to the variety of intriguing properties in bulk and thin films. Similar, to the surface, the ions at the interface can be reconstructed, breaking the symmetry of the constituent bulk oxides even further. The existence of an interface in perovskites, for example, can cause oxygen octahedra to rotate in the ideal cubic structure of the bulk oxide, changing its conducting and magnetic characteristics as well as the ferroelectric order. Multiple properties can be tuned at the interface of perovskite oxides including 2DEG. The development of 2DEG at the LAO/STO interface [21] provided a significant thrust to the research of oxide interfaces as an alternative to the traditional wide band gap semiconductors as a high-speed electronics material. In STO-based interfaces, multiple interesting phenomena such as magnetism [43], superconductivity [44,45], Rashba spin-orbit coupling [46] along with 2DEG are observed due to the Ti 3*d* bands character. Interfacial magnetism is an uncommon property among these features, considering both LAO and STO are nonmagnetic in nature. The intrinsic electronic reconstruction, i.e., polar catastrophe, was principally supposed to be responsible for the formation of 2DEG in LAO/STO interface. Other mechanisms have also been postulated to explain the origins of interfacial 2DEG conductivity in LAO/STO, including oxygen vacancies, [47], interface cation mixing [48], cation off stoichiometry [26,27] and internal structural deformation, [49]. 2DEG in other complex oxides, aside from titanate-based heterostructures, is largely unexplored. Alkaline earth stannates have attracted interest because of their excellent room-temperature electron mobility while remaining optically transparent, making

them viable candidates for transparent conducting oxides (TCO). One of the interesting stannates to look at is BSO, when La-doped, it is reported to show the highest mobility in record 320 $cm^2V^{-1}s^{-1}$, with $8\times10^{19}cm^{-3}$ n-type carriers, for complex metal oxides [50]. The vacant 5s orbital of the Sn atom, which leads to a low effective mass of carriers in BSO, is believed to be responsible for such high mobility of La-doped BSO.

Indium-based oxides are predominantly used in optoelectronic applications since three decades due to their transparent conducting nature [2,51]. The scarcity of elemental indium on Earth has led to the search for indium-free materials, such as stannates in recent years. Low resistivity observed in TCOs can be improved either by increasing the carrier mobility and/or carrier density. Although there is a tradeoff between these two parameters, mobility enhancement is the more favorable alternative for TCO films due to their higher carrier density. Complex metal oxides are good alternatives to replace indium-based optoelectronic materials since they offer more degrees of freedom, such as spin and structural deformation [52,53]. On the other hand, engineering interfaces with BSO as an active layer and a good donor as a dopant may result in high mobilities and carrier concentrations for high-speed electronics applications. Another unique feature that can be exploited for next-generation electronics is ferromagnetism discovered in 2DEG at the non-magnetic oxide interface, LAO/STO [43]. Interestingly, spin-polarized 2DEG can be used in spintronic devices like magnetic memory and spin logic. Furthermore, unlike typical semiconductors, complex oxides can display substantial spin-orbit coupling when conduction bands contain 5d electronic states, allowing for next-generation THz spin-Hall nano-oscillators [54,55].

1.5 Overview of Thesis

This dissertation work intends to elaborate on the application of the emerging thin film growth technique, hMBE to synthesize ultraclean perovskite oxides at the atomic level. The major goal of this dissertation is to correlate the surface and interface of ultraclean samples grown by hMBE for future applications in multiple fields due to the observed multiferroic, ferroelectric, ferromagnetic and superconducting properties. Chapter 2 introduces the properties and related physics of STO, SNO and BSO. Different popular techniques that have been used for the growth of thin-film oxides are introduced and the effectiveness of hMBE technique is discussed in chapter 3. The purpose of Chapter 4 is to describe the material characterization techniques employed in this dissertation, as well as their operational principles including related physics. Chapter 5 investigates the surface stability in STO thin films grown by hMBE. The first ever hMBE growth of metastable SNO and its surface stability is studied in chapter 6. In chapter 7, possible charge transfer in SNO/BSO interface is discussed investigating tin oxidation state through Sn 3*d* core level. Finally, chapter 8 summarizes the study of surfaces and interfaces of hMBE grown perovskite oxide thin films and presents a proposal for future research.

Chapter 2

Materials Properties and Related Physics

2.1 $SrTiO_3$ Overview

2.1.1 Crystal Structure

In thin-film perovskite oxide technology, $SrTiO_3$ (STO) is a prototypical simple cubic perovskite oxide with lattice parameter of 3.905 Å [56]. Figure 2.1 shows that oxygen octahedra surrounds the Ti-site at the body center and Sr-site cations at the corner of a unit cell. The band structure of STO depicts a band gap of 3.27 eV with the valence band maximum (VBM) and conduction band

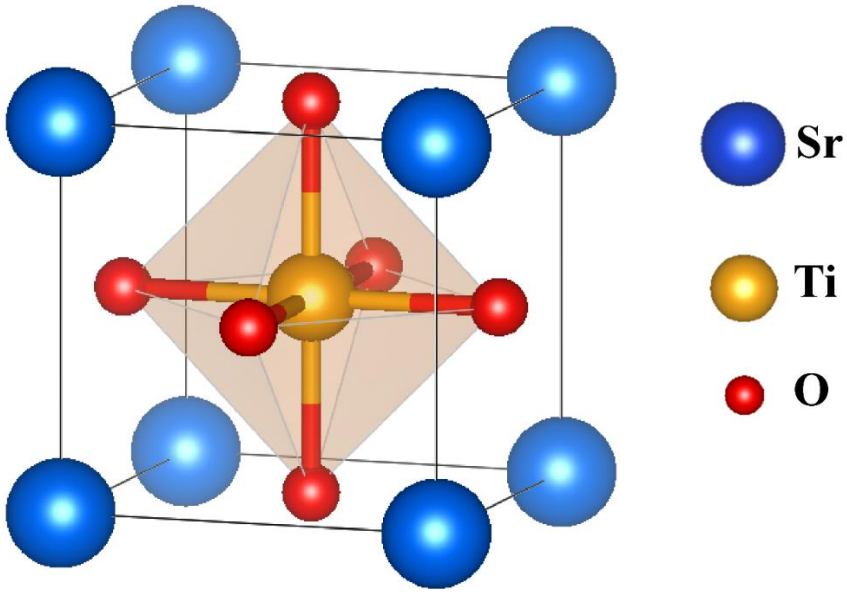

Figure 2.1: $SrTiO_3$ cubic unit cell

minimum (CBM) populated by O 2*p* and Ti 3*d* states, respectively [57]. Due to its simple structure and fascinating properties, STO is one of the most investigated materials in thin-film complex

oxides. The ionic charges of Sr^{2+}, Ti^{4+}, and O^{2-} are observed in the cubic perovskite structure of STO. During STO synthesis, either SrO or TiO_2 termination can be observed due to their comparable thermodynamic stability. One of the most broadly adopted parameters of a film to check stoichiometry is the XRD measured lattice constant. When compared to stoichiometric STO, non-stoichiometric STO has a substantially greater lattice constant [58–60].

2.1.2 Surface properties

In comparison to the bulk, the surface of STO exhibits fascinating features such as 2DEG and topological properties, hence modern technological advancement is focused on surface related properties. There was immense attraction towards the field of oxide interfaces after the discovery of two dimensional gas (2DEG) in $LaAlO_3$ (LAO)/STO interface [21]. Though the charge transfer mechanism discussed in the LAO/STO interface is still up for controversy, with one referring to the oxygen vacancy in STO-driven phenomena [21,36,61] and the other to the polar discontinuity at the interface-driven phenomena [62]. Surface termination of a STO film triggered by contaminants, surface defects, and other sources of defects may result in novel phases at the film surface that have a major impact on surface and interfacial properties. Surface sensitive probes such as atomic force microscopy and scanning tunneling microscopy (STM) revealed half unit cell step height (~ 2.0 Å) that confirms mixed terminations of SrO and TiO2 in a film, whereas unit cell step height shows the existence of either type of surface termination [62]. Surface reconstruction is a term used to describe a type of unique phase evolution that occurs at the film's surface. Surface reconstruction in STO films has been extensively researched, with STM analyzed (2x1), c(4x4), and c(4x2) phases suggesting various reconstruction [63]. The Sr adatom

model [64] is one of the atomic structures proposed for the $(\sqrt{5}\times\sqrt{5})R26.6°$ reconstruction, however no precise atomic structure model exists to describe all of the reconstruction regimes. A material's electronic property may largely deviate due to surface reconstruction which opens or closes the gap between band in band structure. Because of their potential applications in photocatalysis, surface reconstruction has gained a lot of attention.

2.1.3 Thin Film Synthesis

The importance of surface terminations demands atomic-scale control of thin film oxide growth. Multiple growth approaches have been used to synthesize STO, including metalorganic chemical vapor deposition (MOCVD) [65] and molecular beam epitaxy (MBE) [66,67]. The incorporation of an extremely low vapor pressure element or refractory element is an additional growth challenge for complex metal oxides by MBE. Among these elements, Ti is one element that is difficult to deliver using a regular effusion cell in MBE. The hybrid MBE (hMBE) technology is used to synthesize an ultraclean STO at the atomic level. In 2009, employing titanium tetraisopropoxide (TTIP) for Ti delivery, the hMBE approach was used to grow homoepitaxial and heteroepitaxial STO films for the first time [59]. The subsequent work on La doped STO [15] revealed the highest mobility in record at low temperatures, indicating that the hMBE generated STO films were of high quality. Nowadays, by supplying elemental Sr and TTIP as a Ti source, hMBE has become a standard approach for STO synthesis [5,15–17]. A massive success in the synthesis of high-quality STO films paved the way for complicated metal oxides containing elements with exceptionally low vapor pressures. In Chapter 5, the details on STO synthesis by hMBE is described.

2.1.4 Application as an Interface Active layer

The fact that STO is utilized as a typical substrate for depositing oxide compounds due to its structure and lattice constant that are comparable to those of several other significant oxides, enables for epitaxial growth. The STO-based conductive material can be formed by *n* type [71] or *p* type [72] doping due to the major conduction band contribution coming from Ti 3*d* states. It can display *d* electronic characteristics by the filling of different *d* orbitals which opens the great application opportunity of STO-based 2DEG in oxide electronic devices. Discovery of quasi 2DEG in LAO/STO interface [21] due to polar discontinuity created immense attraction towards the field of oxide interface. After this discovery, oxide 2DEG opened new phenomena because of strong electron correlation between *3d* electrons which was not observed in conventional GaAs based 2DEG that has *s* or *p* electrons as conducting electrons. Due to the presence of electron correlation between *3d* electrons, oxide 2DEGs display magnetism, ferroelectricity, spin orbit coupling characteristics [23,71,73]. Among STO based oxide interface, LAO/STO system is one of the widely studied oxide interface system up to date. Beyond 2DEG systems, studies of polar/nonpolar $LaFeO_3$/STO interfaces [74–76] demonstrates photocatalytic behavior reflecting the importance of understanding interfacial structures and defects in these materials with a great deal of precision for future electronic and energy devices.

2.2 $SrNbO_3$ Overview

2.2.1 Crystal Structure

$SrNbO_3$ (SNO) has a d^1 electronic configuration and a simple cubic perovskite structure with lattice parameter ranging from 4.0 to 4.1 Å [77]. The Sr cations are at the A-site and Nb at the B-

site forming oxygen octahedra surrounded by six oxygen atoms as shown in Figure 2.2. As previously reported in density functional theory (DFT) studies on SNO/STO heterostructures [77,78], the band diagram of SNO reveals the Nb 4d t_{2g} bands crossing the Fermi level, indicating its metallic nature. This, combined with the low work function, makes SNO stand out as a good donor [79]. Studies have also examined the material for use as a plasmonic transparent conducting material due to the large band gap between the O 2*p* and Nb 4d bands [80–82].

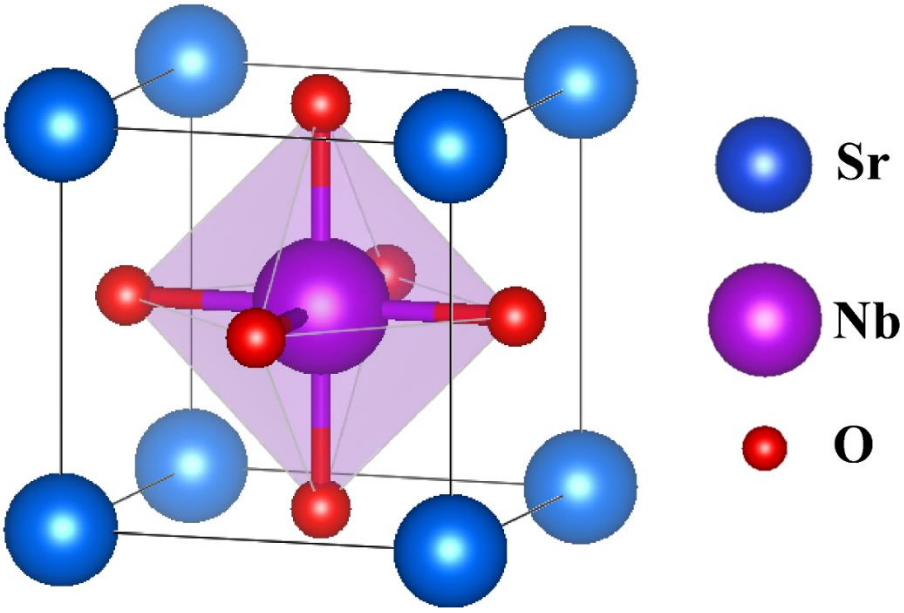

Figure 2.2: $SrNbO_3$ cubic unit cell

2.2.2 Thin Film Synthesis

SNO is a challenging material to grow due to its metastable state and difficulty in delivering Nb by evaporation because of extremely low vapor pressure. Extra care must be taken to preserve the metastable state of SNO films so that over-oxidation can be minimized or alleviated. In the past,

synthesis of SNO has been carried out by PLD [81,83,84], sputtering [80,82], but hMBE has been implemented for the first time in our work which will be discussed in chapter 6.

2.2.3 Role as a Donor in 2DEG

4d electronic states are more extended than 3*d* electronic states, resulting in enhanced hybridization with surrounding oxygen ions and weaker on-site coulomb interaction, promoting a stronger metallic character and fewer electronic correlations, and resulting in higher electrical conductivity [79]. SNO with the Nb $4d^1$ electronic configuration produces a large charge carrier density that crosses the Fermi level providing metallic-like behavior. Presence of an extra electron and low work function makes SNO a good donor. As predicted by density functional theory (DFT) studies on SNO/STO heterostructures [78], SNO is proposed as a good donor to STO. Recent exciting results on SNO/STO interfaces [85,86] grown by PLD without capping layers with atmospheric exposure reflects the importance of SNO for candidate material as a donor. However, these predictions may not be the complete story and our findings on the role of a capping layer of metastable SNO films [87] discussed in chapter 6 would likely change the interpretation of both findings.

2.3 $BaSnO_3$ Overview

2.3.1 Crystal Structure

$BaSnO_3$ (BSO) is a cubic perovskite structure with lattice parameter of 4.13 Å [88]. The Ba cations occupy the A-site and Sn cation the B-site forming oxygen octahedra surrounded by six oxygen atoms as shown in Figure 2.3. The electronic band structure of BSO shows that the VB states are O 2*p* contributed while CBM has Sn 5s states with indirect band gap of 3.2 eV [89]. BSO is

considered as one of the interesting transparent conducting oxides (TCO's) due to its optical band gap [88] and *s* character in CBM. La doping in BSO has been reported to produce electron mobilities comparable with the best TCOs [50,90,91]. Due to the scarcity of In for In-based TCOs, the search for an alternate material led to the BSO, which has reasonable TCO characteristics.

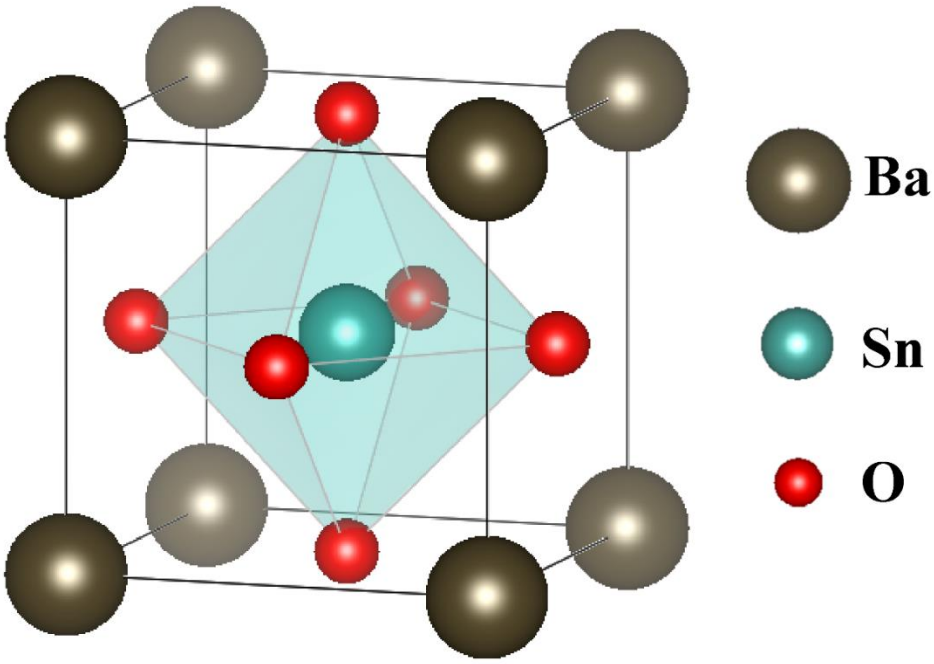

Figure 2.3: $BaSnO_3$ cubic unit cell

2.3.2 Thin Film Synthesis

A bulk La-doped BSO outperforms thin film BSO in mobility [50] which directs towards the improvements in synthesis of high quality BSO thin films. The stoichiometry of a thin film and the choice of lattice matched substrate have a major impact on sample mobility. Compared to the bulk single crystal, BSO thin films have low mobility mainly due to substrate misfit introduced threading dislocations [16] and point defects due to non-stoichiometry and scattering effects due

to La dopant concentration [92]. The BSO thin films have been grown by PLD [89], MBE [16] and hMBE [93,94] in the past. One of the major concerns in synthesis of BSO is a Sn contamination [95] of the chamber so we will be using as grown BSO film from Cornell University to grow SNO film on top of it to carry out carrier concentration and mobility measurements in SNO/BSO interface.

2.3.3 Role as an active layer in 2DEG

BSO has a comparable band gap with STO. Inversely, compared to the Ti *3d* states in STO, BSO has its CBM contributed by Sn *5s* states with little O 2*p* hybridization producing low effective mass that is suitable for high electron mobility [92]. Electrical conductivity along with optical transparency stands out BSO as one of the candidate materials for modern optoelectronic applications. A Hall mobility of 103 $cm^2\ V^{-1}\ s^{-1}$ with an n-type carrier concentration of ~8–$10\times10^{19}\ cm^{-3}$ in La-doped bulk BSO single crystal was reported [90]. Subsequently, largely improved Hall mobility of 320 $cm^2\ V^{-1}\ s^{-1}$, highest mobility in complex metal oxides up to the date, with $8\times10^{19}\ cm^{-3}$ n-type carriers was achieved in La-doped bulk BSO single crystal [50] highlighting a potential application of BSO as an optoelectronic materials. Due to these interesting characteristics, BSO has gained increasing attention as a candidate material for next-generation oxide electronic devices. Compared to the bulk single crystal, BSO thin films have low mobility mainly due to substrate misfit introduced threading dislocations [16] and point defects due to non-stoichiometry and scattering effects due to La dopant concentration [43]. Our work in chapter 7 focuses on SNO/BSO interfacial system where SNO acts as a donor in modulation doping fashion.

Since dopant scattering can be safely ruled out, this approach will dramatically increase BSO mobility.

Chapter 3

Thin Film Growth

3.1 History of Oxide Molecular Beam Epitaxy

Oxide molecular beam epitaxy (MBE) was first employed to grow Al_2O_3 on GaAs using molecular oxygen and aluminum deposition to prepare a metal oxide semiconductor heterostructure [96]. One of the challenges faced was inadvertent oxidation of the GaAs crystal that changed the crystal structure of the GaAs substrate. This oxygen diffusion to the GaAs occurred during the high growth temperature required for Al_2O_3 synthesis and was irreversible. On the other hand, maintaining a lower growth temperature would be unacceptable since the film's crystallinity would suffer and show oxygen defects. Later, more efficient oxygen sources were used such as oxygen plasma and ozone to increase oxygen reactivity for the film even at lower temperatures. In 1985, $LiNbO_3$ was the first crystalline ternary oxide grown by MBE [97]. After the discovery of room temperature superconductivity in cuprates [98,99], the utilization of MBE as a growth technology skyrocketed. However, the amorphous nature of thin films formed by MBE did not exhibit the desired properties, hence post-growth annealing was employed. Most importantly, oxygen plasma and ozone assisted MBE growth were used to maintain the quality of a thin film and provide uninterrupted growth of superlattice and interfaces [100,101].

3.2 Oxide Molecular Beam Epitaxy

Delivering highly reactive oxygen has played a major role in producing high-quality films in oxide growth through several procedures such as cleaning substrates, eliminating contaminants during growth, and modifying the reactiveness of an oxidation process. Since the introduction of

molecular oxygen in MBE growth, other forms of alternate oxygen sources have been employed. Ozone and oxygen plasma is used as an oxygen source in growths that demand highly reactive oxygen since they provide atomic oxygen, O^-. Atomic oxygen plays a critical function in removing carbon contamination [68,102], which is essential for creating high-quality surfaces and interfaces in samples. This is important because many unique phenomena occur at the surface or interfaces of a structure. Ozone and oxygen plasma are both often used as oxygen sources for reactive oxygen MBE growth these days. Depending upon the plasma power and oxygen pressure, oxygen plasma efficiency varies largely. On the other hand, proper care of an ozone source must be taken to eliminate liquefaction of ozone which acts as an explosive and has been reported in different instances [103,104]. In some cases, nitrogen dioxide (NO_2) and hydrogen peroxide (H_2O_2), in addition to molecular oxygen, oxygen plasma, and ozone, have been demonstrated to act as oxidizing agents [105,106]. The low reactivity of NO_2 compared to ozone, along with incorporation of nitrogen ions at oxygen sites, makes NO_2 not a favored oxidant [107]. H_2O_2 has also been shown to be an effective oxygen supply for oxide film development [108] although its usage is limited since water vapor in the main growth chamber is a likely byproduct, which is undesirable for ultra-high vacuum (UHV) synthesis.

3.2.1 Challenges with Oxide Molecular Beam Epitaxy

Along with the selection of oxygen sources either in the form of molecular oxygen, radio frequency plasma, ozone, NO_2, or an H_2O_2, practical compatibility issues in UHV system must be considered. Despite the importance of the reactive oxygen source in oxide growth, undesired oxidation in the substrate heater filament, substrate holder, and source material are key issues that must be

addressed. The use of oxidation-resistant substrate holders and heating filaments in substrate heaters and source heaters would greatly reduce the problem of unwanted oxidation. This includes finding highly oxygen resistant material for the heater filament since as the temperature is increased, oxygen starts to become more reactive, and oxidation is inevitable. Unless this unwanted oxidation is greatly reduced, contaminants will end up in the film, degrading the quality of the sample. On the other hand, those oxidized pieces of instrument do not last that long which is another challenge as a grower.

Oxidation of metal effusion cell heating filament could occur in the case of a less oxygen resistant crucible. Beside filament oxidation, oxidation of the metal source material is a substantial issue in oxide growth. Oxidation of source material could happen both in refractory elements such as Ti, V, and Nb, and in elements with high oxidation potential such as Sr, Ba, and Ca [109,110]. Those high oxidation potential elements can be readily oxidized in the presence of oxygen, and low vapor pressure elements require high cell temperature to evaporate properly. The reactivity of the elements rises with oxygen exposure at higher cell temperatures, resulting in the oxidation of the source. Another common problem with high cell temperatures is the blockage of the crucible aperture by elemental oxides, which results in metal flux instability. This has a significant impact on the stoichiometry of the grown sample. Oxidation of the source elements can be minimized by pumping out the source through differential pumping. Differential pumping is greatly effective in isolating highly oxidizing source elements during venting of the chamber.

Fluctuations in cation fluxes are another key problem in synthesizing high-quality samples using MBE. Under an oxygen environment, a quartz crystal microbalance (QCM) can be used to measure

cation fluxes for some of the metals such as Sr to measure flux in their oxide form. The QCM is used to measure small mass changes in a quartz crystal resonator in real time as it is exposed to an effusion cell, which is useful in monitoring the growth rate. One drawback with QCM is that the QCM's head must be replaced on a regular basis since the sensor becomes less sensitive over time as deposited mass increases. Differential pumping supports the QCM head replacement process without exposing UHV chamber to the atmosphere.

Modern MBE systems are equipped with a surface sensitive tool called a reflection high-energy electron diffraction (RHEED) system that is effective for monitoring the surface morphology, growth rate and growth modes. RHEED is also used to adjust cation fluxes to obtain stoichiometric samples [67]. Along with the RHEED to monitor the quality of the sample, post growth complementary characterization techniques such as X-ray photoelectron spectroscopy (XPS) is also used to check the sample stoichiometry. The long-term continuous use of a RHEED system leads to the oxidizing environment oxidizing the RHEED filament. Differential pumping is one of the highly practiced approaches to extend the filament lifespan from oxidation.

Obtaining adsorption-controlled growth in perovskite oxides is important to carry out highly controlled repeated synthesis of stoichiometric samples. It was during the first time MBE was used to grow GaAs [111] that it was considered an adsorption-controlled growth. $PbTiO_3$ was the first perovskite oxide system [112] investigated for adsorption-controlled growth. This type of growth is advantageous in eliminating small flux instabilities and unreliability in sample growths. Usually, excess cations on a film during the growth are desorbed in the form of their oxide which helps to maintain a proper stoichiometric ratio throughout the sample. Adsorption controlled growth has

been obtained in many other perovskite oxides [113] including $PbTiO_3$. To obtain adsorption-controlled growth in MBE, the equilibrium partial pressure of a volatile oxide should be high enough to carry out the growth at a realistic temperature and practical growth rate. However, adsorption-controlled growth is not attainable in many other perovskite oxides, especially those including refractory elements. Major issues with these low vapor pressure elements include difficulty in maintaining sufficient vapor pressure and instability in flux rates in oxygen environments. Oxygen defects in films also appear due to the need of keeping low oxygen pressures to maintain reasonable mean free paths. To circumvent these issues and obtain adsorption-controlled growth window in perovskite oxides, the hybrid MBE (hMBE) technique was developed.

3.3 Hybrid Molecular Beam Epitaxy

Due to the lack of an adsorption-controlled growth window, MBE growth of complex metal oxides is more challenging than that of binary semiconductors such as GaAs. Some growths involving cations and cation oxides with high vapor pressures such as Pb in $PbTiO_3$ and RuO_x in $SrRuO_3$ can be carried out with ease [114]. In general, cations do not exhibit high vaporization and it is even more challenging in the case of refractory elements such as Ti, Nb, Zr, V. This makes them difficult to use in synthesizing a material with perfect stoichiometry. Regular oxide MBE uses effusion cells for each elemental source, but this is not always possible when working with low vapor pressure metals, as stated in the preceding section. The hMBE is a combination of conventional MBE and metalorganic MBE approach where the A-site cation is supplied through an effusion cell and the B-site cation is supplied in the form of a metal-organic precursor and

reactive oxygen environment as shown in Figure 3.1. This method was first employed in synthesis of $SrTiO_3$ (STO) film using an effusion cell for Sr-site cations and a metal organic precursor, titanium tetraisopropoxide (TTIP), for titanium [59,115]. A stainless-steel bubbler is used to vaporize the precursor and is connected through the gas inlet system to the growth chamber. To avoid condensation and potential blockage, the gas lines are kept at a greater temperature than the bubbler. Although liquid nitrogen flow is commonly used to cool the growing chamber shroud, which can trap adsorbed byproducts and unreacted metal organics, a low-temperature fluid called Syltherm XLT has also proven to be quite successful for this purpose [68,87]. Due to the high vapor pressure and ability to perform without a carrier gas, hMBE is useful for delivering metals in the form of their organic precursor. As the valve separates the connection between the precursor and the chamber, the beam flux remains extremely steady in a low-pressure oxygen atmosphere. This setup also allows for the refilling of metal organics without disrupting the UHV of the growing chamber. The oxygen bonded precursor is usually effective in oxide formation because the bonded oxygen with metal ions present in the precursor helps to achieve the sample's stoichiometry. Furthermore, hMBE growth is extremely effective at maintaining an adsorption-controlled growth at reasonable temperatures, which may not be possible with standard oxide MBE. In the case of STO growth, it has been predicted that the SrO terminated site is more favorable to dissociate the TTIP precursor, accelerating the film deposition [113]. A consecutive study shows that SrO termination is necessary to obtain stoichiometric sample [68].

Physical properties are highly influenced by point defects, whether they be vacancies or interstitials. In the case of STO, the adsorption-controlled growth window largely reduces the

chance of off-stoichiometry growths normally caused by fluctuation in traditional effusion cell beam flux. This, in turn, reduces the defect concentration in films. Low temperature electron mobilities in La-doped STO were reported to exceed 50000 $cm^2 V^{-1} s^{-1}$ [116] in samples grown using this method, which is more than two times higher than those reported in bulk single crystal [117] and much higher than those in films grown by PLD [118]. This depicts the effectiveness of hMBE in reducing defects and enhancing the mobility of a film at low temperature. In addition to STO, $BaTiO_3$ [119] and $CaTiO_3$ [120] has been grown using a TTIP precursor, proving it to be an effective precursor for self-regulated growth. Along with this titanium-based precursor, hMBE has proven effective for epitaxial development of numerous refractory metal oxides, including vanadates, zirconates, and titanates [15,59,70,102,113,115,121,122].

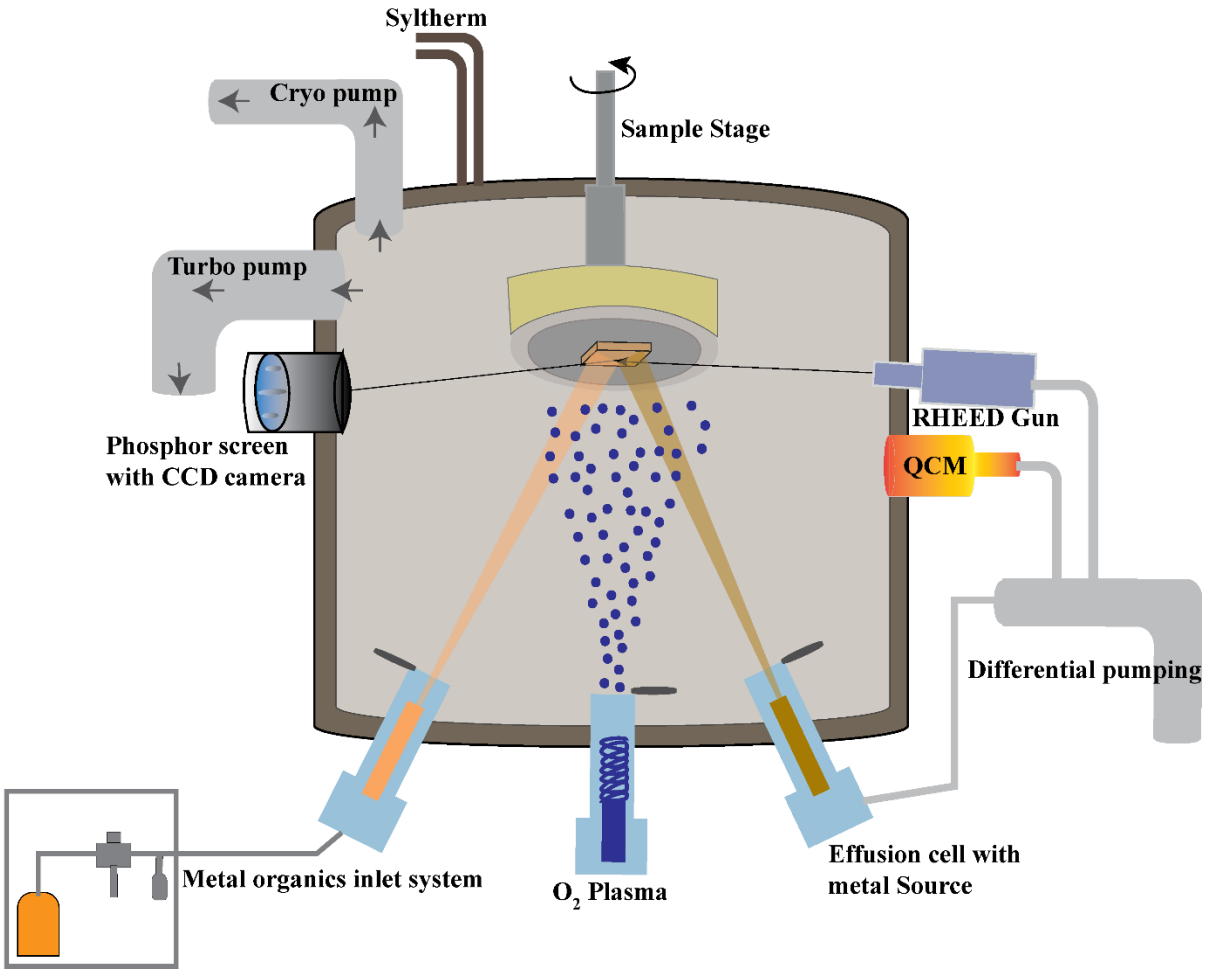

Figure 3.1: Hybrid molecular beam epitaxy system schematic.

3.3.1 Challenges with hybrid Molecular Beam Epitaxy

One of the common challenges in hMBE is the choice of the UHV-suited precursor. It is not always easy to pick a precursor for delivering low vapor pressure cations. Precursors themselves are metal organics consisting of hydrocarbons which can be a source of carbon contamination in a film. Although, carbon contamination is inevitable in air-exposed samples, carbon contamination in sample during the growth must be minimized for synthesizing high quality films using hMBE. Besides changing the stoichiometry of a sample, the chemistry of a film can also deviates compared

to that of a pristine sample. This will eventually affect the understanding of the film and its subsequent properties governed by the bulk, surface, and interface. Carbon contamination on a sample can be reduced by increasing the growth temperature in STO growth [68,123]. Mostly, oxygen coordinated precursors are useful in growing perovskite oxides at low oxygen pressures by hMBE. An oxygen free precursor could be a wise choice where a relatively low oxygen environment is needed to preserve metastable perovskite oxides such as $SrNbO_3$ (SNO) [87]. The adhesive nature of the organic leftovers from metal organics and unreacted metal ions stick to the chamber wall, making it difficult to keep the growth chamber clean for subsequent growth. Maintaining their adhesion to the chamber wall during growth is useful in reducing the integration of those byproducts in a film but removing them from the chamber wall permanently after the sample has been removed from the chamber is critical. Baking the chamber helps in the removal of these byproducts from the chamber wall, but it is a time-consuming and tedious process. In recent times, an infrared radiation lamp is illuminated inside the chamber for a few hours to help remove major byproducts and unreacted metal ions from the chamber walls between growths.

3.4 Growth Modes

Epitaxial film growth is a broad field that includes many types of materials, such as metals, semiconductors, and oxides. Surface chemistry, kinetics, and elastic characteristics of materials all influence epitaxial film growth. Epitaxial growth can be divided into two types: homoepitaxy which refers to the growth of a film of the same material as the single crystal substrate, and heteroepitaxy which refers to the synthesis of a film different than the substrate. Different growth

modes are possible in epitaxial thin film growth. These growth modes are primarily categorized as layer-by-layer, island growth, and layer plus island growth as shown in Figure 3.2.

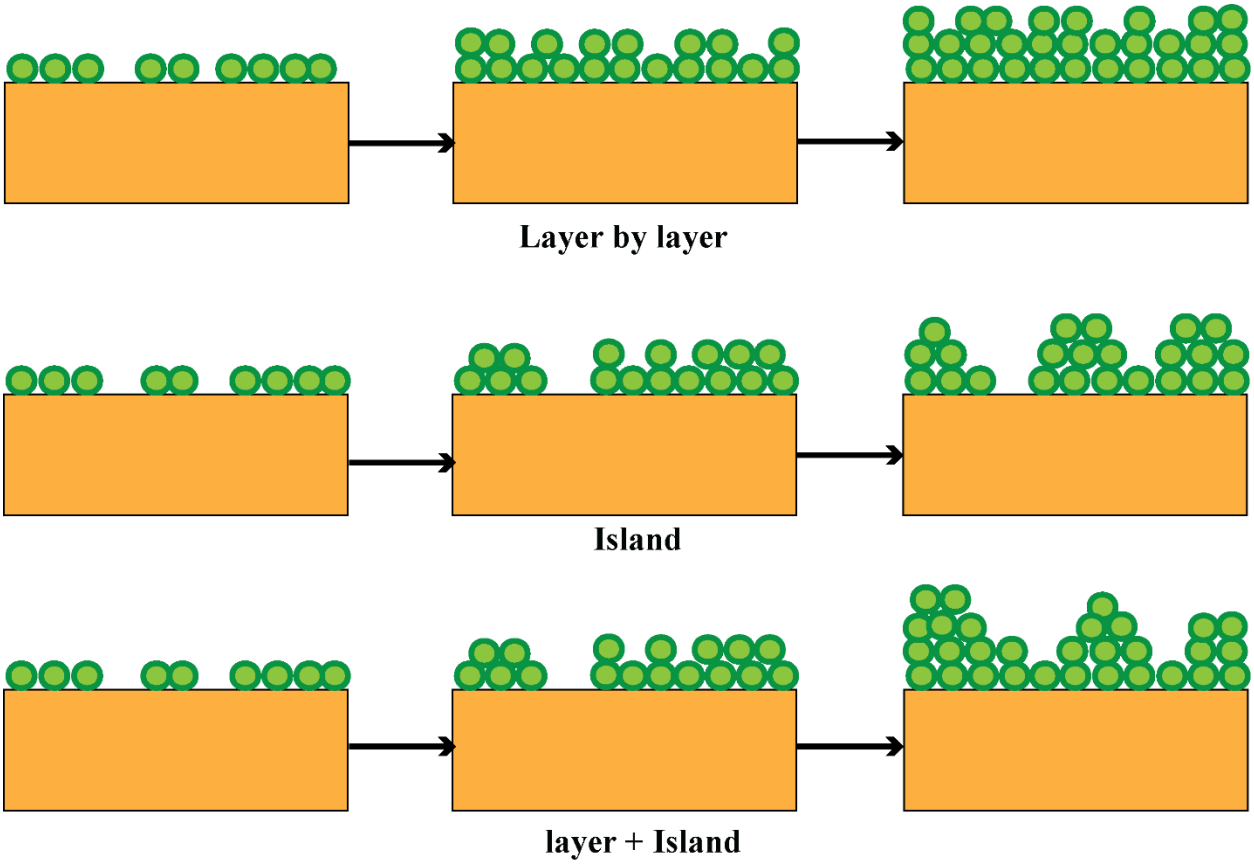

Figure 3.2: Different growth modes common in MBE.

A layer-by-layer growth is a self-terminating cyclic deposition process that does not initiate deposition of a second layer until the first layer is completed [124]. This growth mode is useful in calculating film thickness as each cycle represents one monolayer of a film. This type of growth usually occurs at low growth temperature, high particle flux and high background pressure. When the surface diffusion length is much larger than the substrate surface terrace length, surface steps on the substrate surface represent energetically favorable sites for nucleation. This situation during

a growth leads to the step-flow growth mode [125]. Island growth occurs when clusters of atoms form on the surface of the substrate and grow into individual islands that are many atomic layers in height [126]. The film does not wet the substrate's surface in this scenario, leaving some areas uncovered as the islands expand in height. More islands form as more material is deposited, and the islands finally combine to form a columnar epitaxial film. In some cases, combination of both layer and island growth can be observed depending upon the growth condition. The initial interface energy between the substrate and the film encourages layer-by-layer expansion during layer plus island growth. However, as the film thickness increases, strain energy from the substrate's lattice mismatch favors island formation as a mechanism of strain relaxation [126].

3.5 Substrates and Substrate Preparation

The quality of the underlying crystalline template, or substrate, is critical in epitaxial single crystal growth. To prepare a smooth and defect-free substrate surface for epitaxial growth, various processing methods such as chemical mechanical polishing and chemical etching are used. The extra care taken in substrate preparation has been key to the success of semiconductor technology. As a result, modern semiconductor technology is able to deliver high quality technology on a large scale. One of the most important components in high-quality epitaxial single crystal growth is a lattice-matched substrate. The larger the lattice mismatch, the more strain is introduced into the film and changing the structural properties of the grown films. Although, studies involving film strain has led to the emergence of unprecedented features in materials and is another fascinating area of cutting-edge research [127–132]. According to the purpose of experiment, many different substrate types were used in this research work. STO is one of the most commonly used substrates

throughout research due to its wide availability and suitable lattice constant for many growths. In case of homoepitaxial STO growth, calibration substrates such as $(LaAlO3)_{0.3}(Sr2AlTaO6)_{0.7}$ (LSAT) and sapphire were used. Some of the STO samples are prepared on Nb doped STO substrates to carry out scanning tunneling microscopy and low energy electron diffraction/microscopy measurements that require conductive substrates. To grow SNO, STO is mostly used as a calibration substrate while $GdScO_3$ (GSO), $TbScO_3$ and $BaSnO_3$ are used as a major substrate for research sample growth.

Figure 3.3: Substrate mounted on a 10x10 mm^2 sample holder

All substrates used in this study are either 10x10 mm^2 or 5x5 mm^2 in area size. One 10x10 mm^2 sample mounted on an appropriately sized holder is shown in Figure 3.3. For cleaning purposes, substrates were ultrasonically cleaned in acetone and then isopropanol followed by drying with dry nitrogen. In some cases, substrates were air annealed to control the surface termination of a crystalline template.

Chapter 4

Thin Film Characterization

In this chapter, different characterization techniques are discussed that are employed to uncover the properties of epitaxial thin films, surfaces, and interfaces grown by hybrid molecular beam epitaxy (hMBE). Before atmospheric exposure, *in-situ* RHEED is used to monitor the growth and *in-vacuo* XPS is used as a surface sensitive probe to characterize chemical composition, stoichiometry, valence band features, and oxidation state of cations. Ex-situ XRD, AFM, STM, LEED/LEEM and XAS are employed as needed to characterize the properties and related physics of the hMBE grown epitaxial thin films.

4.1 Reflection High Energy Electron Diffraction

Modern epitaxial thin film growth techniques such as molecular beam epitaxy (MBE) and pulsed laser deposition (PLD) are coupled with reflection high energy electron diffraction (RHEED) to monitor the growth of epitaxial thin films in real time. RHEED, a surface sensitive technique, uses electron energies of 5 to 100 keV provided by an electron gun. When an electron beam is incident at a glancing incidence on a sample surface, the diffracted electrons interfere and satisfy Laue's condition, resulting in diffraction patterns [133,134] on a phosphor screen as shown in Figure 4.1. Positions on the diffraction pattern are reciprocal-space representations of physical distances between unit cells of the sample surface. The diffraction pattern from the RHEED image can be used to track the epitaxial growth in real time, allowing for the prediction of a variety of film characteristics such as epilayer thickness, growth rate, surface roughness, and surface reconstruction.

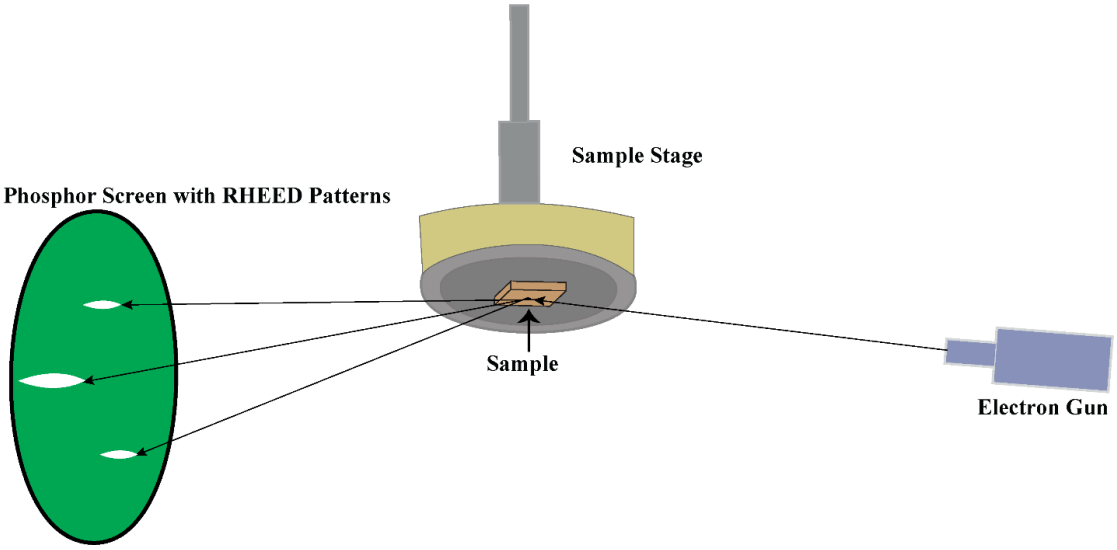

Figure 4.1: Reflection High Energy Electron Diffraction schematic.

RHEED is a highly surface-sensitive technique that generates diffraction patterns when electrons scatter from the top one or two atomic layers of the sample. The diffraction condition is satisfied where an Ewald sphere intersects with reciprocal lattice rods, producing diffraction spots at particular locations according to the crystal structure and quality. These spots often appear as streaks due to undulations caused by domains or point defects on the surface. The width and length of these streaks is determined by the finite size of the in-plane lattice parameter and the incidence angle of an electron beam. Fundamental reflections are streaks that emerge on the 0th order Laue zone. Secondary streaks between the primary streaks also appear in the case of increasing unit cell length and surface reconstruction [135] as shown in Figure 4.2 for homoepitaxial $SrTiO_3$ (STO) film of 20 nm.

The diffraction pattern is formed according to the periodic position of atoms on the sample and is used qualitatively to determine film structure, and can be used quantitatively to determine in-plane

lattice constants. Additionally, RHEED patterns are useful in determining the growth modes such as layer by layer, island, and layer plus island growth in epitaxial film growth [136]. In a layer-by-layer growth mode, the intensity oscillates back and forth and an overall intensity of a RHEED spots remains constant. On the other hand, island growth has step density that varies nonperiodically, and multiple diffuse scattering from various steps may dominate the RHEED electron-scattering process which results to a sharp decline in RHEED intensity and no oscillations in the reflected beam. As a result, RHEED patterns change from 2D "streaky" to 3D "spotty" [137]. A high deposition rate leads to high supersaturation, which increases the chance of large islands on the surface and results in 2D layer-by-layer plus islands growth [138].

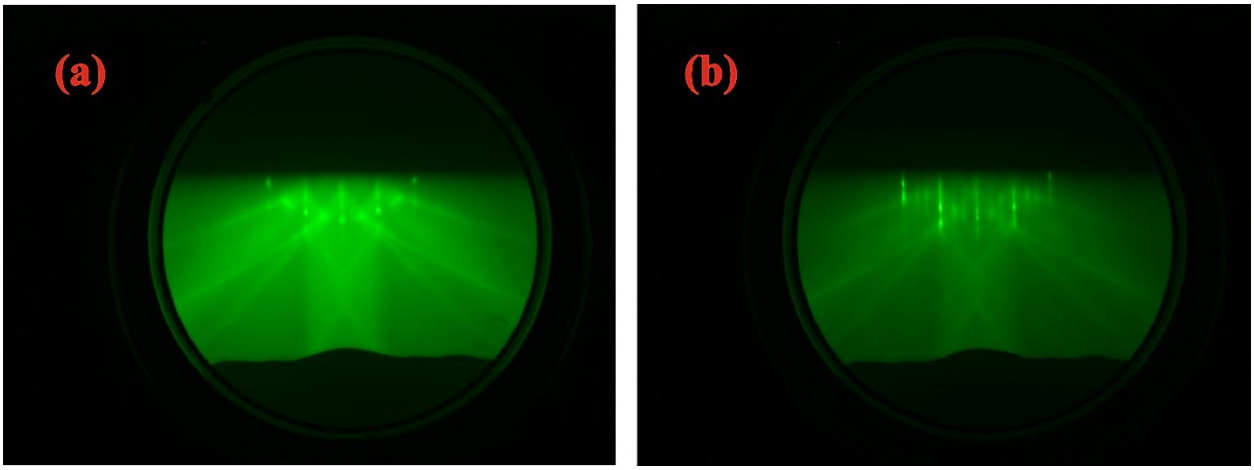

Figure 4.2: (a) $SrTiO_3$ substrate and (b) 20 nm $SrTiO_3$ film on $SrTiO_3$ substrate with surface reconstructions

A uniform structure from bulk to surface is shown by a continuous unchanging RHEED pattern throughout the film growth process, which is the first indicator of a single-crystalline or single-phase film. This also allows for the confirmation of layer-by-layer growth modes in films. After deposition, the oxygen reactivity and stage temperature parameters that are optimal for forming a material may not be adequate for preserving its structure. In case of metastable films such as

$SrNbO_3$ (SNO), oxygen environment plays vital role in over-oxidation of film surfaces during and after the growth. As shown in Figure 4.3, the intensity spots and Kikuchi bands degrade, indicating that the quality of the RHEED pattern lowers while cooling down the sample.

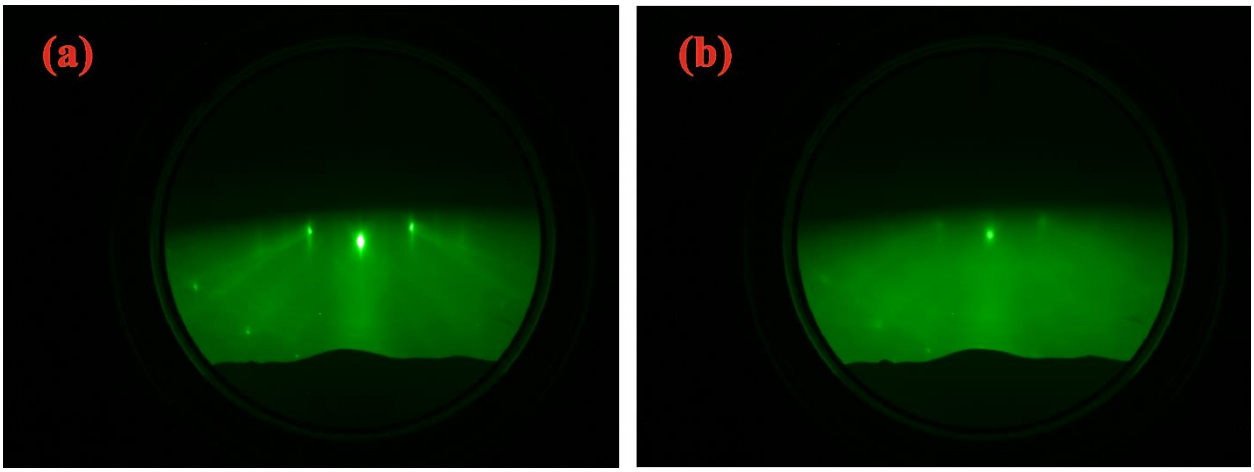

Figure 4.3: $SrNbO_3$ film on $GdScO_3$ substrate (a) hot and (b) cool (room temperature)

4.2 X-ray Photoelectron Spectroscopy

Advances in thin film synthesis by novel growth techniques demands highly efficient characterization tools that can explain the physical origin of emergent phenomena in thin films, surfaces, and interfaces. X-ray photoelectron spectroscopy (XPS) is a well-known surface sensitive characterization technique due to its ability to probe no more than 10 nm in sample depth. Our lab setup for hMBE integrates synthesis with XPS in a single vacuum which creates unique opportunities to examine *in-operando* elemental stoichiometry, valence state and bonding environments of a thin film and its interface. XPS is a powerful technique for accessing chemical effects on a film surface that might have occurred after growth, beginning with sample cooldown all the way to atmospheric exposure.

The principle of XPS is based on the photoelectric effect [139]. When an incident X-ray on a sample knocks out any core level or valence electrons to the vacuum, this is the photoelectric effect. Generally, Mg Kα X-ray (1253.6 eV) or Al Kα X-ray (1486.6 eV) are used as an X-ray source in XPS measurement. In this work, all the measurements were carried out with an Al Kα X-ray source in a PHI 5400 XPS system. The schematic of a typical XPS is shown in Figure 4.4.

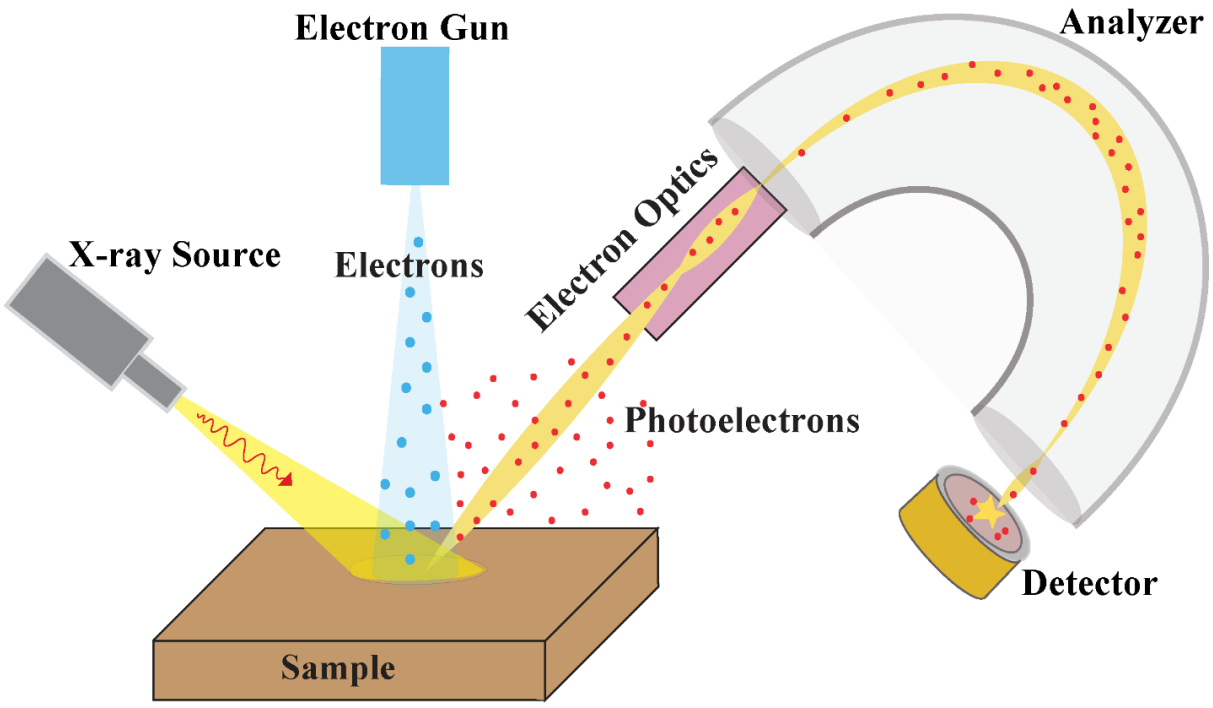

Figure 4.4: X-ray photoelectron spectroscopy system schematic.

The ejected photoelectrons must pass through electron optics and a hemispherical analyzer before encountering the detector. Electron optics includes a two-stage electrostatic lens which focuses photoelectrons onto the entrance slit to the analyzer and deaccelerates them to a kinetic energy value known as pass energy. The main role of an analyzer is to invetsigate the number of photoelectrons at given energies that pass through the entrance slit, where energy resolution is highly sensitive to the choice of pass energy and the width of a selected entrance slit. Depending upon the resistivity of the sample, positive charging effects due to electron loss can make a

significant difference in spectra and cause issues in data collection. To resolve this issue, our lab XPS is equipped with a neutralizer which consists of an electron gun source to shower the sample with electrons during data acquisition and minimize the accumulation of charged holes in a material. Extra care must be taken during data analysis by shifting the binding energies by proper amounts to correct the undesired binding energy shifting effect. The lab set up of the XPS system in Auburn FINO lab (our lab) is shown in Figure 4.5.

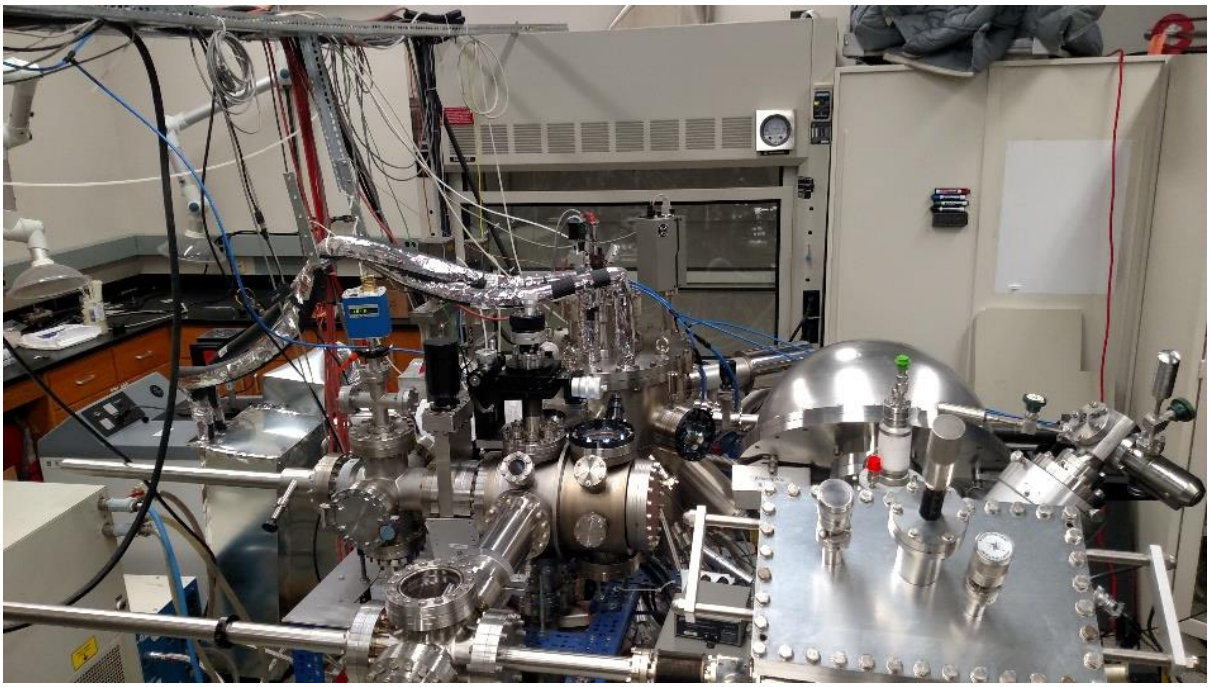

Figure 4.5: Auburn FINO Lab XPS system.

Precise control of x-ray wavelength with the help of monochromator allows us to determine the binding energy (E_B) of a photoelectron via the equation:

$$E_{photon} = h\nu = E_B + \Phi_S + E_{k'} \qquad (1)$$

where Φ_S is the work function of a sample and $E_{k'}$ is the kinetic energy of the emitted electron. As an ejected photoelectron has to pass through the XPS analyzer, an actual kinetic energy of an emitted electron is related to the work function of the XPS, Φ_A, and kinetic energy measured by detector, E_k, as

$$E_{k'} = E_k + \Phi_A - \Phi_S \quad (2)$$

Arranging equation (2) using equation (1), the binding energy of an electron can be calculated as,

$$E_B = h\nu - E_k - \Phi_A \quad (3)$$

Hence, the binding energy of an ejected photoelectron depends upon the XPS instrumentation rather than on the work function of a material and kinetic energy of the emitted electrons.

XPS can measure different types of peaks in spectra from a single measurement, providing signature of multiple phenomena related to the sample. Some of the major peak types observed in XPS measurements are spin doublet, multiplet splitting, shake-up satellite and Auger peaks. When a photoelectron is emitted from an orbital with an angular momentum quantum number, $l > 0$, spin and angular momenta in the final state couples to exhibit two core level peaks that are called spin-orbit doublet peaks. The second major peak is multiplet splitting, in which spin and angular momenta of electrons in different core orbitals of a photoionized atom can couple with unpaired valence electrons of the same atom to produce multiplicity in the final states. This phenomenon is common in transition metal ions that have partially filled orbitals. Among many other properties of a material, the ionic nature of photoionized materials forces valence electrons to undergo charge rearrangement among the available orbitals. When a valence electron is excited to an unoccupied state of higher energy, it gives rise to another major feature at a lower kinetic energy of the primary

core level known as shake-up peaks. These peaks are useful to determine bonding environment within the materials. On the other hand, Auger peaks are one of the routinely observed major peaks in XPS spectra. These peaks appear when rearranging valence electrons produces enough energy to knock out secondary electrons from the atom. These peaks are useful for elemental identification though they often impose complications in quantification when they appear close to core level peaks.

As discussed above, peak position, shapes, and intensities from XPS measurement largely helps to characterize epitaxial thin films, surfaces, and interface. Core level relative peak heights from XPS scans can provide rough estimates of the cation ratios in a material for stoichiometry. More precisely, areas under the core level peaks calculated with appropriate constraints are a useful means to check the stoichiometry of a sample especially in the case of *in-vacuo* XPS. Along with stoichiometry determination, contaminants, surface terminations, oxide surface chemistry, interfacial chemistry and intermixing, band alignment and interfacial charge transfer can be quantified from XPS spectra.

4.2.1 X-ray Photoelectron Spectroscopy Scans

Before acquiring data, a sample must be aligned using alignment knobs at three dimensions to maximize the electron counts collected by the detector. Also, charging effects must be minimized as much as possible by adjusting the emission current with the neutralizer set up using the electron flood gun. The use of an electron flood gun is crucial for samples grown on the non-conducting substrates with large band gap such as $GdScO_3$, as they exhibit a strong charging effect. The use of an electron flood gun creates complexity primarily in valence band analysis which is vital for band alignment if epitaxial heterostructures. After sample alignment, XPS spectra can be acquired

by scanning a sample in two different modes. One is known as a survey, and the other is a multiplex.

4.2.1.1 Survey Scan

Surveys are quick but broad scans within a large energy range (1400 eV to -10 eV, in our case) with a high pass energy (178.5 eV) at the expense of energy resolution. This scan reveals most of the elemental signatures present in the material as shown in Figure 4.6 in case of SNO epitaxial thin films grown on STO substrate. Film thickness can be calculated from an XPS survey scan by referring to the intensity of substrate signature peaks if the probing thickness of the XPS is available. In Figure 4.6, Sr 3*d* signal is coming from both the substrate and the film, while Ti 3*d* signal is exclusively from the substrate, and the appearance of a Ti 3*d* peak indicates that the film is not thick enough. In this way, XPS probes to the substrate through the film. Because any shared elemental composition between a film and a substrate makes characterization of the sample stoichiometry difficult, even during *in vacuo* XPS, extra caution must be taken while selecting the substrate for epitaxial ultra-thin film growth. On the other hand, relative peak heights from the survey scan can be used to estimate the stoichiometry of the sample. Additionally, contaminants in the sample can be inferred from the signature of their elemental peak in a survey scan. In an *ex-situ* XPS, contaminants are usually hydroxides and hydrocarbons from atmospheric exposure. *In-situ* XPS does not have to deal with these contaminants, so that these impurities can be largely reduced or eliminated, which is greatly advantageous in ultraclean thin film synthesis for studying surfaces and subsequent interfacial properties [140]. Most importantly, XPS survey scans are critical in establishing a better growth recipe for speeding the growth process.

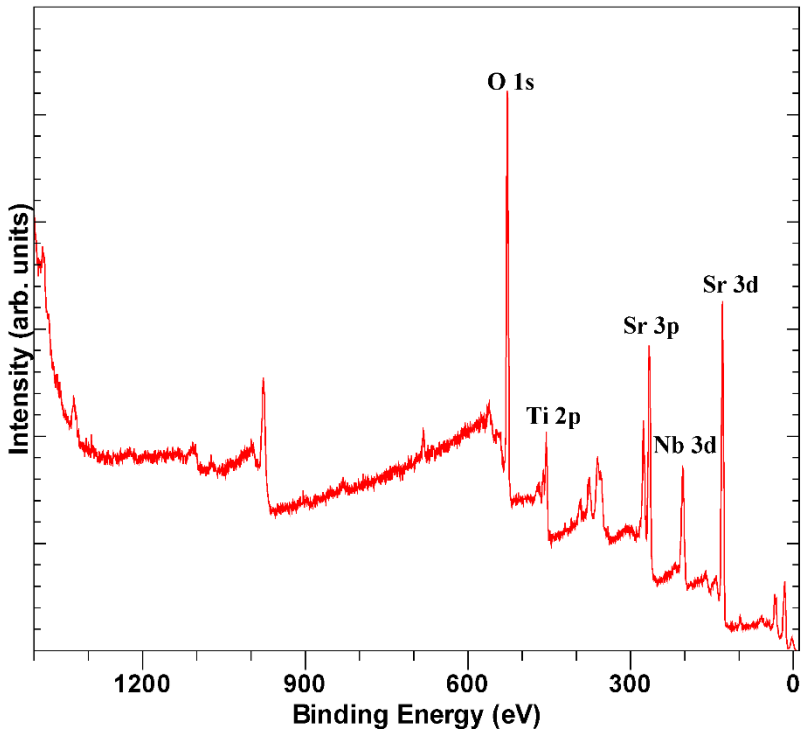

Figure 4.6: XPS survey of $SrNbO_3$ film on $SrTiO_3$ substrate.

4.2.1.2 Multiplex Scan

Multiplexes are scans of individual core levels with a low pass energy (35.5 eV) that maintains a higher energy resolution. As the area under the curve of a core level can be used to compute the quantity of atomic sites, core level scans are crucial in evaluating the stoichiometry of a sample. Peak positions of the core level and the presence of any extra peaks are clearly visible in this scan as shown in Figure 4.7 for Nb 3*d* core level in a SNO growth sample. The presence of an extra peak at lower binding energy besides the core level peaks is indication of a niobium oxidation state lower than a 5+ state. The peak position, which is critical in determining the binding energy of a metallic site, can be shifted by different bonding environments. The existence of an additional peak closer to the main core level peak indicates a mixed oxidation state of an element.

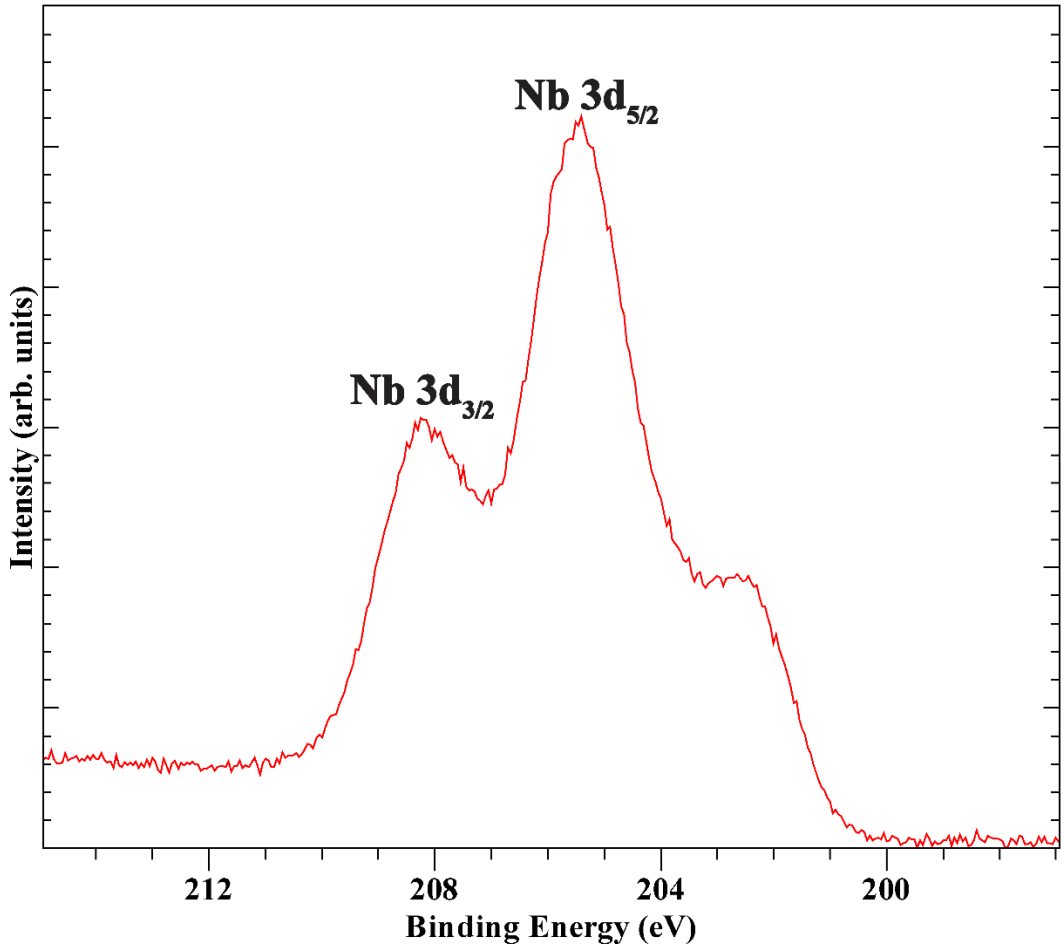

Figure 4.7: Nb 3*d* core level from $SrNbO_3$ film grown on Nb doped $SrTiO_3$.

4.2.1.3 X-ray Photoelectron Spectroscopy Data Analysis

Among three different file formats obtained from XPS scan, ".txt" format can be used to analyze the XPS data. Different software can be used to quantify the data for XPS analysis, including CasaXPS [141,142], which is used in this work. CasaXPS is a user-friendly XPS data analyzing tool to make choices on background types for background subtraction, and for creating multiple artificial components with built-in constraints during analysis. Among backgrounds, one is the widely used Shirley background which is used in this work to subtract a proper background from spectra while quantifying the core level areas. While comparing the core level peak shapes and

intensities among different samples, the overlaying option in CasaXPS is beneficial for assessing stoichiometry and chemical state. One of the important features in data analysis is the quantification of core levels where major characteristics of a sample are buried. The primary core level can be broken down into multiple components to represent the different oxidation states of an element which is useful in finding stoichiometry, bonding environment, and chemical state of a material.

4.3 X-ray Diffraction

X-ray diffraction (XRD) is a bulk sensitive technique where diffraction occurs when elastically scattered X-rays from the atoms of a crystal interfere constructively. To achieve a diffraction phenomenon in crystals, X-rays of wavelength between 0.5 Å to 5 Å are required since crystals made up of regularly spaced atoms often have interatomic spacings of a few angstroms. An X-ray source of Cu $K\alpha$ having wavelength of ~1.54 Å is often used to carry out XRD measurements. The XRD uses the size and orientations of the unit cells of materials to provide structural information [143]. Notably, the periodicity of the lattice allows diffraction from a crystal in specific directions that satisfy Bragg's law [144]. According to Bragg's law, when a beam of parallel and monochromatic X-rays is scattered from a crystal made up of atomic planes separated by d_{hkl}, constructive interference occurs when the path difference between the interfering X-rays ($2d_{hkl}\sin\theta$) is an integer multiple of the wavelength (λ), written as

$$2d_{hkl}sin\theta = n\lambda$$

where θ is the angle formed by the incident beam and the crystal surface, and n is the reflection order. As a result, intensity maxima are detected at specific angles known as Bragg angles, which

are characteristic of the planar distance d_{hkl}. The interplanar spacing (d_{hkl}) is related to the lattice parameter (a) of a cubic crystal as

$$d_{hkl} = \frac{a}{\sqrt{h^2 + k^2 + l^2}}$$

Hence useful information on symmetry, lattice parameters, texture, grain size, and microstrain can be collected by the diffraction pattern [145]. In this study, high-resolution X-ray diffraction (HRXRD) is carried out to check the thin film crystallinity and for estimation of thicknesses of an epitaxial film.

4.3.1 High Resolution X-ray Diffraction

High resolution X-ray diffraction (HRXRD) is a collection of non-destructive analysis processes for crystalline structured materials that are mainly layered and nearly perfect. Understanding the structural properties that can be revealed and quantified are crucial for the successful utilization of such materials. A monochromatic X-ray beam with a well-defined wavelength spread and low angular divergence is required for HRXRD experiments on epitaxial layers, heterostructures, and superlattice systems. Compared to regular XRD, HRXRD is suited with monochromators that can filter out Cu $K\alpha_2$ along with other undesired radiation that plays a role in improper constructive interference due to different wavelengths from the X-ray source. Out-of-plane XRD scanning is one of the popular scan modes in HRXRD to obtain structural information of thin film single crystals. In this work, out-of-plane XRD spectra of SNO samples were gathered using a Rigaku SmartLab diffractometer system with a Cu $K\alpha_1$ source filtered appropriately for thin film samples using a parabolic mirror and double bounce Ge (220) monochromator. Also, 2θ-ω scans on the (002) reflection of the STO samples using a Malvern Panalytical X'Pert3 Diffractometer with a

four-circle goniometer and a Cu $K\alpha_1$ radiation line isolated with a double bounce Ge (111) monochromator was employed.

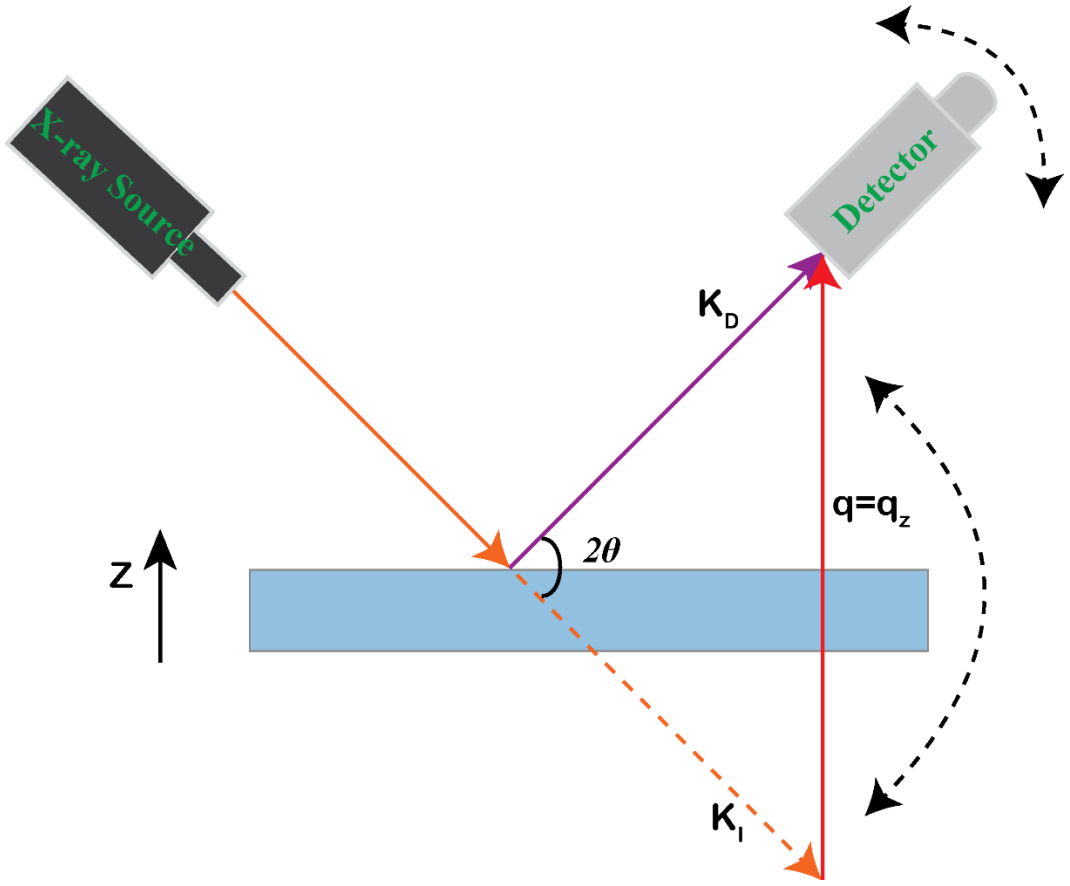

Figure 4.8: Specular diffraction where scattering vector $\boldsymbol{q}$ is connected to incident wave vector $\boldsymbol{K_I}$ and diffracted wave vector $\boldsymbol{K_D}$.

Out-of-plane XRD, is well suited to examine thin films with homogeneous crystal orientation, such as STO and SNO, because it is solely sensitive to the out-of-plane lattice direction. According to Bragg's law, highly crystalline samples produce peaks at specific X-ray path angles, and the presence of these characteristic peaks validates the crystal lattice. The scattering vector, $\boldsymbol{q}$ is defined as, $\boldsymbol{q} = \boldsymbol{K_D} - \boldsymbol{K_I}$ where $\boldsymbol{K_D}$ and $\boldsymbol{K_I}$ are diffracted and incident wave vectors, respectively. When specular diffraction occurs, the scattering vector, $\boldsymbol{q}$, points in the z-direction and its

magnitude can be expressed as, $q = q_z = 2k \sin\theta = \frac{4\pi}{\lambda}\sin\theta$ when the crystallographic planes are parallel to the crystal surface, as illustrated in Figure 4.8. This is because the wave vector can be expressed as $k = \frac{2\pi}{\lambda}$.

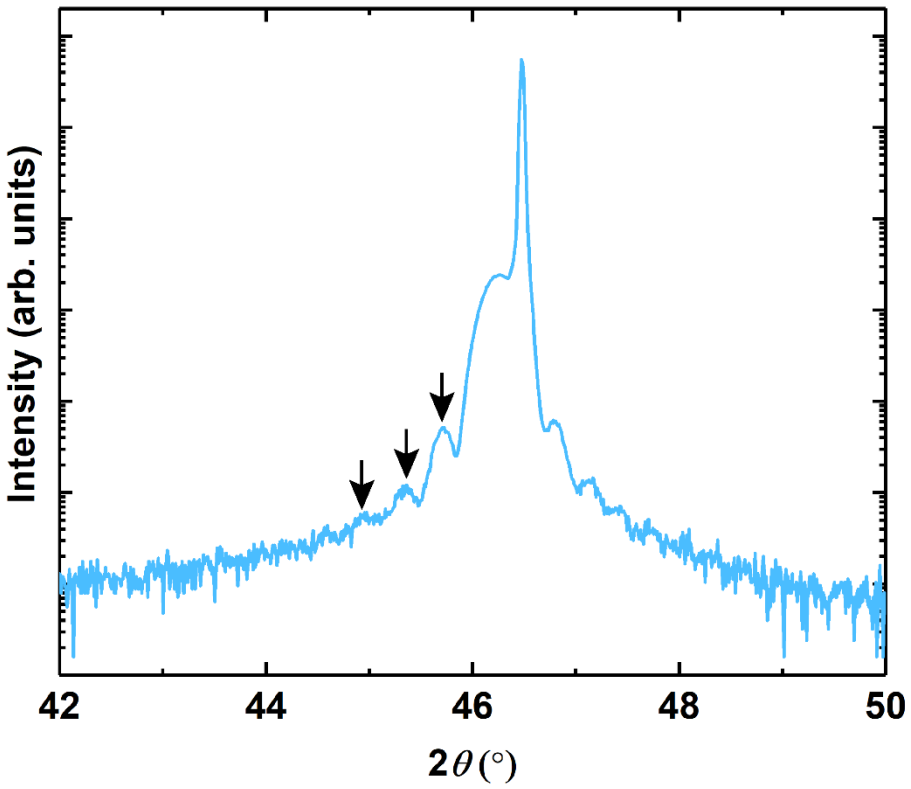

Figure 4.9: High resolution X-ray diffraction patterns for 20 nm $SrTiO_3$ film on $SrTiO_3$ substrate with Keissing fringes labelled.

Another noteworthy feature is the Kiessig fringes of the Bragg peak, as shown in Figure 4.9 for the homoepitaxial STO film. The reflected X-rays from the surface of a film and the interface between the film and the substrate interfere constructively and destructively, forming a series of fringes around the Bragg peak to form Kiessig fringes [146]. Substrate peaks are significantly sharper and higher in intensity compared to the film peaks due to their greater thickness. Presence of these fringes provides the signature of atomically smooth films and substrate interfaces.

Additionally, the fringes' frequency can also be used to calculate the film thickness. In HRXRD measurements, a highly crystalline single-phase films with nanometer range thickness shows a clear peak position which can be used to calculate the out of plane lattice parameters using the Bragg equation.

4.4 Atomic Force Microscopy

Atomic force microscopy (AFM) is one of the routinely used experimental tools for characterizing a sample surface. The AFM is capable of extracting information on surface roughness, friction, thickness, conductivity, capacitance, dislocations, and homogeneity of the scanned surface. The AFM is sophisticated with very sharp tip cantilever as shown in Figure 4.10 to scan over the surface of the sample. Depending on the attractive or repulsive force between the tip and the sample surface, the cantilever deflects towards or away from the surface of the sample respectively. During the measurement, a laser beam reflected from the flat surface of the cantilever is focused at the surface of a position sensitive photodiode to detect the deflection of the cantilever [147]. Raised and lowered features of topography variance on the surface of a sample influences the deflection of the cantilever which is monitored by the position sensitive photodiode. The feedback loop is used to control the force (or height) of the tip above the surface so that the magnitude of the force between the tip and the sample surface is kept minimum. Following all these steps, AFM generates an accurate topographic map of the surface of a sample.

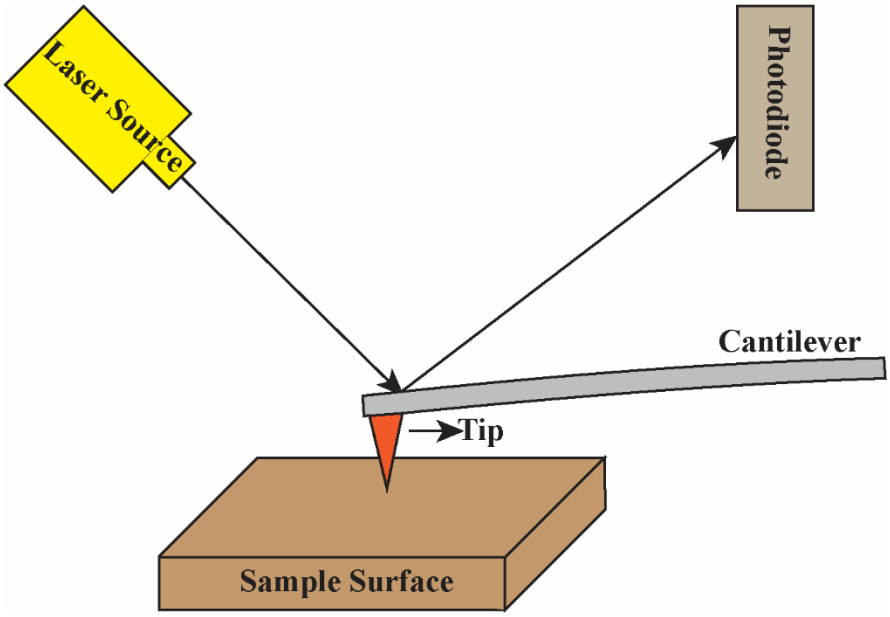

Figure 4.10: Schematic of Atomic Force Microscopy set-up.

Based on the interaction of the tip and the sample surface, AFMs operate in contact mode (repulsive), non-contact mode (attractive), or tapping mode [148]. In this work, non-contact mode scans were performed on epitaxially grown STO and SNO thin films. Contact mode scans provide comparatively higher resolution images than non-contact mode, but the electrostatic and tension forces pull the scanning tip toward the surface which can damage the sample and distort the image data. On the other hand, tapping mode is used for scanning very soft and fragile samples thereby excluding destructive forces but still reaching high-resolution images. Using Park Systems' XE7 AFM, we have performed AFM scans of varying topography map areas as large as 5 x 5 μm^2 to measure the root-mean-square (rms) surface roughness of the hMBE grown epitaxial perovskite oxide thin films.

4.5 X-ray Absorption Spectroscopy

X-ray absorption spectroscopy (XAS) is a commonly used technique in a variety of disciplines to determine the chemical state of a material. XAS is a popular bulk-sensitive experimental technique

that offers information on atomic valence, coordination, and bond lengths among other material properties. In this technique, inner core level electrons are knocked out from the atom to an outer unoccupied valence state, and another inner-shell electron will then fall back producing secondary x-rays (fluorescent x-ray) [149]. This is why the approach is also known as x-ray in and x-ray out technique. The XAS measurement requires highly energetic but continuous-wavelength x-ray sources that demands reservation of beam time at synchrotron facilities such as those found at national laboratories. The range of incoming X-ray energy that excite 1s electrons to unoccupied states is referred to as the K-edge area of the XAS spectra. Although different absorption edges can be acquired from XAS spectra, the K-edge is most frequently carried out since it is simpler to analyze without missing valuable information.

XAS spectra are subdivided into two regions: X-ray absorption near edge structure (XANES) and extended X-ray absorption fine structure (EXAFS). The K-edge shelf, which is a huge increase in intensity that signifies incident X-ray energy that is sufficient to excite 1s electrons to unoccupied states, is the most prominent characteristic of XANES. Pre-edge peaks that emerge due to structural factors such as coordination environment of the cations is another feature of XANES. Relative shifts of the K-edge shelf towards higher binding energy in the XANES region indicates a higher cation valence. Pre-edge peaks can be seen in K-edge XAS spectra at energies below the characteristic K-edge shelf. Multiple material qualities such as symmetry, and structural deformation are inferred by these pre-edge peaks. EXAFS shows periodic variations in fluorescent X-ray intensity that come from the interaction of excited 1s electrons with neighboring atoms. In this study X-ray absorption near edge spectroscopy (XANES) is carried out on the Nb *K*-edge to check the oxidation state of Nb atoms. All XAS Fluorescence data was collected at the Advanced Photon Source of Argonne National Laboratory at Sector-20 BM.

4.6 Scanning Tunneling Microscopy

The scanning tunneling microscope (STM) involves a surface-sensitive probe that can image surfaces at the atomic level and also provides a three-dimensional profile of the surface. The STM works by the principle of quantum tunneling effect. Since STM measurements require a closed electrical loop to flow tunneling current, samples must be prepared on conducting substrates to carry out the measurements. For imaging, an electrochemically etched tungsten tip is employed. When an electric potential difference is set up between the tip and the sample, electrons from a sample tunnel through the tip. The amplitude of the tunneling current is determined by the surface of the sample. Larger distances between the surface and the tip means lower tunneling current, and smaller distances between the surface and the tip means higher tunneling current. Eventually, the amplitude of the tunneling current produced by tunneling electrons is amplified and is sent to a computer to generate data and plots. STM results were presented in chapter 5 as measured by an Omicron Nanotechnology Variable Temperature Scanning Probe Microscopy (VT-SPM) system, and the topography images were analyzed with the open-source software, Gwyddion [150].

4.7 Low Energy Electron Diffraction/Microscopy

The diffraction patterns in low energy electron diffraction (LEED) are obtained by using an electron gun that produces monochromatic low energy electrons (10-600 eV). If the crystal surface is as wide as the electron beam De-Broglie wavelength, elastically backscattered electrons diffract that satisfy Laue's condition. Qualitatively, LEED is advantageous in mapping symmetry of the surface structure and is useful to study crystal reconstruction at the sample surface. On the other hand, I-V curves can be fitted to provide accurate atomic positions at the sample surface. In low energy electron microscopy (LEEM) measurements, the high energy electrons (10-20 keV) are retarded before reaching the sample surface with lower energy (10-100 eV) and are back-

accelerated when reflected off the surface beyond the objective lens. For bright field imaging, a specular reflected beam is used while frequently diffracted beams are used for dark field imaging. In this work, both LEED and LEEM measurements were carried out in the XPEEM/LEEM endstation of the electron spectro-microscopy (21-ID-2) beamline at the National Synchrotron Light Source II [151].

Chapter 5

Surface Stability in $SrTiO_3$ Thin Films Grown by Hybrid Molecular Beam Epitaxy

Suresh Thapa, Sydney Provence, Wencan Jin, and Ryan Comes

Physics Department, Auburn University, Auburn, AL, 36849, USA

Devin Jessup and Petra Reinke

Department of Materials Science and Engineering, University of Virginia, Charlottesville, VA, 22904

Jason Lapano and Matthew Brahlek

Materials Science and Technology Division, Oak Ridge National Laboratory, Oak Ridge, TN, 37830

Jerzy T. Sadowsky

Center for Functional Nanomaterials, Brookhaven National Laboratory, Upton, NY, 11973

Published in *Journal of Vacuum Science and Technology A*, **39**, 053203, Sep 2021. DOI: 10.1116/6.0001159. Reprinted with permission of publisher, *American Vacuum Society*.

Abstract: Hybrid oxide molecular beam epitaxy (hMBE), a thin-film deposition technique in which transition metal cations are delivered using a metal-organic precursor, has emerged as the state-of-the-art approach to the synthesis of electronic-grade complex oxide films with a stoichiometric growth window. However, numerous questions remain regarding the chemical mechanisms of the growth process and the surface properties of the resulting films. To examine these properties, thin film $SrTiO_3$ (STO) was prepared by hMBE using a titanium tetraisopropoxide (TTIP) precursor for Ti delivery and an elemental Sr source on annealed STO and Nb-doped STO substrates with varying TTIP:Sr flux ratios to examine the conditions for the reported

stoichiometric growth window. The films were transferred *in vacuo* to an x-ray photoelectron spectroscopy system to study the surface elemental composition. Samples were examined using x-ray diffraction to compare our surface sensitive results with previously reported measurements of the bulk of the films in the literature. *Ex situ* studies by atomic force microscopy, scanning tunneling microscopy and low energy electron microscopy confirmed the presence of surface reconstructions and an Ehrlich-Schwoebel barrier consistent with an A-site SrO termination. We find that a surface exhibiting a mixture of SrO and TiO_2 termination, or a full SrO termination is necessary to obtain stoichiometric adsorption-controlled growth. These results indicate that surface Sr is necessary to maintain chemical equilibrium for stoichiometric growth during the hMBE process, which is important for the design of future interfacial systems using this technique.

5.1 Introduction:

Novel properties governed by the polar discontinuity at a heterojunction have been a central focus of oxide thin film research for over a decade. The electronic reconstruction at the interface due to the polar discontinuity between oxides layer can generate high mobility two-dimensional electron gas (2DEG) [152,153]. Atomic-scale control of interfacial terminations between polar and non-polar materials has led to a variety of emergent phenomena with potential applications for energy and electronic technologies. Beyond 2DEG systems, studies of polar/non-polar $LaFeO_3/SrTiO_3$ interfaces [154–156] and the subsequent demonstration of photocatalytic behavior [157] reflects the importance of understanding interfacial structures and defects in these materials with a great deal of precision for future electronic and energy devices. To engineer these materials, however, careful control over the synthesis process is required, which has led to the continued improvement of epitaxial growth techniques.

The epitaxial growth of atomic scale complex oxide thin films has been achieved by pulsed laser deposition (PLD) and molecular beam epitaxy (MBE) over the past 30 years. However, compared to the growth of traditional semiconductors, growth of complex oxides is challenging due to the lack of an adsorption-controlled growth window in MBE. Established oxide MBE employs effusion cells for each element, and recipes have been developed for the growth of $SrTiO_3$ (STO) and other materials that typically use alternating deposition of the *A*-site and *B*-site cations, allowing for stoichiometry control down to ~1% precision [158]. Achieving even more precise stoichiometric control, which is necessary for control of defect and dopant inventories, however, has proven challenging. Additional difficulties arise from the challenge to maintain stable evaporation rates for low vapor pressure and

refractive elements in the requisite oxygen environment. These challenges can be overcome by using metal-organic precursors rather than elemental sources, which are promising alternatives to traditional oxide MBE. Hybrid MBE (hMBE) is a well-known technique for the implementation of mixed type sources combining elemental effusion cells for *A*-site cations and metal organic precursors for transition metal *B*-site cations in reactive oxygen sources.

Epitaxial growth for several refractory metal oxides, including vanadates, zirconates, and titanates, relies on hMBE [159–166]. Unexpectedly, hMBE was found to exhibit an adsorption-controlled growth window for stoichiometric STO growth when a titanium tetraisopropoxide (TTIP) precursor was used for titanium delivery in conjunction with evaporation of Sr from a conventional effusion cell [164]. The self-regulated growth window provides an avenue to control the stoichiometry of both the cations and anions which compensates unavoidable drift in effusion cell fluxes over the course of the growth. The presence of a growth window for STO via hMBE is now well-established and has led to the highest mobility *n*-STO films on record [163,167]. STO is one of the most widely studied perovskite oxide structures in terms of bulk and surface properties due to its unique properties along with the simple cubic structure. A growth window has also been reported for several other materials, including $SrVO_3$ [165] and $BaSnO_3$ [168], yielding some of the best electronic properties reported to date in these materials. However, evaluating the presence of a growth window for STO and other complex oxides has focused primarily on bulk parameters to determine if defects are present within the material. X-ray diffraction (XRD) studies of the strong dependence of the film lattice parameters on stoichiometry have traditionally been used to evaluate the growth window [2,8–11]. However, XRD and transport measurements are primarily sensitive to the bulk properties of a film and surface studies of hMBE films have been quite limited. Understanding the film surface is critical for the

engineering of emergent properties across dissimilar interfaces including polar/non-polar heterostructures.

To date, in most heterostructures grown by hMBE only the *A*-site cation has been varied, while chemical continuity was maintained across the *B*-site [171–173]. However, in multilayer structures combining dissimilar *A*-site and *B*-site cations, control of the interfacial termination is critical to designing functional properties [154,174,175]. The surface of hybrid-grown STO films is at present poorly understood, and growth of complex heterostructures is difficult to achieve in a controlled and predictive manner. Furthermore, in spite of decades of studies, the stability of various STO surface terminations and reconstructions is still a matter of great debate [176–179]. In the case of hMBE growth, these studies are confounded by the growth environment, where the residue of the metal-organic precursor may introduce carbon and hydrogen as well as the transition metal cation. In most STO hMBE film growth, *in situ* reflection high energy electron diffraction (RHEED) has been applied to monitor the growth in real time domain, though *in-vacuo* X-ray photoelectron spectroscopy (XPS) studies have never been reported. RHEED measurements have been important for quantifying the surface reconstructions to establish a growth window, with reports that a c(4×4) surface reconstruction is indicative of the best film stoichiometry as determined through XRD and electron mobility measurements [161]. However, the actual surface termination and chemistry of hybrid-grown STO films has never been reported, which is the subject of this work.

Here we focus on characterization of the surface stoichiometry of the hMBE grown film using *in vacuo* XPS [180] and quantify the critical growth window. Measurement of the surface termination and bonding of hMBE grown oxides delivers the relationship between surface chemistry and the growth window, which has previously been reported for the bulk material and was established with

XRD. The *in-vacuo* characterization eliminates efficiently carbon contamination, [162], as well as determination of water and hydrogen adsorption due to residual hydrocarbons in the growth chamber after TTIP decomposition [177]. We examine the surface of STO films grown by hMBE using *in situ* and *ex situ* surface techniques, including RHEED, XPS, scanning tunneling microscopy (STM), and low-energy electron diffraction and microscopy (LEED/LEEM) to understand the stable surface under the unusual growth conditions present during hMBE. We show that the presence of surface SrO is crucial to the growth of stoichiometric STO and subject to a complex surface chemistry which is not yet well understood.

5.2 Experiment:

STO thin films were grown on air annealed 10×10×0.5 mm^3 (001) STO single crystal substrates (MTI Crystal) in a Mantis MBE reactor with a baseline pressure of ~10^{-9} Torr. Air annealing of the STO substrates in a tube furnace at 1000 °C maintains a mixed surface termination of TiO_2 and SrO because no buffered oxide etching was employed [181]. The substrates were ultrasonically cleaned in acetone and isopropanol respectively and dried with dry nitrogen gas. All substrates were cleaned in oxygen plasma in the MBE growth chamber by ramping to the 1000 °C growth temperature over ~1 hour as measured by thermocouple [160,161]. We estimate that the setpoint is ~150-200 °C higher than substrate surface temperature due to the absence of backside substrate metallization, resulting in an STO surface temperature between 800 and 850 °C. Growth and cleaning were performed in a background pressure of ~3×10^{-6} Torr O_2 with an RF plasma source driven at 300 W to supply O atoms to increase oxygen chemical potential at the substrate surface. Strontium (99.99%, Sigma-Aldrich, USA) was supplied through a low temperature effusion cell. The Sr flux was calibrated using QCM under oxygen environment with a chamber pressure of 3×10^{-6} Torr. Titanium was supplied through a gas source using a metalorganic precursor TTIP (99.999%, Sigma-Aldrich, USA) from a bubbler that

was connected through the gas inlet system to the growth chamber [160]. No carrier gas was used. The growth chamber shroud walls were maintained at -30 °C via a closed loop chiller and low temperature fluid (Syltherm XLT, Dow Chemical) to reduce the background water vapor pressure from the dissociated TTIP molecules. However, the chamber pressure measured by cold cathode gauge generally increases and reaches up to ~5×10^{-6} Torr for the first 5-10 minutes during growth before stabilizing due to the dissociated and unreacted TTIP injected into the system. The plasma was left on while cooling the film to below 300 °C. An additional sample was prepared on an annealed STO substrate by depositing one monolayer of SrO to produce a nominally SrO-terminated STO sample for XPS calibration.

A series of seven samples was grown at differing TTIP:Sr flux ratios where the Sr flux was held fixed and the TTIP gas inlet line pressure was varied. Samples are coded numerically throughout this work by the ratio of the pressure of the TTIP in the gas injection line in mTorr to the flux of SrO measured by quartz crystal microbalance (QCM) in Å/sec. While the units of these numbers cannot be compared to the literature, they serve as a proxy for comparison to reports made by other groups using beam flux pressures [160]. Drift in the Sr flux during the course of the growth is the primary source of uncertainty in TTIP:Sr flux ratios and is assumed to produce a 2% error bar in the ratios, which is consistent with other reports of cell drift [182].

In situ RHEED (Staib Instrument) was used to monitor the growth process and the quality of the film. RHEED intensity oscillations were used to estimate the growth rate, which was corroborated by measuring the spacing of the interference fringes in XRD scans to calculate the film thickness and dividing by the overall growth time. Growth rates were ~4.5 Å/min. Videos of the RHEED patterns were recorded and analyzed using k-means clustering and principal component analysis (PCA) codes

developed at Auburn and inspired by previous work by Vasudevan et al. [183]. PCA compresses the data while retaining the most statistically relevant features, producing a new dataset of orthogonal principle components and time-dependent loadings. The reduced data set is grouped into time clusters using k-means clustering, an unsupervised machine learning technique that groups the frames based on their statistical distance to the mean image of the cluster. This analysis captures any changes or transitions in the RHEED pattern at the time of occurrence in the growth. More information about this technique is described elsewhere [184].

Post-growth the samples were transferred from the MBE reactor to the PHI 5400 XPS (monochromatic Al Kα X-ray source) system through ultra-high vacuum (UHV) transfer line [180]. Core level peaks were measured with a pass energy of 17.9 eV. An electron neutralizer gun was applied to compensate charging of the insulating samples. The surface stoichiometry of all grown samples was characterized by analyzing core level XPS spectra measured with base pressure of ~1×10^{-9} Torr. Analysis of the XPS data was performed using CasaXPS, with a Shirley background subtraction and Gaussian-Lorentzian (Voigt) peak shape. To properly align all core level peaks, the O 1s peak was aligned to place the lowest binding energy peak at 530.0 eV, which corresponds to oxygen bonded to metal cations in the STO film. Measurements were made at 45° and 70° electron takeoff angles to vary the degree of surface sensitivity, with 45° providing a more bulk-sensitive probe of stoichiometry and 70° a more surface-sensitive. We assume in our analysis that electron forward focusing effects, commonly referred to as X-ray photoelectron diffraction, are negligible between samples. A Malvern Panalytical X'Pert³ Diffractometer equipped with a 4-circle goniometer and using Cu $K\alpha_1$ radiation line isolated with double bounce Ge (111) monochromator was used for 2θ-ω scans on the (002) reflection of the STO samples.

Further LEED/LEEM measurements were carried out in the XPEEM/LEEM endstation of the Electron Spectro-Microscopy (ESM, 21-ID-2) beamline at the National Synchrotron Light Source II [185] on an STO sample grown on a Nb-doped STO substrate. The sample was degassed at 120 °C with a pressure of 6×10^{-10} Torr for 1 hour. The sample was then annealed in a preparation chamber at a pressure of 2×10^{-6} Torr of O_2 at 500 °C for 30 mins and cooled down in the same pressure of O_2 to room temperature to remove surface contamination. In this system, the electron-beam spot size in the LEED mode is 1.5 μm in diameter and the spatial resolution in the LEEM mode is < 10 nm [186]. The base pressure of the analysis chamber is 2×10^{-10} Torr.

STM was performed on the STO sample grown on a Nb-doped STO substrate with a base pressure of 3.0×10^{-10} Torr using an Omicron Nanotechnology Variable Temperature Scanning Probe Microscopy (VT-SPM) system. Imaging was conducted with an electrochemically etched tungsten tip at ambient temperature, and the topography images were analyzed with the open-source software Gwyddion [187]. The images have been leveled, and the color range was adjusted for the purpose of illustration. The sample was heated to 450°C with 3×10^{-8} Torr of O_2 for 3 hours prior to imaging to remove ambient contamination. Imaging condition, unless stated otherwise, were bias voltage V_{bias}=2.0V, and tunneling current I_t=0.1 nA which yielded the best imaging conditions. The residual roughness on the terraces can be attributed to air exposure of the sample; more aggressive in-situ treatment was avoided to conserve the terrace structure formed after growth. Higher resolution images of the round features on the terraces remained elusive but the morphology on the terraces was observed consistently over the entire sample surface.

5.3 Results and Discussion:

Figure 5.1 shows the RHEED patterns after growth and cool-down for five of the seven samples grown on undoped STO substrates along <110> and <100> azimuth. The RHEED patterns show strong diffraction peaks and additional intermediate peaks due to surface reconstructions in films with low TTIP:Sr flux (ratios of 740, 780, and 856) compared to films with a higher flux ratio. Images for samples 758 and 798 are shown in the Supplemental Information. The strong Kikuchi lines reflect the high crystal quality of the film. Faint surface reconstructions are observed for samples 740, 780, and 856 along (100) and/or (110) but specific determination of the nature of the reconstruction is challenging. Films with higher TTIP:Sr flux (Figure 5.1(d-e)) show streaky RHEED patterns rather than intense spots indicating that the film is Ti-rich with high defect concentrations.

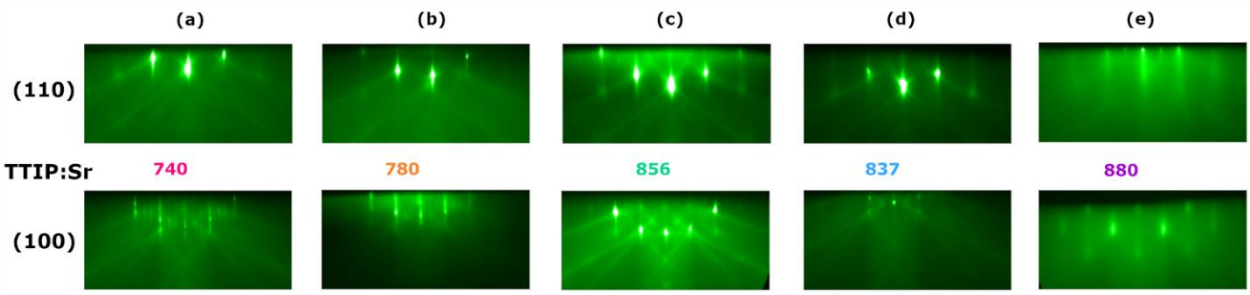

Figure 5.1: RHEED images (a)-(e) along 110 and 100 planes with increasing Ti:Sr peak area ratios as measured by XPS. Color-coded numbers match the samples to those in Figure 5.2. Calibrated flux ratios for each sample are shown in the center.

XPS measurements immediately after growth focused on quantifying Ti:Sr peak area ratios to determine surface and bulk film stoichiometry. Figure 5.2(a) shows the normalized area ratio of Ti 2*p* to the Sr 3*d* core level as a function of TTIP:Sr flux at photoelectrons takeoff angles of 45° and 70°. The dashed grey, red and purple lines represent the *B*-site to *A*-site core level area ratio for an air annealed STO substrate, air annealed Nb-doped STO substrate, and STO substrate after deposition of one monolayer of SrO, respectively. These references were helpful to maintain the same nominal

stoichiometry and cation ratio for the STO film grown on Nb:STO substrate. With increasing TTIP:Sr flux the area ratio also increases, except for the sample with a TTIP:Sr ratio of 856. Deviation in XPS peak area ratios for the 856 sample away from the monotonic increase shown in the other samples is most likely attributable to drift or slight miscalibration in the Sr source flux. As the surface sensitivity of the XPS measurements increases with electron emission angle, the changes in area ratio can be used to infer the primary surface termination of the sample. In fact, simply by changing the STO termination from SrO to TiO_2, one can expect to see a significant change in the Ti 2*p*:Sr 3*d* peak area ratio of approximately 20% (see Appendix A, Supplemental Information Section 1 for details).

In addition to studies of the Sr:Ti cation ratios, possible carbon contamination has also been resolved in the STO films through XPS. As the TTIP precursor contains large amounts of carbon, there have been long-standing questions as to the presence of carbon in the bulk of the film or on the surface [162]. In our core level XPS scan (see Appendix A, Supplemental Information Figure S1), we found the C 1s peak was negligibly small in comparison with the nearby Sr 3p peaks, which could be from the adsorption of carbon during the time required to transfer the sample and perform XPS measurements. Together with previous measurements [162], this suggests that hMBE samples grown with activated oxygen plasma do not have significant carbon contamination. Whether this is also the case for samples grown in molecular oxygen will be determined in future work.

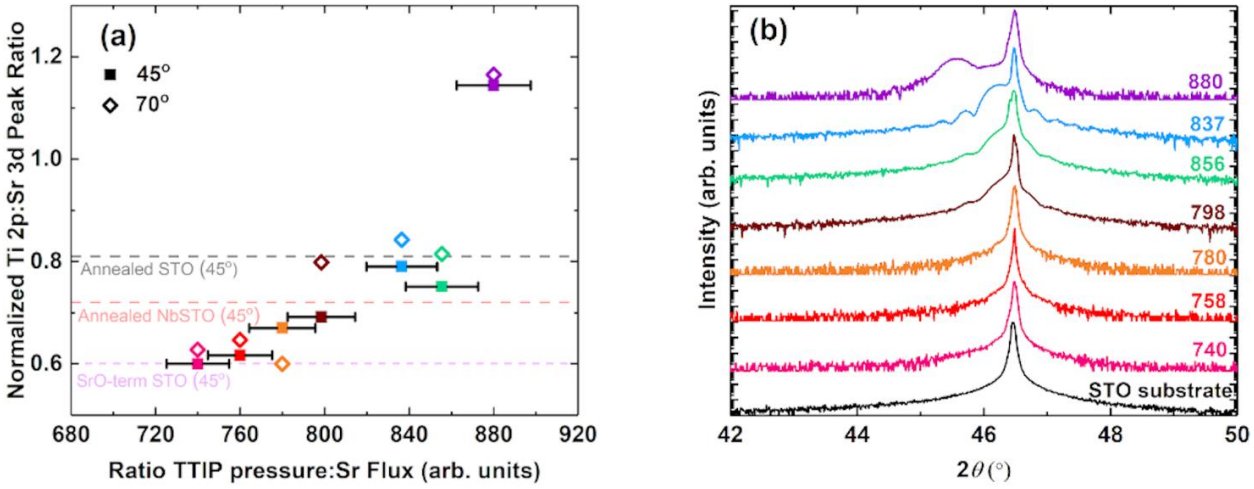

Figure 5.2: (a) Normalized area ratio of Ti $2p_{3/2}$ to Sr $3d_{5/2}$ as a function of TTIP pressure to Sr flux ratio at 45° and 70° electron emission angle in XPS. Error bars for the peak area ratios are smaller than the graphical data points. (b) Intensity as a function of 2θ for XRD scans on (002) Bragg peak.

In Figure 5.2(b), XRD scans are shown for all seven films along with an air annealed plain STO substrate (black). A single XRD peak for a homoepitaxial film results from out-of-plane lattice matching between the substrate and film and is indicative of a stoichiometric sample with a pristine film-substrate interface with no contamination from atmospheric elements such as carbon [169]. Off-stoichiometric samples produce a secondary film peak at smaller values of 2θ consistent with a larger out-of-plane lattice parameter. The 740, 758, and 780 samples are stoichiometric whereas the 798 and 856 are slightly off-stoichiometric. The 837 and 880 samples have clear secondary peaks indicating significant off-stoichiometry in the films.

In comparison to the XRD measurements, XPS is highly surface sensitive. The more bulk sensitive 45° measurements from XPS for stoichiometric samples (740, 758 and 780) reflect a smaller than expected Ti 2*p*:Sr 3*d* ratio when compared to the single crystal references, with ratios between 0.6 and 0.7. At the more surface sensitive 70° emission angle, we observe that the Ti 2*p*:Sr 3*d* area ratio

of the 780 sample decreases, indicating a majority SrO termination. Meanwhile, samples 740 and 758 change only slightly, suggesting a mixed termination with greater concentrations of surface SrO than either of the single crystal references. Comparisons of Ti 2*p* peak fits for stoichiometric and off-stoichiometric samples (see Figure S8) confirm that there is no difference in Ti valence between samples, indicating that the off-stoichiometry is not attributable to differences in oxygen vacancy concentrations between samples. Previous work has indicated that changes to oxygen stoichiometry produce only 0.001-0.002 Å change in lattice parameter, which is barely detectable even in bulk samples [188] and thus not likely to cause the diffraction peaks we measure.

Given the observed XPS peak area ratio from Figure 5.2(a), it seems likely that the off-stoichiometric samples (798, 837, 856, and 880) are Ti rich and contain Sr vacancies that expand the lattice constant of the film. Conversely, samples with Ti 2*p*:Sr 3*d* area ratios less than those of the single crystal substrates (samples 740, 758, and 780) were found to be stoichiometric as measured by XRD. The similarity of sample 798 to the Nb:STO reference suggests that it is majority TiO_2 terminated. The TiO_2 termination, greater peak area ratio, and greater TTIP flux in comparison to the three stoichiometric samples indicate that the sample is Ti rich. This conclusion can be attributed to some excess Ti floating towards the surface, as has been reported by others for off-stoichiometric STO growth [180,189–191]. The nearly monotonic increase in area ratio suggests that the other three samples are also Ti rich.

This somewhat surprising result suggests that more Sr is present on the film surface relative to the annealed reference substrates. By comparing the peak area ratio to the SrO-terminated STO substrate, we see that the peak area ratios at 45° are very close to that of SrO-terminated STO. As the XPS becomes more surface sensitive the weight of signals coming off the top SrO monolayer is

significantly greater relative to the 45° measurements resulting relatively low area ratio (See Supplemental Information Figure S7). However, the variation in peak area ratios between the more bulk-sensitive 45° and more surface-sensitive 70° measurements indicates that the stoichiometric film surfaces are not fully SrO terminated. Meanwhile, the angle-resolved measurements for the off-stoichiometric samples show that they do exhibit majority TiO_2 terminations.

With the unexpected results from the stoichiometry measurements, an understanding of the surface chemistry gives insight into the film growth process. To understand the surface chemistry of the films, the O 1s peak was further analyzed to determine the surface bonding environment. Figure 5.3 shows the deconvolution of the O1s core level using position constraints of 1.1 eV and 2.3 eV higher binding energy from the bulk oxygen peak for OH and surface oxygen respectively that has been applied elsewhere [192]. The two surface peaks at 1.1 and 2.3 eV have higher binding energies (531.1 eV and 532.3 eV, respectively) than the STO lattice oxygen, and are more pronounced in the70° orientation compared to the 45° configuration due to the greater surface sensitivity provided in angle resolved XPS. Therefore, the 70° XPS measurement better quantifies the adsorbed water, hydroxyl, and undercoordinated oxygen on the surface of the film. A more pronounced 532.3 eV surface peak is observed for samples 740 and 780 (Figure 5.3(a-b)). The absence of the 532.3 eV surface component for films with higher TTIP:Sr flux ratio indicates that these films are primarily Ti- terminated or Ti-rich (Figure 5.3(c-e)). The 532.3 eV surface peak was also observed in the SrO-terminated sample, as shown in Supplemental Figure S6 (Appendix A).

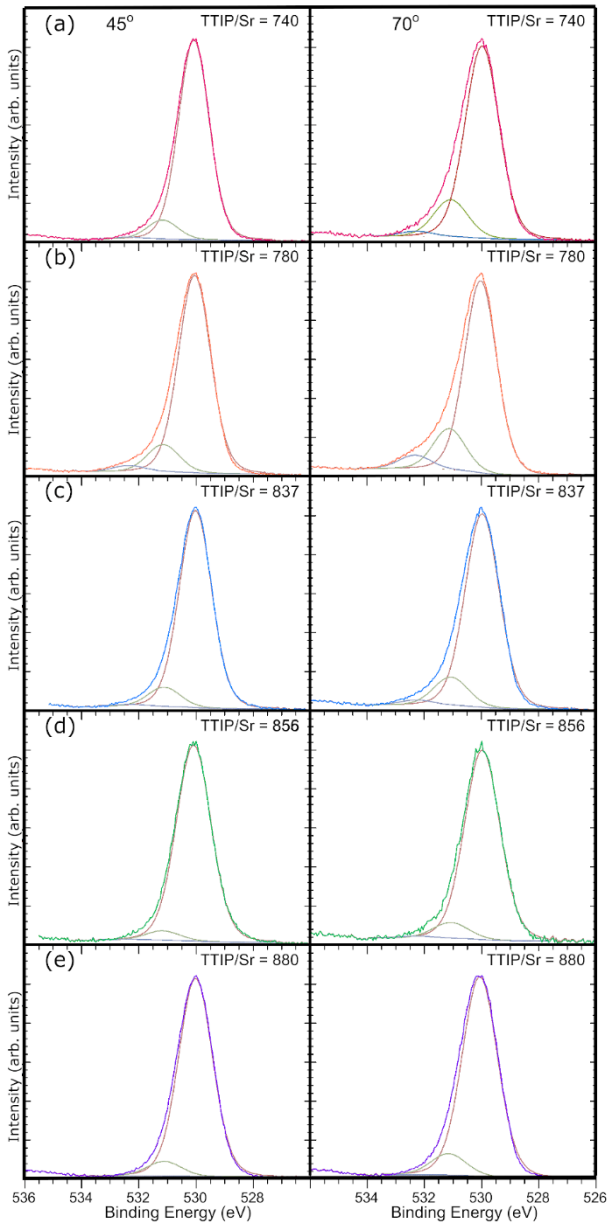

Figure 5.3: O 1s core level deconvolution with electron emission angle 45° and 70° through (a)-(e). Peaks at 530.0 eV, 531.1 eV, and 532.3 eV correspond to lattice oxygen, hydroxyl (OH), and the surface oxygen feature, respectively.

Given that sample 740 has been shown to be stoichiometric and appears to exhibit a partial SrO termination, it was chosen for further analysis of the RHEED videos to understand the growth process. PCA of the RHEED video for Sample 740 is displayed in Figure 5.4 [184]. By studying the time

dependence of the principal components, we can glean the typical information inferred from RHEED oscillations with additional understanding of what components of the surface morphology vary with time. The first two principal components largely contain features that do not appear to correlate with surface evolution during growth. These peaks may originate from a combination of background noise due to cryopump vibrations, diffraction off the bulk of the STO substrate, and the centroid of the zeroth order RHEED streak, which would all be relatively uncorrelated with the film surface evolution. Conversely, oscillations with a frequency that corresponds to a growth rate of 0.45 nm/min are apparent in components 3 through 5. The features of components 3 through 5 are consistent with 2D growth modes observed previously by Vasudevan *et al* [183]. These oscillations damp out around 1100-1300 seconds and the RHEED pattern remains uniform for the remainder of the growth. This transition is consistent with the disappearance of conventional RHEED oscillations reported by Kajdos and Stemmer for stoichiometric films, which was attributed to a transition to step-flow growth [161]. However, similar results could likely be observed for any surface that has reached an equilibrium termination and maintains a uniform surface roughness. Analysis of the RHEED patterns through K-means clustering (see Appendix A, Supplemental Information Figure S2 for more details) further supports this interpretation, as the pattern for Sample 740 transitions from an initial pattern (or "cluster") over the first ~1100 seconds to a final cluster that has minimal time variation for the remainder of the growth. Collectively, these results indicate that the film surface transforms over the first ~1100 seconds (~25 unit cells) from the poorly defined surface present on the air-annealed substrate to an equilibrium surface that is largely unchanged for the remainder of the growth.

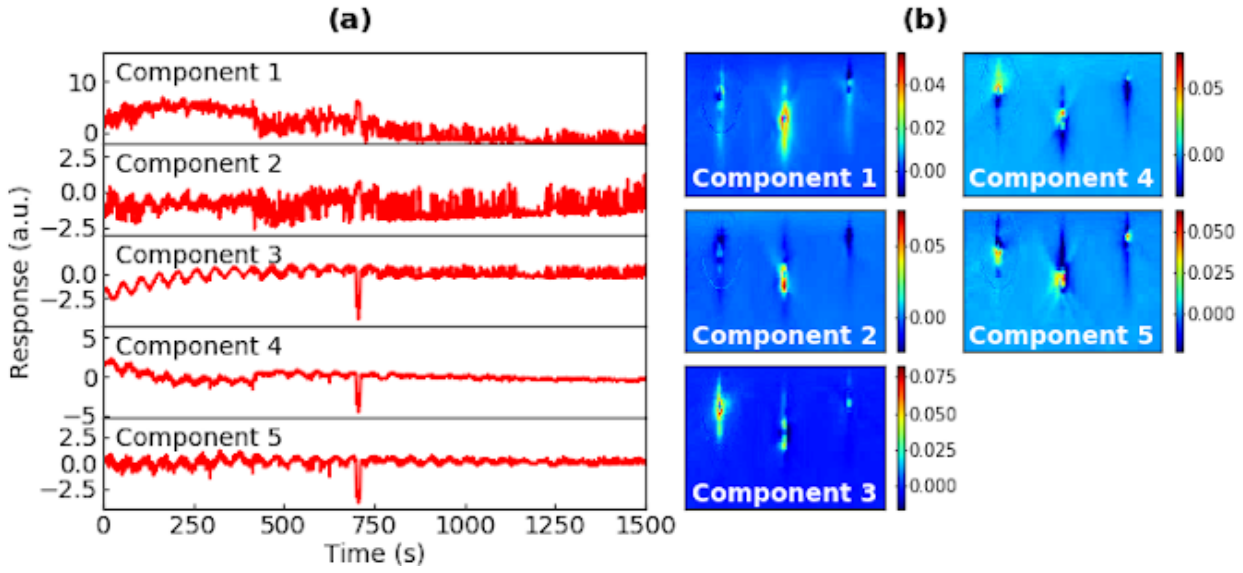

Figure 5.4: Time-dependent eigenvalues (left) and eigenvectors (right) for sample (a) with a constant TTIP/Sr flux ratio of 740.

To summarize the results from the homoepitaxial samples presented thus far, we find that the XRD curves in Figure 5.2 verify that films with greater than expected Sr concentrations at or near the surface are stoichiometric. Meanwhile those that exhibit Ti:Sr peak area ratios comparable to or greater than what is seen in the annealed STO substrates are non-stoichiometric based on XRD measurements and are presumably Ti-rich. The observed 532.3 eV O 1*s* peak for partially SrO terminated films compared to the Ti-rich samples is indicative of undercoordinated oxygen, oxygen vacancies, hydroxyl formation, or other variations in oxygen chemistry at the STO film surface. PCA of the RHEED videos for a stoichiometric film (sample 740) implies uniform growth of the films after ~1100 secs with no changes in surface termination or roughness. This is consistent with the growth of stoichiometric samples reported previously [160,161,164] and indicates that the film surface is in chemical equilibrium with the Sr adatom flux and TTIP and oxygen vapor. Given the relative increase in surface Sr that we observe for stoichiometric Samples 740, 758, and 780, this suggests that the equilibrium surface for STO films grown by hybrid MBE within the growth window

has a partial SrO termination and greater Sr concentrations at the surface than air-annealed single crystal substrates.

To further understand the apparent SrO surface termination of the samples studied thus far, an additional sample was grown with the same nominal stoichiometry and cation ratio (~0.6) from the XPS analysis as sample 740 on Nb-doped STO (see Appendix A, Supplemental Information Figures S3 and S4 for RHEED and XPS data respectively). LEED, LEEM and STM measurements were performed for the STO film grown on Nb:STO to visualize the surface termination, reconstruction and atomic-scale morphology of the film. Figure 5.5 shows LEED and LEEM data for this sample. The LEED image taken with 45 eV electron energy (Figure 5.5(b)) clearly shows the presence of extra diffraction spots between primary spots indicating a surface reconstruction on the film surface. A c(2×2) reconstruction pattern is observed in Figure 5.5(b), as shown by the yellow circles. A separate faint 2×2 reconstruction can also be seen at some energies (not shown) but was not sufficiently intense for isolation in LEEM studies. A bright field LEEM (BF-LEEM) image at 20 eV and dark field LEEM (DF-LEEM) image with c(2×2) at 22 eV (Figure 5.5(c-d)) show that the reconstruction is not uniform across the whole surface. As the c(2×2) spot was intense enough, the DF-LEEM image was reproduced using this spot and BF-LEEM image was reproduced using the specular reflection. These results are consistent with a mixed surface termination, as has been observed BF-LEEM for oxide surfaces prepared by annealing [179,193]. The dark contrast in the BF-LEEM image has been attributed to differences in the surface potential or work function for a SrO termination in comparison to a TiO_2 termination on the surface. The DF-LEEM further confirms that the dark regions in the BF-LEEM image correspond to regions with a c(2×2) surface termination, which is commonly associated with a Sr-rich or Sr-terminated surface [161].

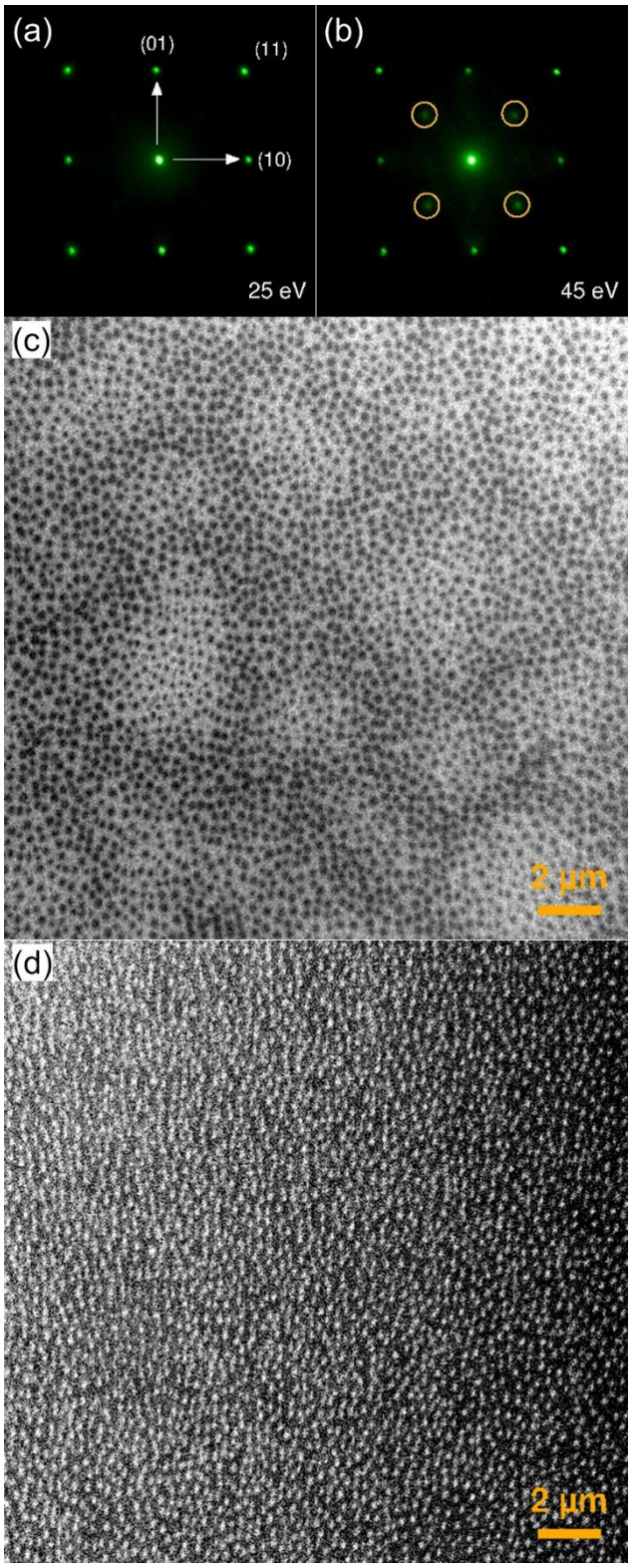
(a)
(01)
(11)
(10)
25 eV
(b)
45 eV
(c)
2 µm
(d)
2 µm

Figure 5.5: Low energy electron diffraction (LEED) at (a) 25 eV and (b) 40 eV electron energies, yellow circles highlight the c(2×2) reconstructions; (c) Bright field low energy electron microscopy (LEEM) image; and (d) Dark field LEEM image highlighting the regions of c(2×2) reconstructions.

To examine the island structures observed through LEED and LEEM measurements, the sample was also analyzed through STM imaging experiments. Figure 5.6 shows a characteristic wedding-cake type structure observed across the entire sample with terrace widths of 40 to 70 nm on stacks with well-defined steps. Atomic force microscopy measurements on the homoepitaxial series of samples show qualitative agreement with the morphology observed in this sample (see Supplemental Information Figure S9). A wedding cake structure is formed when the Ehrlich-Schwöbel (ES) barrier, which limits diffusion across the step edge, cannot be overcome. The adsorbates which ultimately form the growing oxide, are trapped on the top layer and reflected from the step edge. The adsorbate diffusion length on the surface is correlated to the width of the rim – the distance between the terrace step edges [194]. Ultimately, once the adsorbate concentration is sufficiently high, a new layer will nucleate, albeit with a diminished radius which leads to the stacked, wedding cake like structure. The apparent height of the step edges is about ~4 Å which corresponds to a unit cell step height of STO with lattice constant 3.905 Å. In contrast to the strong step-edge anisotropy often observed in metal-on-metal epitaxy with a significant ES barrier [195], the oxide islands do not exhibit a pronounced edge faceting or anisotropy. STM studies of (La,Ca)MnO_3 perovskite oxide films have also demonstrated the wedding cake structure due to the ES barrier in these materials [196–198]. These studies examined transitions between mixed terminations and uniform *B*-site termination as a function of film thickness and noted the presence of a c(2×2) reconstruction for the *A*-site terminated regions, as we also observe in the LEED/LEEM studies. Given our results, it seems apparent that the homoepitaxial growth mode for hybrid-grown STO films within the stoichiometric growth window is not exclusively layer-by-layer or step-flow.

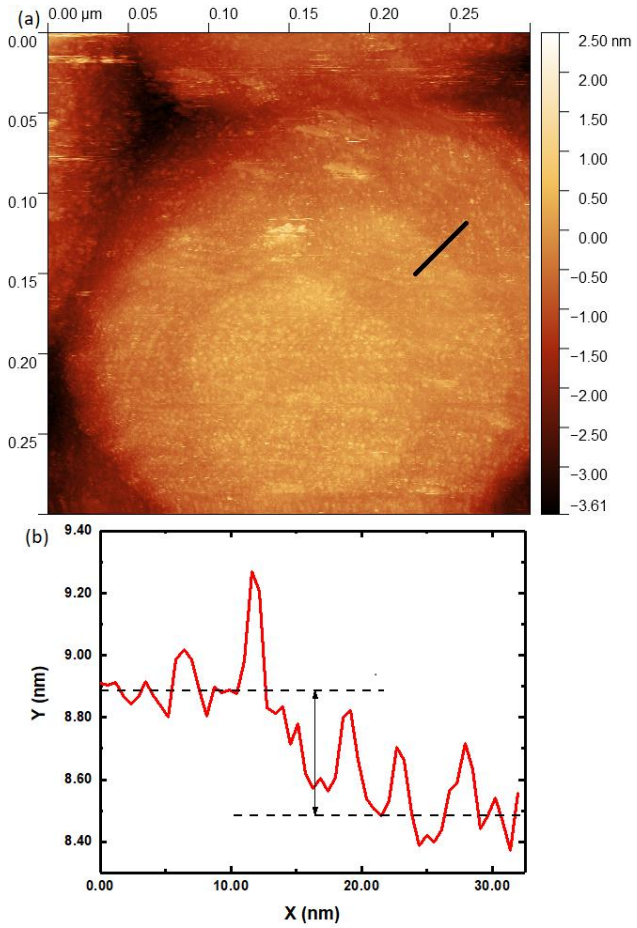

Figure 5.6: (a) Scanning tunneling microscopy (STM) image with (b) line profile shown from black line in (a). Dashed lines represent a 4.0 Å step consistent with the 3.905 Å $SrTiO_3$ unit cell height. Image size 300×300 nm^2.

The surface studies that we report here raise questions as to the nature of the chemical interaction during the hMBE growth process. We have shown that samples with partial SrO termination (samples 740, 758, and 780) are stoichiometric in XRD. Conversely, the XRD results demonstrate samples with surface compositions analogous to that of an air-annealed substrate are off-stoichiometric. Based on angle-resolved XPS measurements, these off-stoichiometric samples showed a preference for majority TiO_2 surface terminations. Surface reconstructions are observed for stoichiometric samples, although we have not observed the c(4×4) reconstruction that others have reported [161]. Instead, a surface with partial SrO termination and evidence of a c(2×2) surface reconstruction in some cases

aligns with the ideal stoichiometry as measured by XRD. These *in situ* observations are confirmed by the LEEM, LEED, and STM measurements. While a surface reconstruction could not be resolved by STM due to atmospheric exposure, the rounded nature of the wedding cake terraces suggests that the terraces are the source of the c(2×2) reconstruction observed in the LEEM images of Figure 5.5(c-d). Thus, it is likely that the wedding cake terraces have a majority SrO termination, which gives rise to the significant ES barrier.

Our results suggest that in order to stabilize the adsorption-controlled growth regime, a significant portion of the surface must possess an SrO termination to catalyze the decomposition of TTIP in stoichiometric ratios. Brahlek *et al* [159] have previously hypothesized that the TTIP sticking coefficient is greater on an SrO termination than on a TiO_2 termination, which agrees with the results we show here. Recent theoretical studies have predicted a stable c(4×4) SrO-terminated STO surface with only half of the surface A sites occupied, which would qualitatively agree with our results and merits further investigation [199]. The existence of the extra XPS peak in the O 1*s* spectrum is associated with undercoordinated oxygen, oxygen vacancies, adsorbed water, or bonded OH on the surface for SrO terminations, which is not observed for TiO_2 terminated films. The presence of adsorbed water or oxygen vacancies will depend significantly on the surface termination and the ambient environment [176,177]. Given that water is a natural byproduct of the TTIP dissociation, the role of water vapor near the film surface may play a role in the chemistry of the adsorption-controlled growth. In the future, *in situ* STM, LEEM, and LEED studies of hMBE grown STO films would be extremely valuable to understand the surface structure in greater detail. However, to our knowledge, there is not currently a growth system conFigured for such studies. Further development of *in situ* surface characterization capabilities to complement hMBE growth would be extremely valuable.

5.4 Conclusion:

In conclusion, we have demonstrated hMBE synthesis of homoepitaxial STO films with *in vacuo* XPS studies for the first time. We show that carbon contamination on the surface is negligible. We find that films exhibiting a partial SrO termination are needed to produce a stoichiometric film as measured in XRD, while TiO_2 terminated films are Ti rich. These results are confirmed via XPS through core level Ti 2*p* to Sr 3*d* peak area ratios and the observation of O 1s surface peaks. Analysis of the RHEED pattern through PCA and K-means clustering indicate that the stoichiometric films transition to a step-flow growth regime after 20-25 unit cells. RHEED, LEEM, LEED, and STM studies verify that surface reconstructions are associated with ideal film stoichiometry, though other complementary surface studies are needed to better probe the reconstructions and surface terminations.

Acknowledgments:

We acknowledge Z. Dai for technical assistance. ST and RBC gratefully acknowledge support from the Air Force Office of Scientific Research under award number FA9550-20-1-0034. ST, SRP, and WJ also acknowledge support from the Auburn University Department of Physics. JML and MB acknowledge support from by the U.S. Department of Energy (DOE), Office of Science, Basic Energy Sciences, Materials Sciences and Engineering Division. This research used resources of the Center for Functional Nanomaterials and National Synchrotron Light Source II, which are U.S. DOE Office of Science Facilities, at Brookhaven National Laboratory under Contract No. DE-SC0012704. DJ and PR acknowlegde the support by support from the National Science Foundation (NSF) (Award No. DMR-2004326) by the Division of Materials Research – Metals and Metallic Nanostructures.

Chapter 6

Surface Stability of $SrNbO_{3+\delta}$ Grown by Hybrid Molecular Beam Epitaxy

Suresh Thapa[1], Sydney Provence[1], Steve M. Heald[2], Marcelo A. Kuroda[1], and Ryan B. Comes[1]

[1]Department of Physics, Auburn University, Auburn, AL 36830, USA

[2]Advanced Photon Source, Argonne National Laboratory, Argonne, IL 60439, USA

Submitted for Publication, available online via ArXiv:2110.15341 [Cond-Mat] (2021)

Abstract:

4d transition metal oxides have emerged as promising materials for numerous applications including high mobility electronics. $SrNbO_3$ is one such candidate material, serving as a good donor material in interfacial oxide systems and exhibiting high electron mobility in ultrathin films. However, its synthesis is challenging due to the metastable nature of the d^1 Nb^{4+} cation and the limitations in the delivery of refractory Nb. To date, films have been grown primarily by pulsed laser deposition (PLD), but development of a means to grow and stabilize the material via molecular beam epitaxy (MBE) would enable studies of interfacial phenomena and multilayer structures that may be challenging by PLD. To that end, $SrNbO_3$ thin films were grown using hybrid MBE for the first time using a tris(diethalamido)(tert-butylimido) niobium precursor for Nb and an elemental Sr source on $GdScO_3$ substrates. Varying thicknesses of insulating $SrHfO_3$ capping layers were deposited using a hafnium tert-butoxide precursor for Hf on top of $SrNbO_3$ films to preserve the metastable surface. Grown films were transferred *in vacuo* for X-ray photoelectron spectroscopy to quantify elemental composition, density of states at the Fermi energy, and Nb oxidation state. *Ex situ* studies by X-ray absorption near

edge spectra illustrates the $SrHfO_3$ capping plays an important role in preserving the Nb $4d^1$ metastable charge state in atmospheric conditions.

6.1 Introduction:

The observation of two dimensional electron gas (2DEG) at the $LaAlO_3$ (LAO)/$SrTiO_3$ (STO) interface [200] has driven ongoing and expanding research in complex metal oxides for the past two decades. This interesting phenomenon placed the oxide interfaces as strong contenders for high carrier concentrations and high electron mobility. (Alternative to the first two sentences)

For two decades, the study of two dimensional electron gas (2DEG) in complex metal oxides has rapidly increased after its observation at the $LaAlO_3$ (LAO)/$SrTiO_3$ (STO) interface [200]. This interesting phenomenon has driven ongoing research for two decades, opening the door for complex oxide interfaces as strong contenders for high carrier concentrations and high electron mobility. Oxide 2DEG [36,37] offer unique opportunities compared to traditional semiconductor ones as they may exhibit strong spin-orbit coupling along with possibility of harnessing high carrier concentrations. The search for a good donor oxide is a great challenge when building a high carrier concentration and mobility in oxides interface for high-speed electronics. Isoelectronic to the $SrVO_3$, $SrNbO_3$ (SNO) has a d^1 electronic configuration and a simple cubic perovskite structure with lattice parameter between 4.0 and 4.1 Å [201]. The band diagram of SNO reveals the Nb 4d t_{2g} bands crossing the Fermi level, indicating its metallic nature, whereas the low work function makes SNO stand out as a suitable donor [202], as previously reported in density functional theory (DFT) studies on SNO/STO heterostructures [203]. SNO has also been discovered as the first plasmonic photocatalyst metallic oxide, which opens a door for new family of photocatalytic materials [204]. Studies have also examined the material for use as a plasmonic transparent conducting material due to the large band

gap between the O 2*p* and Nb 4*d* bands [205–207]. Recent results have also shown that epitaxial strain in SNO films can break cubic symmetry to produce a semimetallic tetragonal phase with extremely high mobility and an observed Berry phase that make it promising for quantum materials applications [208]. Large linear magnetoresistances of ~10^5 % and mobilities of 80,000 cm^2/V-s have also recently been reported in SNO/STO heterostructures [209], suggesting that the material holds exceptional promise in topological and quantum materials research.

Despite the great potential of SNO for interfacial charge transfer and topological phenomena as well as its photocatalytic properties, limited work has been carried out in synthesis of pristine SNO thin films. There are numerous unanswered questions on basic properties of SNO, its surface stability, and its applications for interfacial engineering of emergent materials properties. Previous reports on SNO thin film growth have employed pulsed laser deposition (PLD) [207–212] and sputtering [205,206]. There are no reports of MBE synthesis of SNO, though NbO_2 [213] and Nb-doped STO [214] have been synthesized by MBE using an electron-beam evaporation source. In particular, previous work [211] examining the electronic band structure using *in situ* angle-resolved photoemission spectroscopy (ARPES) measurements provided insights into SNO thin films and verified the metallic character of SNO experimentally. However, this work also showed a significant excess of Nb^{5+} atomic valence relative to the expected 4+ charge state, which suppressed the spectral weight of electronic states near the Fermi level. These results were attributed to surface Nb^{5+} states due to either Sr vacancies or formation of Nb_2O_5. However, adsorption of excess oxygen is also an alternative mechanism to accommodate the conversion from metastable Nb^{4+} to the stable d^0 Nb^{5+} state through the formation of a $Sr_2Nb_2O_7$ phase [212,215,216]. Similar results have also been observed in d^1 rare earth titanates [217,218] and $SrVO_3$ [213] previously. Clearly, understanding and controlling the valence of Nb ions in SNO films is important to the development of interfacial heterostructures that

leverage the d^1 electronic configuration and propensity of SNO to donate electrons to neighboring materials [208,209].

One of the most likely approaches to preserve metastable SNO is by capping films with an alternative oxide with greater atmospheric stability. To date, there have been no reports of suitable capping layers for SNO. However, such an approach has been employed for $DyTiO_3$ films via a $LaAlO_3$ cap, which significantly enhanced the ratio of metastable Ti^{3+} vs d^0 Ti^{4+} [218]. A perovskite oxide with a higher band gap, matching A site cation, and one that does not accept electrons from SNO would be a reasonable choice as a capping layer. $SrHfO_3$ (SHO) is well known for its large band gap of 6.07 eV [219] and is expected to have a band alignment that prevents electron transfer, [202] which makes it an ideal perovskite oxide for capping in this system. However, the delivery of both Nb and Hf is highly challenging due to their refractory natures. To overcome this discrepancy, the hybrid molecular beam epitaxy technique opens opportunities for Nb and Hf to be supplied as metal organic precursors.

In addition to PLD, molecular beam epitaxy (MBE) is well established for the synthesis of various metal oxides over the last three decades. However, repeatable growth of a complex metal oxide incorporating refractory metal cations with stoichiometric control by traditional MBE is extra challenging as they lack the adsorption-controlled growth window. In the past decade, hybrid MBE (hMBE) has been established as a state-of-the-art technique to grow complex metal oxides where refractory metals are supplied through a metal organic precursor and the A-site cation is supplied as a metallic source [220]. The hMBE technique is highly efficient in delivering low vapor pressure and refractory metals for repeatable growth of large varieties of high quality metal oxides such as $SrVO_3$ [221] , $BaSnO_3$ [222] , and $SrTiO_3$ (STO) [68,223] with improved stoichiometric control compared to the traditional MBE growth. This approach offers significant advantages over deposition

with an electron-beam evaporator in an MBE, where achieving repeatable and stable growth conditions can be a challenge.

Selection of precursor becomes highly important in perovskite oxides growth involving refractory metals as they determine the delivery of B-site cation. Previous reports [224,225] on synthesis of Nb_2O_5 by atomic layer deposition (ALD) suggest that niobium ethoxide (NbOEt) and tris(diethalamido)(tert-butylimido) niobium (TDTBN) are the most suitable precursors as a Nb precursor. However, NbOEt decomposition rather than evaporation in its molecular form has been reported due to significantly lower vapor pressure of NbOEt compared to TDTBN [225]. TDTBN was liquid at room temperature and successfully evaporated for ALD at 65 ℃ using open boats due to the low vapor pressure of the precursor. Recent work has shown both thermal and plasma-enhanced ALD of Nb_2O_5 using TDTBN [226]. In the case of thermal ALD, significant amounts of Nb^{4+} ions were observed in the films grown at high temperatures, likely because, unlike NbOEt, TDTBN contains no oxygen atoms in the molecule. The chemical structure of the molecule is shown in Figure 6.1. The lack of oxygen in the TDTBN precursor may afford greater control over the overall oxidation of the film because the delivery of molecular O_2 and oxygen plasma can be tuned to vary the oxygen chemical potential in the system over a wide range.

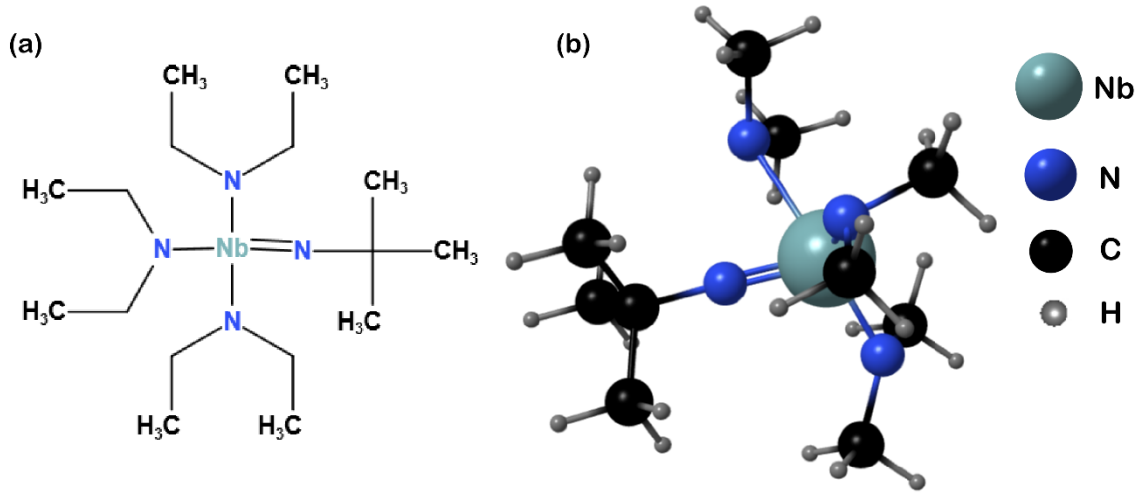

Figure 6.1: (a) Structural formula and (b) ball and stick structure of tris(diethalamido)(tert-butylimido) niobium (TDTBN) precursor used for the hMBE growth of SNO epitaxial thin films.

In this work, SNO band structure and partial density of states (pDOS) calculations are carried out by density functional theory (DFT). Metastable SNO films are grown on $GdScO_3$ substrate using hMBE. The surface of the film is monitored during the growth by reflection high energy electron diffraction (RHEED) and *in vacuo* X-ray photoelectron spectroscopy (XPS) is used to check the stoichiometry of the film. Possible over-oxidation of the surface or of the film is studied by analyzing the Nb 3*d* core level on uncapped and SHO capped samples. Correlating the valence band features further investigates the effectiveness of SHO capping in preserving Nb^{4+} state. The surface roughness is analyzed using atomic force microscopy (AFM) topography. Further Nb K- edge was analyzed using X-ray near-edge spectroscopy (XANES) to check the effect of SHO capping thickness on Nb oxidation state.

6.2 Methods:

The electronic band structure of SNO was analyzed via DFT, using the Perdew-Burke-Ernzerhof (PBE) parameterization of the exchange-correlation energy [227]. No Hubbard U correction parameter was employed, consistent with previous models of the material [208,211]. Calculations employed projector-augmented-wave pseudopotentials [228] for the description of the atomic cores with cutoff energies of 40 Ry and 400 Ry for the wave functions and density, respectively. Cubic unit cells were fully relaxed until forces were smaller than 1.36×10^{-7} eV/Å and band structure calculations were performed. The self-consistent potential was determined using an 8×8×8 Monkhorst-Pack mesh to sample the Brillouin zone. All calculations are carried out using the Quantum Espresso software [229].

Uncapped and SHO capped SNO thin films of identical thickness were grown on highly lattice matched (110) $GdScO_3$ (GSO) single crystal substrates (MTI Crystal) in a Mantis MBE reactor with a baseline pressure of $\sim10^{-9}$ Torr. All the substrates were ultrasonically cleaned in acetone and isopropanol and dried with dry nitrogen gas. All the substrates were cleaned in oxygen in the MBE growth chamber by ramping to the 1000 °C growth temperature over ~1 hour as measured by thermocouple [135,223]. We estimate that the setpoint was ~150-200 °C higher than substrate surface temperature due to the absence of backside substrate metallization, resulting in GSO surface temperature between 800 and 850 °C. Cleaning and SNO (SHO) growths were performed in a background pressure of $\sim3\times10^{-6}$ Torr and $\sim3.6\times10^{-6}$ ($\sim1\times10^{-5}$) Torr O_2 respectively. Calibration samples showed that the absorption of B-site cations takes a longer time compared to low flux of A-site cation. To control the exposure duration, alternate shutter deposition is applied to supply A and B-site cations in both SNO and SHO deposition. For the metalorganic sources, a pneumatic ALD

valve (Swagelok 316L) is used to isolate the sources when they are not depositing and serves as the shutter for the deposition.

A series of uncapped and varying SHO thickness capped SNO samples were grown where Sr and tris(diethalamido)(tert-butylimido) niobium (TDTBN) fluxes were held fixed. The flux of SrO is measured by quartz crystal microbalance (QCM) in Å/sec. Strontium (99.99%, Sigma-Aldrich, USA) was supplied through low temperature effusion cell. The Sr flux was calibrated using QCM under oxygen environment with measured chamber pressure of 3×10^{-6} Torr. Niobium was supplied through a gas source using the TDTBN metal-organic precursor (99.99%, Sigma-Aldrich, USA) from a bubbler connected to the growth chamber using the ALD pneumatic valve and a heated gas injector source (E-Science, USA). No carrier gas was used. The gas injector was held at 90 °C using a PID controller and the bubbler at 73 °C through external heating tape and a PID controller. While the vapor pressure was not measured directly, the chamber pressure showed only marginal changes (~1%) upon valve actuation, suggesting that the vapor pressure is in the range of 1-100 mTorr that is commonly employed for hMBE using a pressure-control feedback system [220]. This configuration can thus be thought of as a modified metal-organic evaporation source that replicates the capabilities of a low temperature effusion cell for organic molecules.

The growth chamber shroud walls were maintained at -30 °C via a closed loop chiller and low temperature fluid (Syltherm XLT, Dow Chemical) to reduce the background water vapor pressure from the dissociated TDTBN molecules. The chamber pressure measured by cold cathode gauge generally increases and reaches one unit higher at 10^{-6} Torr for the first 5-10 secs as the TDTBN supply valve is opened before stabilizing due to the dissociated and unreacted TDTBN injected into the system. O_2 flow is turned off for uncapped sample during cool down to minimize over-oxidation

of the film or of the surface of the film. Right after the SNO deposition, the hafnium tert-butoxide (HTB) flux is calibrated and varying thickness of SHO capping layers were deposited turning on O_2 flow with measured chamber pressure of ~1×10^{-5} Torr O_2. Hafnium was supplied through a gas source using a metalorganic precursor, HTB (99.999%, Sigma-Aldrich, USA) from a bubbler connected to the growth chamber without carrier gas and controlled using a traditional pressure-control feedback loop [220,230]. Here we have presented four representative samples among all the samples including one uncapped and three capped annotated as thin (2 unit cells, ~0.8 nm), medium (3 unit cells, ~1.2 nm), and thick (4 unit cells, ~1.6 nm) capped.

In situ RHEED (Staib Instrument) was used to monitor the growth process and the quality of the film. Post-growth the samples were transferred from the MBE reactor to the PHI 5400 X-ray photoelectron spectroscopy (XPS) (Al Kα X-ray source) system through ultra-high vacuum (UHV) transfer line. An electron neutralizer gun was applied to compensate charging of the insulating samples [180]. The surface stoichiometry of all grown samples was characterized by analyzing core level and correlated with the valence band XPS spectra measured with base pressure of ~1×10^{-9} Torr. Analysis of the XPS data was performed using CasaXPS. To properly align all core level peaks, the valence band is fitted with a Fermi-Dirac function and all peaks are shifted with respect to the Fermi level because the charge neutralizer prevents direct determination of the Fermi level. A representative fit is shown in Figure S4 in the Supplemental Information (Appendix B). We assume in our analysis that electron forward focusing effects, commonly referred to as X-ray photoelectron diffraction, are negligible between samples. Though the probing depth for 95% of the signal is less than 5 nm which indicates these measurements are highly surface sensitive. A Rigaku Smartlab XRD equipped with a 4-circle goniometer and using Cu $K\alpha_1$ radiation line isolated with double bounce Ge (220) monochromator was used for 2θ-ω scans on the (002) reflection of the SNO samples. X-ray absorption near-edge

spectroscopy (XANES) was performed at the Advanced Photon Source at Sector 20-BM in fluorescence mode for both in-plane (parallel) and out-of-plane (perpendicular) polarized x-rays at the Nb K edges.

6.3 Results:

Figure 6.2(a) shows the cubic crystal structure of perovskite SNO where a niobium cation is octahedrally coordinated by oxygen ions. A lattice parameter of 4.02 Å was obtained using DFT calculations, which is agreement/disagreement with previous work [201]. The band structure and corresponding density of states (DOS) that provide context to interpret experimental results of SNO are shown in Figure 6.2(b) and 6.2(b) right panel, respectively. The metallic nature of SNO is observed with the Fermi level crossing conduction bands primarily formed by Nb 4d states, consistent with its d^1 electronic configuration. The O 2*p* bands make significant contributions to the band structure of SNO in the vicinity of the Fermi level. Fully occupied valence bands are composed mainly by the O 2*p*. The gap between the O 2p and Nb 4*d* bands is ~2.4 eV. These results agree with previous DFT reports [211].

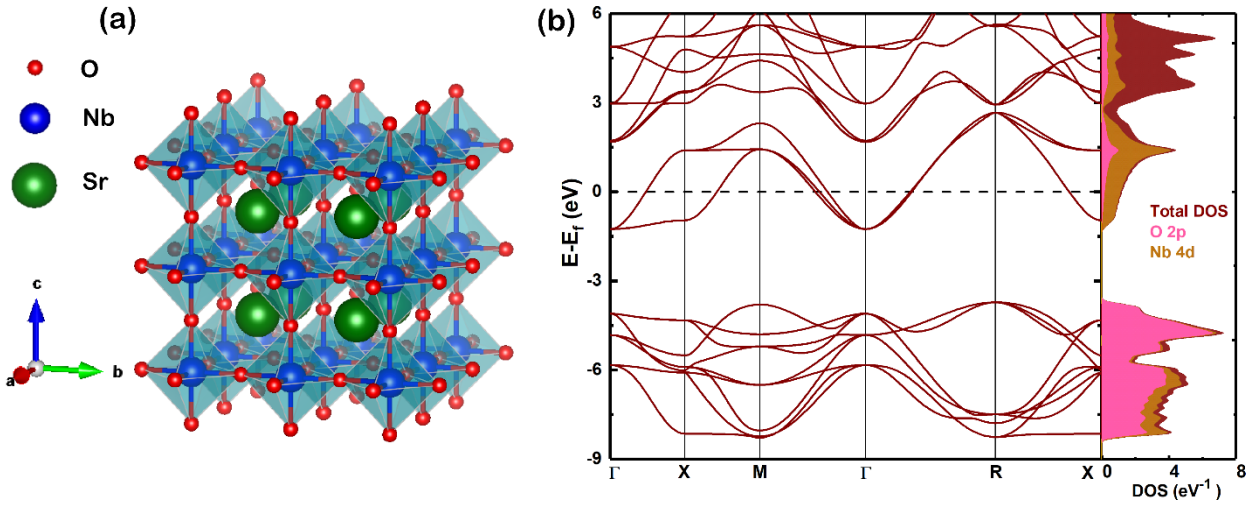

Figure 6.2: (a) Cubic perovskite structure of $SrNbO_3$, (b) band dispersion and density of states (DOS) of $SrNbO_3$. Orbital decomposition onto localized atomic orbitals from Nb 4d and O 2*p* are shown in gold and pink, respectively.

To test the efficacy of TDTBN as a precursor, SNO thin films were grown on GSO substrates by hMBE. Figure 6.3(a-b) shows the RHEED images for uncapped SNO film grown on GSO along the [110] azimuth immediately after growth at high temperature and after the sample is cooled down to room temperature. Intense diffraction spots as well as sharp Kikuchi bands in Figure 6.3(a) indicate that the sample is smooth with a well-crystalized surface film. However, the diffraction spots along with Kikuchi bands lose their intensity after the sample is cooled as shown in Figure 6.3(b), indicating degradation in surface crystal quality. One possible explanation for this phenomenon is the over-oxidation of the film surface due to the presence of residual oxygen and water in the chamber, which cannot be pumped out quickly enough after the growth. Water is also a likely by product of the decomposition of the precursor. A second possible reason may be due to adsorbed nitrogen and carbon on the film surface as a by-product from metal organics as shown in XPS spectra for uncapped sample in, Supplemental Information S3 (Appendix B). On the other hand, SNO samples show consistently improved RHEED images after capping with SHO, which can be found in supporting materials in

Figure S1 (Appendix B). This indicates high crystallinity of the SHO capping layer and better preservation of SNO from over-oxidation during cooldown. It should be noted that the medium-capped SNO sample shows relatively weak RHEED pattern after SHO capping as found in Figure S1 because of inconsistent Hf flux that produced a Hf-rich capping layer (Appendix B).

AFM measurements were performed to verify the surface morphology of the SNO films. Figure 6.3(c) shows the AFM topography of uncapped SNO film grown on GSO substrate with surface roughness of ~ 1.1 nm indicating the film is highly smooth. Additionally, AFM topography of SHO shows the surface roughness of ~2 nm as shown in Figure S2 indicating smooth capping surface (Appendix B). Figure 6.3(d) shows the XRD data for uncapped and SHO capped SNO films grown on GSO substrates. An uncapped SNO sample exhibits no clear evidence of crystalline perovskite film while capped samples have extra peak at lower 2θ. The intensity of an extra peak increases with increasing thickness of a capping, reflecting improved stoichiometry and crystallinity as predicted by the RHEED.

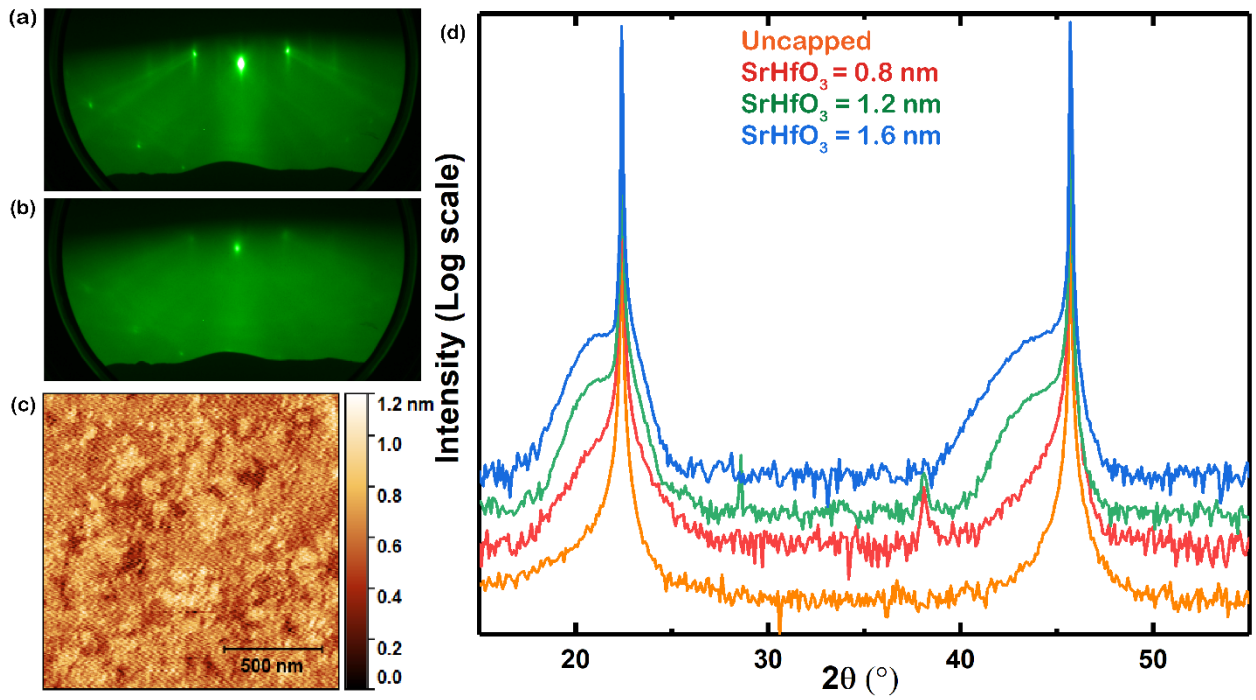

Figure 6.3: RHEED image of SNO film (a) hot right after growth and (b) after cooling down on GSO along 110 azimuth, (c) AFM topography of uncapped SNO films, (d) XRD on uncapped and SHO capped samples.

To probe the role of capping on preservation of the Nb^{4+} state, *in situ* XPS analysis of the Nb 3*d* core level on uncapped and SHO capped SNO films was performed. Figure 6.3(a-d) show the Nb 3*d* core level deconvolution for uncapped and SHO capped SNO films using constraints from table S1 as provided in supplemental information. As the Hf 4d core level significantly overlaps with the Nb 3*d* core level, the peaks must be carefully deconvoluted to determine the ratio of Nb^{4+} to Nb^{5+}. A clear extra peak at lower binding energy in Nb 3*d* is significantly increased in capped samples compared to an uncapped sample that reflects the SHO capping is highly effective in preserving the Nb^{4+} state. This peak has previously been observed after sputter cleaning of NbO_2 after atmospheric exposure [231] and *in situ* for high-quality NbO_2 films grown by MBE using an electron-beam evaporation source [213]. *In situ* measurements of uncapped $SrNbO_3$ films grown by PLD showed significantly smaller concentrations of Nb^{4+} by comparison [211], indicating that the $SrHfO_3$ capping

layer is important even for *in situ* studies of the material. Explicit quantification of the ratio of Nb^{4+} to Nb^{5+} is complicated by the satellite feature that is expected even for an ideal system with only d^1 states for all Nb cations [213]. However, it is clear that some Nb^{5+} is still present even in the capped samples, leading to a chemical formula of $SrNbO_{3+\delta}$ for the material.

XPS valence band spectra were acquired simultaneously with the Nb 3*d* core level data to measure the density of states for the Nb 4d electronic states near the Fermi level. Figure 6.4(e) shows the valence band spectra for uncapped and SHO capped samples. The thickness and quality of the capping layer plays a clear role in the preservation of the single Nb 4d electron at the Fermi level, with the thickest capping layer providing the largest peak. The medium-capped sample shows relatively lower electron concentration compared to a thin capped sample as shown in Figure 6.4(e). That is likely related to the off-stoichiometry of the SHO capping layer governed by fluctuation in Hf flux during SHO deposition for that sample. This can be inferred from Figure 6.3(b) as we see a more intense Hf 4d core level compared to Nb 3*d* core level among all capped samples. This result can also be correlated with lowest quality of RHEED image for medium capped film as shown in middle panel of Figure S1 (Appendix B). It is thus clear that the effectiveness of SHO as a capping layer for SNO is dependent on the crystalline quality of the SHO film.

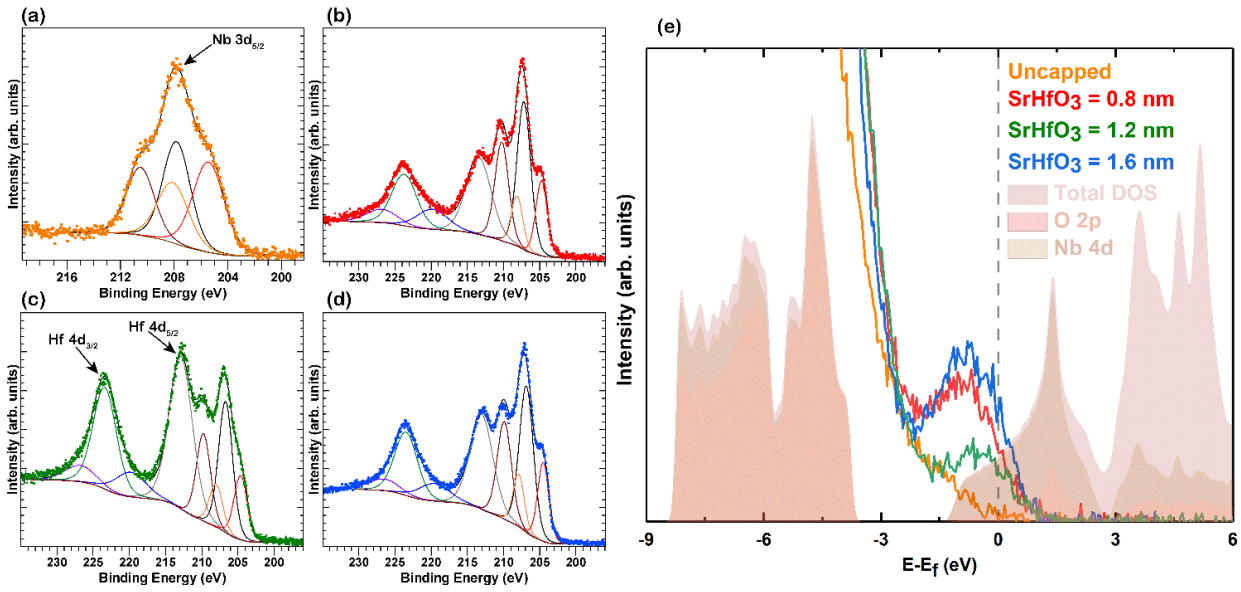

Figure 6.4: Nb 3*d* core level deconvolution for SNO thin films capped with (a) uncapped, (b) thin (0.8 nm) capped, (c) medium (1.2 nm) capped, (d) thick (1.6 nm) capping of SHO. Fits to the data show spin-orbit split peaks of Nb^{4+} (low binding energy) and Nb^{5+} (high binding energy) features. (e) Valence band XPS data showing density of states near the Fermi level for all four samples. Partially transparent density of states from DFT model of $SrNbO_3$ is taken from Figure 6.2.

XANES offers a more bulk-sensitive probe of the Nb valence after atmospheric exposure. Hence, to supplement the XPS analysis on oxidation state of Nb in the film, XANES analysis on Nb K-edge was also carried out. Figure 6.5 shows the XANES spectra on the Nb K-edge for SHO-capped samples with reference spectra for Nb^{4+} (NbO_2) and Nb^{5+} (Nb_2O_5) [232]. The Nb K-edge shows that the pre-edge features of the thinnest capped SNO sample mirrors Nb_2O_5 spectra, indicating more Nb^{5+} state compared to other samples. The white line is also shifted to greater photon energy, consistent with a higher formal charge. The Nb K-edge energy in the inset of the Figure shows that the thickest capped sample the spectrum white line is shifted to lower photon energy, indicating the greatest concentration of Nb^{4+} state among all of the samples. This observation indicates that the capping has great role on preserving Nb oxidation state in SNO film after air exposure.

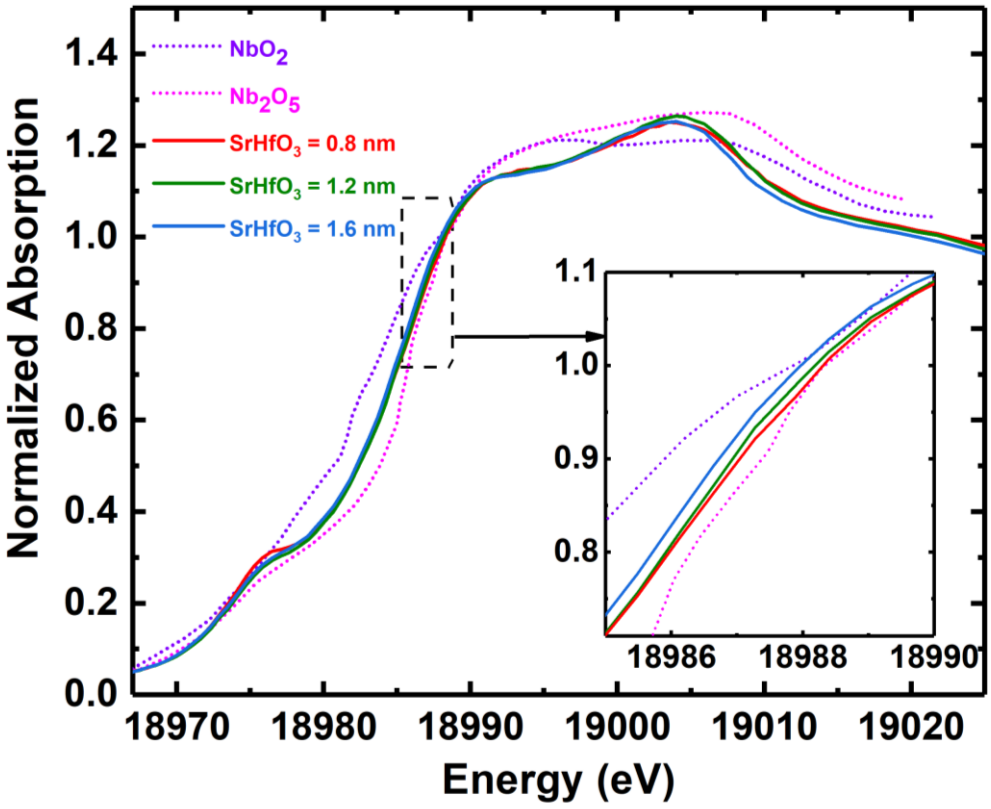

Figure 6.5: Nb K edge XANES data for three $SrHfO_3$-capped samples. NbO_2 (Nb^{4+}) and Nb_2O_5 (Nb^{5+}) reference spectra were taken from Marini, et al. *[232]*. (Inset) High-resolution perspective of three capped samples showing enhanced Nb^{4+} charge state in sample with 1.6 nm capping layer.

6.4 Discussion and Conclusion:

Successful growth of metastable SNO by hMBE using the TDTBN precursor is performed for the first time. Good lattice match to the GSO substrate supported the growth of high quality epitaxial SNO films, which can be inferred from the high quality RHEED in Figure 6.2(a) and Figure S1. Degrading RHEED quality of an uncapped sample during cool down shows that residual oxygen in the chamber over-oxidizes the SNO film surface. Our observation shows that minimizing exposure to oxygen after film growth is critical to preserving a stable film surface, as shown in the RHEED images in the supplemental information and the valence band density of states in Figure 6.4. Over-

oxidation of the SNO film surface can be reduced by depositing a dielectric caping layer such as SHO. Cooling down in vacuum for uncapped samples reduces the formation of competing phases such as amorphous $Sr_2Nb_2O_7$ [212]. However, surface-sensitive studies such as XPS and ARPES are still likely to detect the majority of the signal from the top few unit cells where Nb^{5+} will be the dominant charge state. On the other hand, ex-situ AFM topography reveals that uncapped samples are highly smooth even after air exposure, suggesting that amorphization is fairly uniform across the sample. Thus, a smooth surface is not sufficient evidence to confirm ideal oxygen stoichiometry at the film surface. Our XRD results show that thin SNO films (less than 5 nm) had degraded crystal quality without a capping layer. Thus, we suggest that future studies on ultrathin SNO films should take care to decouple intrinsic phenomena related to the novel physics that can occur in the system from features that may occur due to variation in oxygen stoichiometry away from the ideal $SrNbO_3$ chemical formula.

In conclusion, our study of the synthesis of metastable $SrNbO_{3+\delta}$ thin films demonstrates the capabilities of the hMBE technique with a new TDTBN precursor. As predicted by our DFT calculations, the SNO films have valence band features at the Fermi level based on XPS analysis which is strongly dependent on the Nb charge state. The surface of the sample is preserved during cooldown by depositing a capping layer of $SrHfO_3$ immediately after $SrNbO_3$ growth, which increases the electronic density of states near the Fermi level. XRD, XAS and XPS used to characterize the SNO film and effectiveness of the SHO capping at various thicknesses indicate that both the quality and the thickness of the capping layer are important to preserving the surface. The ability to deposit $SrNbO_3$ films by hMBE opens the door for future exploration of interfacial phenomena in heterostructures, which has not been explored previously in films.

Acknowledgements:

ST and RBC gratefully acknowledge support from the Air Force Office of Scientific Research under award number FA9550-20-1-0034. This research used resources of the Advanced Photon Source, an Office of Science User Facility operated for the U.S. Department of Energy (DOE) Office of Science by Argonne National Laboratory, and was supported by the U.S. DOE under Contract No. DE-AC02-06CH11357.

Chapter 7

Charge Transfer at SNO/BSO Interface

7.1 Introduction:

The observation of a two-dimensional electron gas (2DEGs) at the $LaAlO_3$ (LAO)/$SrTiO_3$ (STO) interface [21] has driven ongoing and expanding research in complex metal oxides for the past two decades. This interesting phenomenon suggested that oxide interfaces can be strong contenders for high carrier concentrations and high electron mobility. Oxide 2DEGs offer unique opportunities compared to traditional semiconductor 2DEGs as they may exhibit strong spin-orbit coupling along with possibility of harnessing high carrier concentrations [233,234]. STO has been employed as an active layer in numerous interfacial systems to characterize varieties of properties including 2DEGs at the interface [21,217]. However, STO suffers from low room temperature carrier mobilities due to electron-phonon scattering [235,236]. Alternative oxide semiconductors are needed to achieve large room-temperature 2DEG conductivities.

Compared to the Ti 3*d* states in STO, the $BaSnO_3$ conduction band is comprised primarily of Sn 5s states that exhibit strong orbital overlap and very little hybridization with O 2*p* states [237,238]. This produces a low effective mass and strong electronic dispersion, which is suitable for high electron mobility [239,240]. Additionally, high electrical conductivity along with optical transparency makes BSO as an outstanding candidate material for modern optoelectronic applications. With a Hall mobility as high as 320 $cm^2V^{-1}s^{-1}$, BSO has the highest room temperature mobility in complex metal oxides to the date at electron concentrations of with $8\times10^{19}cm^{-3}$ in a La-doped bulk BSO single crystal [50]. Due to these interesting characteristics, BSO has gained increasing attention as a candidate material for next-generation oxide optoelectronic devices. One challenge for the material, however, is increasing the doping levels due to band filling and compensating defects that may occur

at high dopant concentrations [241–243]. Compared to the bulk single crystal, BSO thin films have low mobility mainly due to threading dislocations from substrate misfit introduced [16] and point defects due to non-stoichiometry and scattering effects due to La dopant concentration [92]. In thin films, BSO has been employed as an active layer at perovskite oxide interface to harness the 2DEG at interface. $LaInO_3$/BSO [244,245] and La-doped $SrSnO_3$/BSO [246,247] heterostructures have been examined for better understanding of BSO-based oxide interface and exploration of 2DEG. However, polar/non-polar $LaInO_3$/BSO interfaces may suffer from interfacial defects common to the LAO/STO interface and the band alignment of La-doped $SrSnO_3$ produces minimal charge transfer into BSO.

$SrNbO_3$ has good potential as an interfacial electron donor because of the large gap between the O 2*p* and Nb 4*d* bands while maintaining a d^1 electronic structure [79]. As previously reported in density functional theory (DFT) studies on SNO/STO heterostructures, the band diagram of SNO displays the Nb 4*d* t_{2g} bands crossing the Fermi level, confirming its metallic nature, whereas the low work function and large separation between the O 2*p* and Nb 4*d* bands make SNO a promising donor [79]. Recent studies have shown that there is a great potential of SNO for interfacial charge transfer and topological phenomena such as spintronics [83,86]. Creating an epitaxial interface of SNO/BSO for modulation doping by charge transfer could produce greater carrier concentrations than have been possible previously. To achieve this, the conduction band offset must have BSO at lower potential compared to SNO to observe spillover of electrons to the BSO layer from SNO at the interface. On the other hand, the metastable nature of SNO demands extra care to provides suitable capping layer. Recent report on SNO synthesis has demonstrated that a $SrHfO_3$ capping layer is efficient for maintaining the metastable d^1 electronic state of SNO [87].

One of the essential aspects of a heterojunction is the band offsets at the interface of two semiconductors. Understanding the link between interfacial physical structure, electronic structure,

and carrier dynamics requires precise band offset measurements. Charge transfer occurs when two materials are stacked together to form an interface, balancing the electron chemical potential of both materials. To enhance carrier mobility in a 2DEG structure and reduce impurity scattering, isolation of charge carriers from the ionized dopant impurity is crucial in heterostructure engineering. Due to the purity provided by segregated donor and carrier sites and the challenges in avoiding defects at polar/non-polar interfaces, modulation doping is widely used these days in oxide heterostructures [217,248]. For years, it has been known that X-ray photoemission can provide a straightforward measurement for band offsets and charge transfer in oxide heterostructures [20,180]. This makes in situ XPS studies of 2DEGs grown by molecular beam epitaxy (MBE) particularly valuable for careful examination of interfacial phenomena [180].

In this work, density functional theory predictions are used to examine the band alignment and charge transfer between SNO and BSO. Experimental studies validate these predictions through the synthesis of metastable SNO films on BSO films deposited on Nb-doped STO substrates using hybrid molecular beam epitaxy. *In vacuo* X-ray photoelectron spectroscopy (XPS) is used to check the oxidation state of the Sn to measure the degree of charge transfer in the SNO/BSO interface. Angle-resolved XPS is used to verify the presence of a 2DEG structure at the interface.

7.2 Methods:

The SNO/BSO heterostructure is created by growing SNO on as prepared (110) BSO single crystal grown on Nb-doped STO substrate from Cornell University using hMBE approach as described elsewhere [87]. Some of the changes implemented are the growth chamber shroud walls were maintained at -60 °C compared to -30 °C via a closed loop chiller and low temperature fluid (Syltherm XLT, Dow Chemical) to effectively reduce the background water vapor pressure from the dissociated

TDTBN molecules and the hafnium precursor, tetrakis(ethylmethylamino) hafnium (TEMAH) flux is used due to the flux instability of hafnium tert-butoxide (HTB) as reported in the previous report. Hafnium was supplied through a gas source using a metalorganic precursor, (TEMAH) (99.99%, Sigma-Aldrich, USA) from a bubbler connected to the growth chamber without carrier gas.

In situ RHEED (Staib Instrument) was used to monitor the growth process and the quality of the film. Post-growth the samples were transferred from the MBE reactor to the PHI 5400 X-ray photoelectron spectroscopy (XPS) (Al Kα X-ray source) system through ultra-high vacuum (UHV) transfer line. An electron neutralizer gun was applied to compensate charging of the insulating samples [33]. The angle resolved X-ray photoelectron spectroscopy (ARXPS) was implemented to characterize the reduction of tin oxidation state by Sn 3d core level deconvolution with base pressure of ~1×10^{-9} Torr. Analysis of the ARXPS data was performed using CasaXPS [34, 35]. *Ex situ* atomic force microscopy measurement is carried out in uncapped sample to check the morphology of SNO film.

7.3 Results:

Figure 7.1 (a) shows the RHEED image for uncapped SNO sample grown on BSO along the [110] azimuth after the sample is cooled down. The RHEED patterns maintains reasonably strong diffraction spots with weak signature of Kikuchi bands which is related to the overoxidation of the film surface as described elsewhere [87]. Additionally, ex-situ atomic force microscopy (AFM) performed on uncapped sample to check the film surface morphology. Figure 7.1 (b) shows the AFM topography of an uncapped SNO film grown on a BSO substrate with a surface roughness of ~2.84 nm, reflecting a smooth film surface.

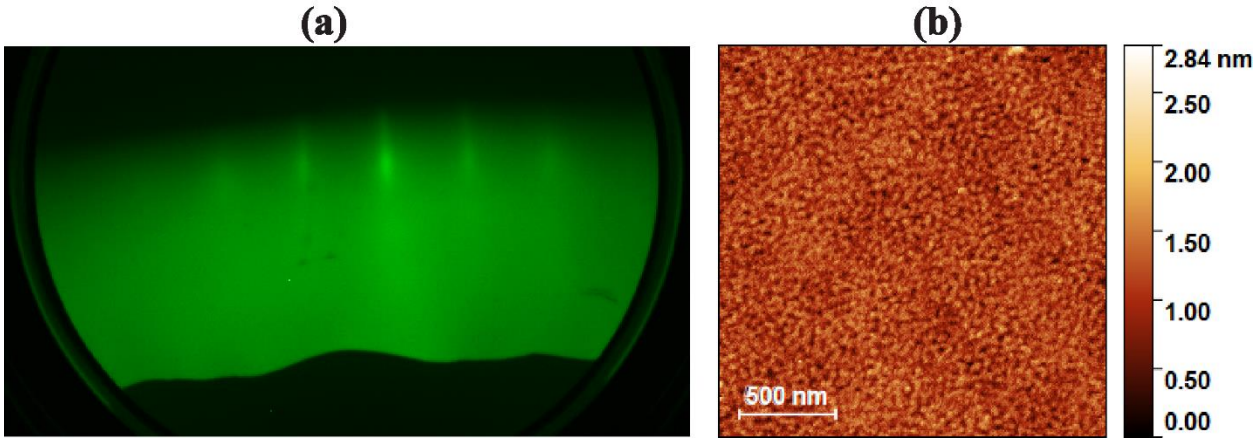

Figure 7.1: Uncapped sample (a) RHEED image along 110 azimuth after sample cool down (b) AFM topography.

The Sn 3*d* core level spectra for an uncapped sample and a SHO capped sample in reference to the plasma cleaned BSO on Nb:STO substrate at 45° and 70° photoelectron emission angles are shown in Figure 7.2 (a). In Figure 7.2 (a), Sn 3*d* core level at 45° photoelectron emission angle for similar thickness SNO film with SHO capping is also presented. The Sn 3*d* spin-orbit doublet shows the separation of ~8.45 eV which is in good agreement with the value reported elsewhere [249]. In an uncapped sample, an angle resolved XPS (ARXPS) measurements of the Sn 3*d* core level at shallower angle shows more prominent additional shoulder at lower binding energy compared to the 45° orientation. This extra shoulder at lower binding energy from ARXPS in Sn 3*d* core level is assigned to the Sn^{3+} states associated with Sn due to electron doping enhanced Sn reduction. Additionally, Sn $3d_{5/2}$ core level deconvolution of a substrate along with SHO capped sample is carried out using same constraints as for the uncapped sample. A plasma cleaned bare BSO on Nb:STO substrate shows non-existence of secondary peak at lower binding energy. To quantify this lower oxidation state associated with Sn, Sn $3d_{5/2}$ core level of uncapped sample is deconvoluted by constraining a second component

with same FWHM as the Sn^{4+} component and at 1.75 eV lower binding energy than the Sn^{4+} component as shown in Figure 7.2 (b) for 70° photoelectron emission angle.

Deconvolution of a capped sample exhibits that the SHO capping has largely improved the weight of extra peak at lower binding energy with an increase of ~450 % in Sn^{3+} peak area compared to the uncapped sample at photoelectron emission angle of 45°. This result suggests that the capping of SNO film surface is a key in preserving metastable state of SNO to donate free electrons to the BSO interface layer. These free electrons are most likely to fill Sn *s* state as predicted by previous works [52,239]. Similar to the traditional high mobility semiconductors [250], *s* orbital electronic behavior of Sn in interfacial BSO layer has a great role in improving mobility in oxide 2DEG applications.

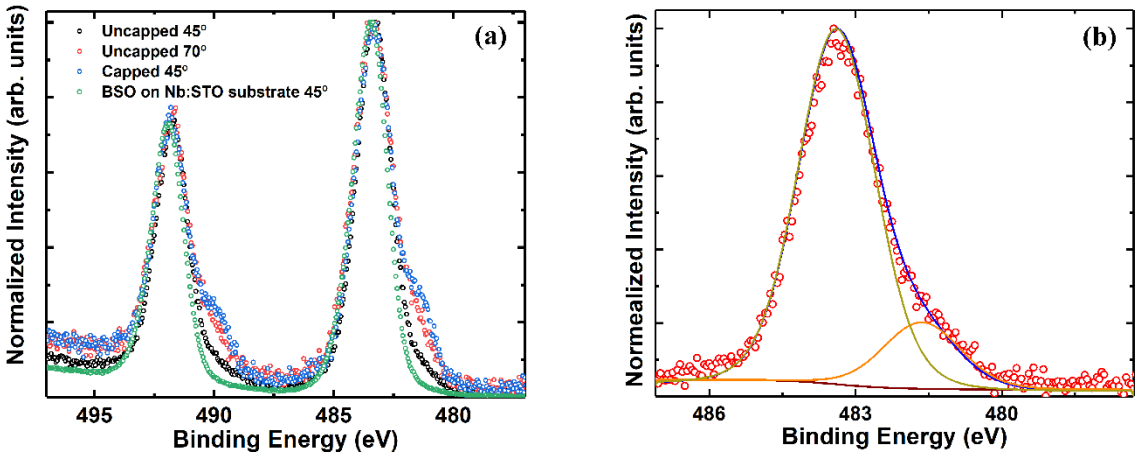

Figure 7.2: (a) Sn 3*d* core level for uncapped sample at 45° and 70° photoelectron emission angle and capped sample substrate at 45° photoelectron emission angles, (b) Sn 3*d*5/2 core level of an uncapped sample deconvolved for 70° photoelectron emission angle

In reference to the missing extra component in Sn 3*d* in plasma cleaned bare BSO on Nb:STO substrate, ARXPS analysis shows that the extra peak feature in Sn 3*d* is significant for uncapped sample. In a scatter plot with error bars, Figure 7.2 (b) shows the proportion of Sn^{3+} state observed in uncapped sample by deconvoluting the Sn $3d_{5/2}$ core level as a function of photoelectron emission angle from 45° to 70° at an interval of 5° in ARXPS analysis. An error bar within 2% in deconvoluting the Sn $3d_{5/2}$ core level indicates the consistency in our XPS area analysis. As the photoelectron emission angle becomes more shallower, an increasing trend of Sn^{3+} concentration in BSO layer is observed. This result shows that the Sn is significantly reduced at the interface BSO layer in the SNO/BSO heterostructure. We can safely rule out the possible reduction of BSO layer during substrate heating as the oxygen plasma was operated until the epitaxial SNO film deposition started.

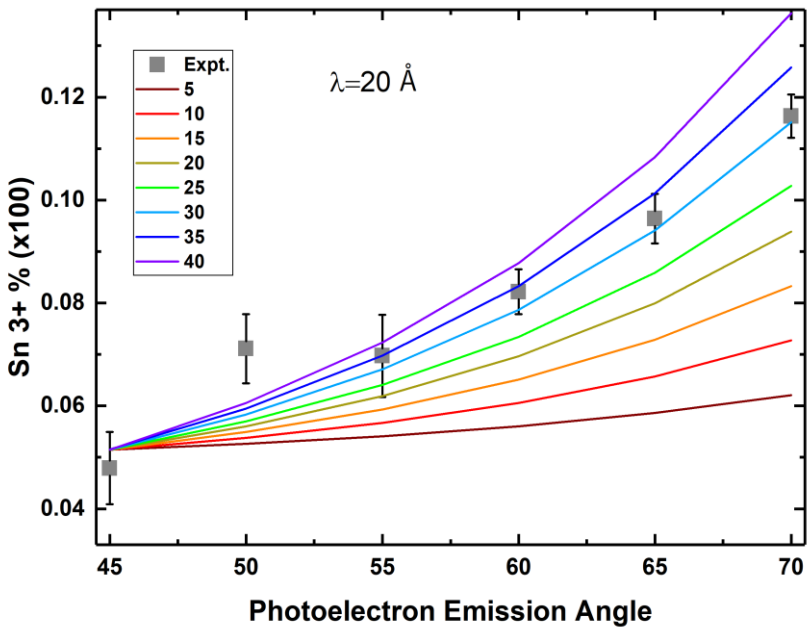

Figure 7.3: Scatter plot of Sn^{3+} electronic state as a function of photoelectron emission angle with error bars from angle resolved XPS experiment, and different Sn^{3+} decay concentration from a model.

A model is created to estimate the percentage of Sn^{3+} penetrating deep into the subsequent layer below the interface BSO layer. In this model, inelastic mean free path (IMFP) of 20 Å which is suitable for Sn. The BSO layer thickness up to 40 Å and relatively less sensitive Sn^{3+} decay model as a function of depth is considered which is shown in Figure 7.4 for 30 % Sn^{3+} at the interface. Different concentrations of Sn^{3+} at the interface is used in a model, ranging from 5% to 40% to generate multiple set of data to find the correlation with ARXPS data. On comparison, it is observed that the 30 % concentration of Sn^{3+} at the interface BSO layer fits relatively well with the experimental ARXPS showing reduction of nearly 15 % of Sn to Sn^{3+} state at the subsequent BSO layer next to the SNO/BSO interface.

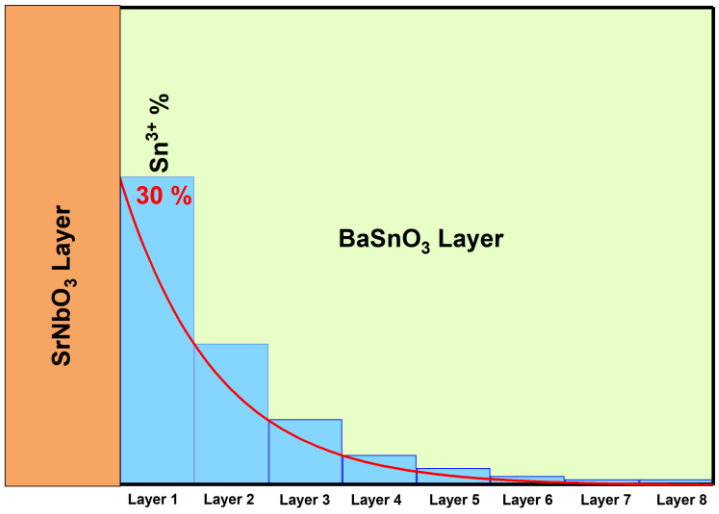

Figure 7.4: Sn^{3+} decay model as a function of BSO thickness

Considering one free electron for completely reduced Sn^{3+} from Sn^{4+} electronic state and taking 4.1 Å as a lattice parameter for BSO cubic unit cell structure, we have estimated the electron density and sheet carrier concentration at the interface BSO layer for 30% Sn^{3+} electronic states. Our calculation

shows that the electron density of 4.35×10^{21} cm^{-3} and sheet electron concentration of 1.78×10^{14} cm^{-2} is available at the interface BSO layer. Considering up to the six-unit cell of BSO layer starting from the interface leaves less than 1% of Sn^{3+} electronic states below the sixth BSO layer as per our Sn^{3+} decay model. Accounting up to six-unit cell of BSO layer from the interface, approximately 1.78×10^{21} cm^{-3} of electron density is observed. This result is useful in optimizing the 2DEG confinement at the SNO/BSO interface.

7.4 Discussion:

Growth of SNO on as grown BSO on Nb:STO by hMBE using the TDTBN precursor has been demonstrated. A suitable lattice match crystalline template, BSO helped to maintain the good quality of SNO film as shown by the RHEED and AFM measurements on uncapped samples. One challenge for films grown on Nb:STO was that strain relaxation in BSO produces a rougher initial surface compared to a bare substrate. Films grown on strained BSO below the critical thickness on $GdScO_3$ demonstrated smoother surfaces and a sharper RHEED pattern. Future studies could explore the growth of SNO on BSO substrates [251] or on BSO grown on a lattice matched substrate such as Ba_2ScNbO_6 [252].

Comparison of the Sn 3*d* spectra for a uniform BSO film to the samples with SNO and SHO-capped SNO, shows the presence of an extra peak at lower binding energy that indicates the charge transfer from SNO to BSO layer at the interface. The charge is shown to be localized at the SNO/BSO interface based on our ARXPS analysis. The estimated electron density of 4.35×10^{21} cm^{-3} in the interfacial BSO layer of SNO/BSO interface is significantly higher than other reports for La-doped BSO films [239,240], La-doped BSO single crystals [50,251], and oxygen-deficient BSO films [253] by at least a factor of 4 in all cases. Interestingly, our results agree semi-quantitatively with DFT

predictions of band filling in BSO by Krishnaswamy *et. al.* [254], who showed that carrier concentrations of ~10^{21} cm^{-3} would be expected if the conduction band minimum of BSO were lowered to 1.3 eV below the Fermi level. This corresponds well with DFT analysis by our collaborators, who indicate that the BSO/SNO interface should produce Sn 5*s* states 1.2 eV below the Fermi level [255].

The sheet electron concentration can be estimated from the ARXPS model to be at least 1.8×10^{14} cm^{-2} by accounting for only the interfacial layer of the BSO film. This value is roughly an order of magnitude larger than reports for $LaInO_3$/BSO polar/non-polar interfaces [244–246] and ~30x larger than modulation-doped La:$SrSnO_3$/BSO heterostructures [248]. We emphasize that these electron concentrations are calculated based on XPS rather than transport measurements due to the conductive nature of the SNO film, which is not expected to be depleted of electrons. Future studies could explore the role of a thin $SrHfO_3$-interfacial layer that permits some charge transfer into BSO while separating the BSO and SNO layers, as has been predicted by DFT for an analogous SNO/$SrZrO_3$/STO heterostructure [79].

While we cannot rule out the presence of some growth-induced oxygen vacancies at the interface, we do not believe that our results can be explained solely on the basis of oxygen vacancies. The samples were heated in oxygen plasma prior to growth to prevent reduction of the BSO and the plasma was only turned off at the beginning of the growth process, limiting the time for the BSO to reduce. Additionally, the intensity of the Sn^{3+} peak increases when the film is capped with $SrHfO_3$, which suggests that it is more sensitive to the number of electrons in SNO available for charge transfer rather than the oxygen environment during growth. Finally, predictions of BSO carrier concentrations in oxygen poor environments by DFT have indicated that carrier concentrations of ~10^{18}-10^{19} cm^{-3}

would be expected [256]. Previous work has shown that oxygen-deficient BSO films have electron concentrations of only ~10^{19} cm^{-3} [253], which is well below the values extracted from our studies.

These observations are remarkable for their potential applications in high mobility 2DEGs due to the low electron-phonon scattering and expected reduction in ionized impurity scattering in BSO from modulation doping [239,254]. A significantly larger degree of charge transfer to produce a Sn^{3+} electronic state is observed in the SHO-capped sample in comparison to the uncapped sample, demonstrating the significance of the SHO capping layer in preservation of the metastable SNO film. The diffusion of electrons deep into the BSO layer away from the interface BSO layer to sustain Sn^{3+} electronic states as suggested by our model is an interesting observation. However, lab-based ARXPS is relatively insensitive to this diffusion, which merits further study using advanced techniques such as hard X-ray photoemission (HAXPES) [237,248]. Due to the large degree of dispersion in for Sn 5s states in BSO, significantly greater electron diffusion into the film would be expected in comparison to the more localized transition metal *d* states that are commonly studied in oxide interfaces.

7.5 Conclusion:

In conclusion, SNO growth by hMBE approach using the metalorganic TDTBN precursor on BSO on Nb:STO substrate to create SNO/BSO heterostructure has been successfully demonstrated. The degree of charge transfer at the SNO/BSO interface is demonstrated from fitting of the Sn $3d_{5/2}$ oxidation state by XPS. A quantitative analysis of peak area under the curve shows that the capping layer of SHO has great role in improvement of charge transfer mechanism in SNO/BSO interface. ARXPS analysis of Sn 3*d* core level provides the signature of charge transfer in SNO/BSO heterostructure which opens the door for future investigation of charge transfer mechanism and

mobility measurement in SNO/BSO system. Based on our ARXPS results, the interface BSO layer contains ~30% Sn^{3+} electronic states, indicating considerable charge transfer from SNO to BSO that is at least an order of magnitude greater than previous reports. This degree of electronic concentration for this SNO/BSO system is highly promising for high mobility 2DEG applications.

Acknowledgements:

ST and RBC gratefully acknowledge support from the Air Force Office of Scientific Research under award number FA9550-20-1-0034 and Alabama EPSCoR-GRSP Fellowship.

Chapter 8

Conclusions and Future Work

8.1 Conclusions

This work has focused on the epitaxial growth of single crystal perovskite oxides $SrTiO_3$ (STO), $SrHfO_3$ (SHO) and $SrNbO_3$ (SNO) using the hybrid molecular beam epitaxy (hMBE) approach. It has demonstrated the effectiveness of metal organic precursors in supplying low vapor pressure transition metals Ti and Nb in STO and SNO synthesis by hMBE. The synthesis challenges associated with the growth of STO and SNO are discussed and resolved leading to high quality epitaxial thin films. The added difficulty due to the metastable nature of SNO thin films is appropriately addressed. The key focus of this study was to characterize the surface of STO and SNO thin films due to their impressive role in interfacial properties. Multiple thin film characterization techniques were employed to study the surface related properties including *in-vacuo* X-ray photoelectron spectroscopy (XPS), a major characterization tool used throughout the study. Despite some difficulties in quantitative analysis in XPS, qualitative analyses played a crucial role in accelerating the growth process. I have also created and studied an SNO/$BaSnO_3$ (BSO) interface by depositing SNO on an as-grown BSO layer using the hMBE approach for the first time. This novel SNO/BSO interface is characterized to investigate the charge transfer properties from the SNO layer to the interface BSO layer which carries great importance in high mobility 2DEG research.

The homoepitaxial STO synthesis is carried out using TTIP as a metal organic precursor by hMBE techniques. *In- situ* RHEED played a crucial role in monitoring film growth in real time. Our primary interest in stoichiometry and surface terminations of homoepitaxial STO films is addressed by *in-vacuo* XPS characterization for the first time. Our findings show that the SrO termination is needed

to synthesize a stoichiometric film, as measured by XRD. More importantly, RHEED, LEEM, LEED, and STM studies verify that surface reconstruction is associated with ideal film stoichiometry. Possible carbon contamination in the film is ruled out using *in-vauo* XPS and is likely due to high growth temperatures that help to maintain clean sample surfaces for interfacial characteristic integrity.

Synthesis of a metastable SNO thin film demonstrated the capabilities of the hMBE technique in utilizing a new TDTBN precursor for the first time. For preservation of a metastable state in SNO, a SHO capping layer was deposited immediately after the SNO growth which resulted in increasing electronic density of states near the Fermi level. XRD, XAS and XPS used to characterize the SNO thin film showed that both the quality and thickness of the capping layer are important in preserving the metastable state of SNO film surface. Most notably, this study opens the door for future exploration of interfacial phenomena in SNO related heterostructures, which has not been explored previously due to an unavailability of SNO films deposition by standard deposition technique, hMBE.

To study the possible charge transfer properties of SNO/BSO interfaces, SNO thin films were grown on BSO substrates using hMBE with a TDTBN precursor. The creation of these materials demonstrates their successful synthesis using the hMBE approach. RHEED and AFM show that the SNO films are high-quality. The qualitative study of charge transfer at the SNO/BSO interface is demonstrated from analysis of the Sn $3d_{5/2}$ core level from XPS scan. Peak area fitting under the curve is used to highlight the role of the SHO capping layers in improving the charge transfer mechanism at the SNO/BSO interface. XPS studies of the Sn 3*d* core level revealed a signature characteristic of charge transfer properties in SNO/BSO heterostructures thereby opening the door for future investigations into charge transfer mechanisms and mobility measurements.

8.2 Future Work

This dissertation provides a clear path for future research that seeks to improve the quality of metastable SNO thin films. Future studies could seek to tune SHO capping layer thicknesses which would preserve the SNO film surface after an exposure to the atmosphere but also allow for depth-sensitive characterization. Future work could involve the basic physical properties of the hMBE grown SNO films including investigating the band structure via angle resolved photoelectron spectroscopy (ARPES) [211] and crystal structure through various microscopy techniques. Also, improving the charge transfer properties at the SNO/BSO interface could be done by synthesizing or modeling SNO and BSO layers at varying thicknesses. Mobility measurements on SNO/BSO interfaces could be performed to investigate the material's high mobility applications as an alternative to the traditional wide band gap semiconductor based system [36]. Related to this, evaluation of the effective masses of conducting free electrons in the Sn *s* states would complement high mobility property investigations.

While care must be taken to maintain growth chamber cleanliness [95], consecutive SNO and BSO synthesis within the same MBE system may lead to increased purity at the SNO/BSO interface and may reveal properties that may not be observable in samples where SNO and BSO are grown in separate systems which involves atmospheric exposure. Complementary spectroscopy characterization using techniques such as hard X-ray photoelectron spectroscopy (HAXPES), which probes deeper into sample surfaces than standard XPS, could provide better understanding on the charge transfer mechanisms at the interface. These studies along with investigations into the physical properties of sample surfaces and interfaces provide future exploration opportunities in the field of high mobility oxide 2DEG materials.

References:

[1] M. L. Green, E. P. Gusev, R. Degraeve, and E. L. Garfunkel, *Ultrathin (<4 Nm) SiO2 and Si–O–N Gate Dielectric Layers for Silicon Microelectronics: Understanding the Processing, Structure, and Physical and Electrical Limits*, Journal of Applied Physics **90**, 2057 (2001).

[2] H. Ohta, M. Orita, M. Hirano, H. Tanji, H. Kawazoe, and H. Hosono, *Highly Electrically Conductive Indium–Tin–Oxide Thin Films Epitaxially Grown on Yttria-Stabilized Zirconia (100) by Pulsed-Laser Deposition*, Appl. Phys. Lett. **76**, 2740 (2000).

[3] D. G. Schlom, L.-Q. Chen, X. Pan, A. Schmehl, and M. A. Zurbuchen, *A Thin Film Approach to Engineering Functionality into Oxides*, Journal of the American Ceramic Society **91**, 2429 (2008).

[4] V. M. Goldschmidt, *Die Gesetze der Krystallochemie*, Naturwissenschaften **14**, 477 (1926).

[5] M. A. Peña and J. L. G. Fierro, *Chemical Structures and Performance of Perovskite Oxides*, Chem. Rev. **101**, 1981 (2001).

[6] A. L. Companion and M. A. Komarynsky, *Crystal Field Splitting Diagrams*, J. Chem. Edu. **41, 5, 257** (1964).

[7] *Stability of Polyatomic Molecules in Degenerate Electronic States - I—Orbital Degeneracy | Proceedings of the Royal Society of London. Series A - Mathematical and Physical Sciences*, https://royalsocietypublishing.org/doi/abs/10.1098/rspa.1937.0142.

[8] O. Diéguez, K. M. Rabe, and D. Vanderbilt, *First-Principles Study of Epitaxial Strain in Perovskites*, Phys. Rev. B **72**, 144101 (2005).

[9] A. Munkholm, S. K. Streiffer, M. V. Ramana Murty, J. A. Eastman, C. Thompson, O. Auciello, L. Thompson, J. F. Moore, and G. B. Stephenson, *Antiferrodistortive Reconstruction of the PbTiO3(001) Surface*, Phys. Rev. Lett. **88**, 016101 (2001).

[10] M. L. Medarde, *Structural, Magnetic and Electronic Properties of Perovskites (R = Rare Earth)*, J. Phys.: Condens. Matter **9**, 1679 (1997).

[11] T. Shimizu, D. Suwama, H. Taniguchi, T. Taniyama, and M. Itoh, *Comparative Study of Phase Transitions in BaTiO3 Thin Films Grown on (001)- and (110)-Oriented SrTiO3 Substrate*, J. Phys.: Condens. Matter **25**, 132001 (2013).

[12] J. L. Giocondi and G. S. Rohrer, *Structure Se Nsitivity of Photochemical Oxidation and Reduction Reactions on SrTiO3 Surfaces*, Journal of the American Ceramic Society **86**, 1182 (2003).

[13] J. L. Giocondi, P. A. Salvador, and G. S. Rohrer, *The Origin of Photochemical Anisotropy in SrTiO3*, Top Catal **44**, 529 (2007).

[14] D. O. Scanlon, *Defect Engineering of BaSnO3 for High-Performance Transparent Conducting Oxide Applications*, Phys. Rev. B **87**, 161201 (2013).

[15] J. Son, P. Moetakef, B. Jalan, O. Bierwagen, N. J. Wright, R. Engel-Herbert, and S. Stemmer, *Epitaxial SrTiO3 Films with Electron Mobilities Exceeding 30,000 Cm2 V−1 S−1*, Nature Mater **9**, 482 (2010).

[16] S. Raghavan, T. Schumann, H. Kim, J. Y. Zhang, T. A. Cain, and S. Stemmer, *High-Mobility BaSnO3 Grown by Oxide Molecular Beam Epitaxy*, APL Materials **4**, 016106 (2016).

[17] Z. Yang, B. H. Babu, S. Wu, T. Liu, S. Fang, Z. Xiong, L. Han, and W. Chen, *Review on Practical Interface Engineering of Perovskite Solar Cells: From Efficiency to Stability*, Solar RRL **4**, 1900257 (2020).

[18] Y. Liu, Z. Hong, Q. Chen, H. Chen, W.-H. Chang, Y. (Michael) Yang, T.-B. Song, and Y. Yang, *Perovskite Solar Cells Employing Dopant-Free Organic Hole Transport Materials with Tunable Energy Levels*, Advanced Materials **28**, 440 (2016).

[19] L. W. Martin, Y.-H. Chu, and R. Ramesh, *Advances in the Growth and Characterization of Magnetic, Ferroelectric, and Multiferroic Oxide Thin Films*, Materials Science and Engineering: R: Reports **68**, 89 (2010).

[20] S. A. Chambers, T. C. Kaspar, A. Prakash, G. Haugstad, and B. Jalan, *Band Alignment at Epitaxial BaSnO3/SrTiO3(001) and BaSnO3/LaAlO3(001) Heterojunctions*, Appl. Phys. Lett. **108**, 152104 (2016).

[21] A. Ohtomo and H. Y. Hwang, *A High-Mobility Electron Gas at the LaAlO3/SrTiO3 Heterointerface*, Nature **427**, 423 (2004).

[22] W. Siemons, G. Koster, H. Yamamoto, W. A. Harrison, G. Lucovsky, T. H. Geballe, D. H. A. Blank, and M. R. Beasley, *Origin of Charge Density at LaAlO3 on SrTiO3 Heterointerfaces: Possibility of Intrinsic Doping*, Phys. Rev. Lett. **98**, 196802 (2007).

[23] T. Khan, H. Zhang, H. Zhang, Z. Yang, J. Song, J. Zhang, X. Chen, Y. Chen, B. Shen, and J. Sun, *Two-Dimensional Electron Gas at Manganite Buffered LaAlO3/SrTiO3 (001) Interface by Spin Coating Chemical Methods*, Appl. Phys. Lett. **113**, 071601 (2018).

[24] N. Reyren, S. Thiel, A. D. Caviglia, L. F. Kourkoutis, G. Hammerl, C. Richter, C. W. Schneider, T. Kopp, A.-S. Rüetschi, D. Jaccard, M. Gabay, D. A. Muller, J.-M. Triscone, and J. Mannhart, *Superconducting Interfaces Between Insulating Oxides*, Science **317**, 1196 (2007).

[25] A. D. Caviglia, S. Gariglio, N. Reyren, D. Jaccard, T. Schneider, M. Gabay, S. Thiel, G. Hammerl, J. Mannhart, and J.-M. Triscone, *Electric Field Control of the LaAlO3/SrTiO3 Interface Ground State*, Nature **456**, 7222 (2008).

[26] F. Gunkel, S. Wicklein, S. Hoffmann-Eifert, P. Meuffels, P. Brinks, M. Huijben, G. Rijnders, R. Waser, and R. Dittmann, *Transport Limits in Defect-Engineered LaAlO 3 /SrTiO 3 Bilayers*, Nanoscale **7**, 1013 (2015).

[27] D.-S. Park, A. D. Rata, I. V. Maznichenko, S. Ostanin, Y. L. Gan, S. Agrestini, G. J. Rees, M. Walker, J. Li, J. Herrero-Martin, G. Singh, Z. Luo, A. Bhatnagar, Y. Z. Chen, V. Tileli, P. Muralt, A. Kalaboukhov, I. Mertig, K. Dörr, A. Ernst, and N. Pryds, *The Emergence of Magnetic Ordering at Complex Oxide Interfaces Tuned by Defects*, Nat Commun **11**, 1 (2020).

[28] W. A. Harrison, E. A. Kraut, J. R. Waldrop, and R. W. Grant, *Polar Heterojunction Interfaces*, Phys. Rev. B **18**, 4402 (1978).

[29] G. A. Baraff, J. A. Appelbaum, and D. R. Hamann, *Self-Consistent Calculation of the Electronic Structure at an Abrupt GaAs-Ge Interface*, Phys. Rev. Lett. **38**, 237 (1977).

[30] D. C. Tsui, H. L. Stormer, and A. C. Gossard, *Two-Dimensional Magnetotransport in the Extreme Quantum Limit*, Phys. Rev. Lett. **48**, 1559 (1982).

[31] A. Tsukazaki, S. Akasaka, K. Nakahara, Y. Ohno, H. Ohno, D. Maryenko, A. Ohtomo, and M. Kawasaki, *Observation of the Fractional Quantum Hall Effect in an Oxide*, Nature Mater **9**, 11 (2010).

[32] S. Stemmer and S. James Allen, *Two-Dimensional Electron Gases at Complex Oxide Interfaces*, Annual Review of Materials Research **44**, 151 (2014).

[33] L. Brus, *Size, Dimensionality, and Strong Electron Correlation in Nanoscience*, Acc. Chem. Res. **47**, 2951 (2014).

[34] H. Y. Hwang, Y. Iwasa, M. Kawasaki, B. Keimer, N. Nagaosa, and Y. Tokura, *Emergent Phenomena at Oxide Interfaces*, Nature Mater **11**, 2 (2012).

[35] P. Yu, Y.-H. Chu, and R. Ramesh, *Oxide Interfaces: Pathways to Novel Phenomena*, Materials Today **15**, 320 (2012).

[36] Y. Chen and R. J. Green, *Progress and Perspectives of Atomically Engineered Perovskite Oxide Interfaces for Electronics and Electrocatalysts*, Advanced Materials Interfaces **6**, 1900547 (2019).

[37] J. Mannhart, D. H. A. Blank, H. Y. Hwang, A. J. Millis, and J.-M. Triscone, *Two-Dimensional Electron Gases at Oxide Interfaces*, MRS Bulletin **33**, 1027 (2008).

[38] H. Inoue, H. Yoon, T. A. Merz, A. G. Swartz, S. S. Hong, Y. Hikita, and H. Y. Hwang, *Delta-Doped SrTiO $_3$ Top-Gated Field Effect Transistor*, Appl. Phys. Lett. **114**, 231605 (2019).

[39] Y. Kozuka, M. Kim, H. Ohta, Y. Hikita, C. Bell, and H. Y. Hwang, *Enhancing the Electron Mobility via Delta-Doping in SrTiO3*, Appl. Phys. Lett. **97**, 222115 (2010).

[40] P. Xu, Y. Ayino, C. Cheng, V. S. Pribiag, R. B. Comes, P. V. Sushko, S. A. Chambers, and B. Jalan, *Predictive Control over Charge Density in the Two-Dimensional Electron Gas at the Polar-Nonpolar NdTiO3/SrTiO3 Interface*, Phys. Rev. Lett. **117**, 106803 (2016).

[41] G.-Q. Hai, N. Studart, and F. M. Peeters, *Multisubband Electron Transport in δ-Doped Semiconductor Systems*, Phys. Rev. B **52**, 8363 (1995).

[42] A. Prakash, N. F. Quackenbush, H. Yun, J. Held, T. Wang, T. Truttmann, J. M. Ablett, C. Weiland, T.-L. Lee, J. C. Woicik, K. A. Mkhoyan, and B. Jalan, *Separating Electrons and Donors in $BaSnO_3$ via Band Engineering*, Nano Lett. **19**, 8920 (2019).

[43] A. Brinkman, M. Huijben, M. van Zalk, J. Huijben, U. Zeitler, J. C. Maan, W. G. van der Wiel, G. Rijnders, D. H. A. Blank, and H. Hilgenkamp, *Magnetic Effects at the Interface between Non-Magnetic Oxides*, Nature Materials **6**, 7 (2007).

[44] D. A. Dikin, M. Mehta, C. W. Bark, C. M. Folkman, C. B. Eom, and V. Chandrasekhar, *Coexistence of Superconductivity and Ferromagnetism in Two Dimensions*, Phys. Rev. Lett. **107**, 056802 (2011).

[45] L. Li, C. Richter, J. Mannhart, and R. C. Ashoori, *Coexistence of Magnetic Order and Two-Dimensional Superconductivity at LaAlO3/SrTiO3 Interfaces*, Nature Phys **7**, 10 (2011).

[46] A. Soumyanarayanan, N. Reyren, A. Fert, and C. Panagopoulos, *Emergent Phenomena Induced by Spin–Orbit Coupling at Surfaces and Interfaces*, Nature **539**, 7630 (2016).

[47] L. Yu and A. Zunger, *A Polarity-Induced Defect Mechanism for Conductivity and Magnetism at Polar–Nonpolar Oxide Interfaces*, Nat Commun **5**, 1 (2014).

[48] N. Nakagawa, H. Y. Hwang, and D. A. Muller, *Why Some Interfaces Cannot Be Sharp*, Nature Mater **5**, 204 (2006).

[49] S. A. Pauli, S. J. Leake, B. Delley, M. Björck, C. W. Schneider, C. M. Schlepütz, D. Martoccia, S. Paetel, J. Mannhart, and P. R. Willmott, *Evolution of the Interfacial Structure of LaAlO3 on SrTiO3*, Phys. Rev. Lett. **106**, 036101 (2011).

[50] H. J. Kim, U. Kim, Kim, T. H. Kim, H. S. Mun, B.-G. Jeon, K. T. Hong, W.-J. Lee, C. Ju, K. H. Kim, and K. Char, *High Mobility in a Stable Transparent Perovskite Oxide*, Appl. Phys. Express **5**, 061102 (2012).

[51] Q. X. Jia, J. P. Zheng, H. S. Kwok, and W. A. Anderson, *Indium Tin Oxide on InP by Pulsed Laser Deposition*, Thin Solid Films **258**, 260 (1995).

[52] H. He, Z. Yang, Y. Xu, A. T. Smith, G. Yang, and L. Sun, *Perovskite Oxides as Transparent Semiconductors: A Review*, Nano Convergence **7**, 32 (2020).

[53] M. A. Riza, M. A. Ibrahim, U. C. Ahamefula, M. A. Mat Teridi, N. Ahmad Ludin, S. Sepeai, and K. Sopian, *Prospects and Challenges of Perovskite Type Transparent Conductive Oxides in Photovoltaic Applications. Part I – Material Developments*, Solar Energy **137**, 371 (2016).

[54] R. Khymyn, I. Lisenkov, V. Tiberkevich, B. A. Ivanov, and A. Slavin, *Antiferromagnetic THz-Frequency Josephson-like Oscillator Driven by Spin Current*, Sci Rep **7**, 1 (2017).

[55] R. Cheng, D. Xiao, and A. Brataas, *Terahertz Antiferromagnetic Spin Hall Nano-Oscillator*, Phys. Rev. Lett. **116**, 207603 (2016).

[56] T. Ohnishi, K. Shibuya, T. Yamamoto, and M. Lippmaa, *Defects and Transport in Complex Oxide Thin Films*, Journal of Applied Physics **103**, 103703 (2008).

[57] *Band Gap Engineering of SrTiO3 for Water Splitting under Visible Light Irradiation | Elsevier Enhanced Reader*, https://doi.org/10.1016/j.ijhydene.2014.06.059.

[58] T. Ohnishi, K. Shibuya, T. Yamamoto, and M. Lippmaa, *Defects and Transport in Complex Oxide Thin Films*, Journal of Applied Physics **103**, 103703 (2008).

[59] B. Jalan, R. Engel-Herbert, N. J. Wright, and S. Stemmer, *Growth of High-Quality SrTiO3 Films Using a Hybrid Molecular Beam Epitaxy Approach*, Journal of Vacuum Science & Technology A **27**, 461 (2009).

[60] C. M. Brooks, L. F. Kourkoutis, T. Heeg, J. Schubert, D. A. Muller, and D. G. Schlom, *Growth of Homoepitaxial SrTiO3 Thin Films by Molecular-Beam Epitaxy*, Appl. Phys. Lett. **94**, 162905 (2009).

[61] C. Mitra, C. Lin, J. Robertson, and A. A. Demkov, *Electronic Structure of Oxygen Vacancies in SrTiO3 and LaAlO3*, Phys. Rev. B **86**, 155105 (2012).

[62] M. Lippmaa, M. Kawasaki, A. Ohtomo, T. Sato, M. Iwatsuki, and H. Koinuma, *Observation of SrTiO3 Step Edge Dynamics by Real-Time High-Temperature STM*, Applied Surface Science **130–132**, 582 (1998).

[63] M. R. Castell, *Scanning Tunneling Microscopy of Reconstructions on the SrTiO3(001) Surface*, Surface Science **505**, 1 (2002).

[64] T. Kubo and H. Nozoye, *Surface Structure of SrTiO3(100)-(Square Root of 5 x Square Root of 5) - R26.6 Degrees.*, Physical Review Letters (2001).

[65] T. Kimura, H. Yamauchi, H. Machida, H. Kokubun, and M. Y. M. Yamada, *Synthesis of Novel Sr Sources for Metalorganic Chemical Vapor Deposition of SrTiO3*, Jpn. J. Appl. Phys. **33**, 5119 (1994).

[66] D. G. Schlom, J. H. Haeni, J. Lettieri, C. D. Theis, W. Tian, J. C. Jiang, and X. Q. Pan, *Oxide Nano-Engineering Using MBE*, Materials Science and Engineering: B **87**, 282 (2001).

[67] J. H. Haeni, C. D. Theis, and D. G. Schlom, *RHEED Intensity Oscillations for the Stoichiometric Growth of SrTiO3 Thin Films by Reactive Molecular Beam Epitaxy*, Journal of Electroceramics **4**, 385 (2000).

[68] S. Thapa, S. R. Provence, D. Jessup, J. Lapano, M. Brahlek, J. T. Sadowski, P. Reinke, W. Jin, and R. B. Comes, *Correlating Surface Stoichiometry and Termination in SrTiO3 Films Grown by Hybrid Molecular Beam Epitaxy*, Journal of Vacuum Science & Technology A **39**, 053203 (2021).

[69] L. Zhang and R. Engel-Herbert, *Growth of SrTiO3 on Si(001) by Hybrid Molecular Beam Epitaxy*, Physica Status Solidi (RRL) – Rapid Research Letters **8**, 917 (2014).

[70] A. P. Kajdos and S. Stemmer, *Surface Reconstructions in Molecular Beam Epitaxy of SrTiO3*, Appl. Phys. Lett. **105**, 191901 (2014).

[71] C. Lee, J. Destry, and J. L. Brebner, *Optical Absorption and Transport in Semiconducting SrTiO3*, Phys. Rev. B **11**, 2299 (1975).

[72] T. Fix, R. Bali, N. Stelmashenko, and M. G. Blamire, *Influence of the Dopant Concentration in In-Doped SrTiO3 on the Structural and Transport Properties*, Solid State Communications **146**, 428 (2008).

[73] P. Kumar, A. Dogra, P. P. S. Bhadauria, A. Gupta, K. K. Maurya, and R. C. Budhani, *Enhanced Spin–Orbit Coupling and Charge Carrier Density Suppression in LaAl1-XCrxO3/SrTiO3hetero-Interfaces*, J. Phys.: Condens. Matter **27**, 125007 (2015).

[74] K. Nakamura, H. Mashiko, K. Yoshimatsu, and A. Ohtomo, *Impact of Built-in Potential across LaFeO3/SrTiO3 Heterojunctions on Photocatalytic Activity*, Appl. Phys. Lett. **108**, 211605 (2016).

[75] R. Comes and S. Chambers, *Interface Structure, Band Alignment, and Built-In Potentials at LaFeO3/n-SrTiO3 Heterojunctions*, Phys. Rev. Lett. **117**, 226802 (2016).

[76] M. Nakamura, F. Kagawa, T. Tanigaki, H. S. Park, T. Matsuda, D. Shindo, Y. Tokura, and M. Kawasaki, *Spontaneous Polarization and Bulk Photovoltaic Effect Driven by Polar Discontinuity in LaFeO3/SrTiO3 Heterojunctions*, Phys. Rev. Lett. **116**, 156801 (2016).

[77] D. Oka, Y. Hirose, S. Nakao, T. Fukumura, and T. Hasegawa, *Intrinsic High Electrical Conductivity of Stoichiometric SrNbO3 Epitaxial Thin Films*, Phys. Rev. B **92**, 205102 (2015).

[78] Z. Zhong and P. Hansmann, *Tuning the Work Function in Transition Metal Oxides and Their Heterostructures*, Phys. Rev. B **93**, 235116 (2016).

[79] Z. Zhong and P. Hansmann, *Band Alignment and Charge Transfer in Complex Oxide Interfaces*, Phys. Rev. X **7**, 011023 (2017).

[80] J. Roth, A. Paul, N. Goldner, A. Pogrebnyakov, K. Agueda, T. Birol, N. Alem, and R. Engel-Herbert, *Sputtered Sr XNbO3as a UV-Transparent Conducting Film*, ACS Applied Materials & Interfaces **12**, 30520 (2020).

[81] M. Mirjolet, M. Kataja, T. K. Hakala, P. Komissinskiy, L. Alff, G. Herranz, and J. Fontcuberta, *Optical Plasmon Excitation in Transparent Conducting SrNbO3 and SrVO3 Thin Films*, Advanced Optical Materials **9**, 2100520 (2021).

[82] Y. Park, J. Roth, D. Oka, Y. Hirose, T. Hasegawa, A. Paul, A. Pogrebnyakov, V. Gopalan, T. Birol, and R. Engel-Herbert, *SrNbO3 as a Transparent Conductor in the Visible and Ultraviolet Spectra*, Communications Physics **3**, (2020).

[83] J. M. Ok, N. Mohanta, J. Zhang, S. Yoon, S. Okamoto, E. S. Choi, H. Zhou, M. Briggeman, P. Irvin, A. R. Lupini, Y.-Y. Pai, E. Skoropata, C. Sohn, H. Li, H. Miao, B. Lawrie, W. S. Choi, G. Eres, J. Levy, and H. N. Lee, *Correlated Oxide Dirac Semimetal in the Extreme Quantum Limit*, Sci Adv **7**, eabf9631 (2021).

[84] C. Bigi, P. Orgiani, J. Sławińska, J. Fujii, J. T. Irvine, S. Picozzi, G. Panaccione, I. Vobornik, G. Rossi, D. Payne, and F. Borgatti, *Direct Insight into the Band Structure of SrNbO3*, Phys. Rev. Materials **4**, 025006 (2020).

[85] J. M. Ok, N. Mohanta, J. Zhang, S. Yoon, S. Okamoto, E. S. Choi, H. Zhou, M. Briggeman, P. Irvin, A. R. Lupini, Y.-Y. Pai, E. Skoropata, C. Sohn, H. Li, H. Miao, B. Lawrie, W. S. Choi, G. Eres, J. Levy, and H. N. Lee, *Correlated Oxide Dirac Semimetal in the Extreme Quantum Limit*, Sci. Adv. **7**, eabf9631 (2021).

[86] J. Zhang, J. M. Ok, Y.-Y. Pai, J. Lapano, E. Skoropata, A. R. Mazza, H. Li, A. Huon, S. Yoon, B. Lawrie, M. Brahlek, T. Z. Ward, G. Eres, H. Miao, and H. N. Lee, *Extremely Large Magnetoresistance in High-Mobility SrNbO3/SrTiO3 Heterostructures*, Phys. Rev. B **104**, L161404 (2021).

[87] S. Thapa, S. Provence, S. M. Heald, M. A. Kuroda, and R. B. Comes, *Surface Stability of $SrNbO_{3+\delta}$ Grown by Hybrid Molecular Beam Epitaxy*, ArXiv:2110.15341 [Cond-Mat] (2021).

[88] D. O. Scanlon, *Defect Engineering of BaSnO 3 for High-Performance Transparent Conducting Oxide Applications*, Phys. Rev. B **87**, 161201 (2013).

[89] S. Sallis, D. O. Scanlon, S. C. Chae, N. F. Quackenbush, D. A. Fischer, J. C. Woicik, J.-H. Guo, S. W. Cheong, and L. F. J. Piper, *La-Doped $BaSnO_3$ —Degenerate Perovskite Transparent Conducting Oxide: Evidence from Synchrotron x-Ray Spectroscopy*, Appl. Phys. Lett. **103**, 042105 (2013).

[90] X. Luo, Y. S. Oh, A. Sirenko, P. Gao, T. A. Tyson, K. Char, and S.-W. Cheong, *High Carrier Mobility in Transparent Ba1−xLaxSnO3 Crystals with a Wide Band Gap*, Appl. Phys. Lett. **100**, 172112 (2012).

[91] H. J. Kim, U. Kim, T. H. Kim, J. Kim, H. M. Kim, B.-G. Jeon, W.-J. Lee, H. S. Mun, K. T. Hong, J. Yu, K. Char, and K. H. Kim, *Physical Properties of Transparent Perovskite Oxides (Ba,La)SnO3 with High Electrical Mobility at Room Temperature*, Phys. Rev. B **86**, 165205 (2012).

[92] H.-R. Liu, J.-H. Yang, H. J. Xiang, X. G. Gong, and S.-H. Wei, *Origin of the Superior Conductivity of Perovskite Ba(Sr)SnO3*, Appl. Phys. Lett. **102**, 112109 (2013).

[93] A. Prakash, P. Xu, X. Wu, G. Haugstad, X. Wang, and B. Jalan, *Adsorption-Controlled Growth and the Influence of Stoichiometry on Electronic Transport in Hybrid Molecular Beam Epitaxy-Grown BaSnO3 Films*, J. Mater. Chem. C **5**, 5730 (2017).

[94] A. Prakash, P. Xu, A. Faghaninia, S. Shukla, J. W. Ager, C. S. Lo, and B. Jalan, *Wide Bandgap BaSnO3 Films with Room Temperature Conductivity Exceeding 104 S Cm−1*, Nat Commun **8**, 15167 (2017).

[95] A. Sharma, S. E. Watkins, D. A. Lewis, and G. Andersson, *Effect of Indium and Tin Contamination on the Efficiency and Electronic Properties of Organic Bulk Hetero-Junction Solar Cells*, Solar Energy Materials and Solar Cells **95**, 3251 (2011).

[96] K. Ploog, A. Fischer, R. Trommer, and M. Hirose, *MBE-grown Insulating Oxide Films on GaAs*, Journal of Vacuum Science and Technology **16**, 290 (1979).

[97] R. A. Betts and C. W. Pitt, *Growth of Thin-Film Lithium Niobate by Molecular Beam Epitaxy*, Electronics Letters **21**, 960 (1985).

[98] M. R. Norman, *The Challenge of Unconventional Superconductivity*, Science **332**, 196 (2011).

[99] E. G. Maksimov, *High-Temperature Superconductivity: The Current State*, Phys.-Usp. **43**, 965 (2000).

[100] D. D. Berkley, B. R. Johnson, N. Anand, K. M. Beauchamp, L. E. Conroy, A. M. Goldman, J. Maps, K. Mauersberger, M. L. Mecartney, J. Morton, M. Tuominen, and Y. Zhang, *In Situ Formation of Superconducting YBa2Cu3O$_{7-x}$ Thin Films Using Pure Ozone Vapor Oxidation*, Appl. Phys. Lett. **53**, 1973 (1988).

[101] D. G. Schlom, J. N. Eckstein, E. S. Hellman, S. K. Streiffer, J. S. Harris, M. R. Beasley, J. C. Bravman, T. H. Geballe, C. Webb, K. E. von Dessonneck, and F. Turner, *Molecular Beam Epitaxy of Layered Dy-Ba-Cu-O Compounds*, Appl. Phys. Lett. **53**, 1660 (1988).

[102] B. Jalan, J. Cagnon, T. E. Mates, and S. Stemmer, *Analysis of Carbon in SrTiO3 Grown by Hybrid Molecular Beam Epitaxy*, Journal of Vacuum Science & Technology A **27**, 1365 (2009).

[103] D. G. Schlom, Molecular Beam Epitaxial Growth of Cuprate Superconductors and Related Phases, PhD Thesis, Stanford University, 1990.

[104] R. F. C. Farrow, *Molecular Beam Epitaxy: Applications to Key Materials* (Elsevier, 1995).

[105] K. S. K. Sakurai, D. I. D. Iwata, S. F. S. Fujita, and S. F. S. Fujita, *Growth of ZnO by Molecular Beam Epitaxy Using NO2 as Oxygen Source*, Jpn. J. Appl. Phys. **38**, 2606 (1999).

[106] M. Ritala, T. Asikainen, and M. Leskelä, *Enhanced Growth Rate in Atomic Layer Epitaxy of Indium Oxide and Indium-Tin Oxide Thin Films*, Electrochem. Solid-State Lett. **1**, 156 (1998).

[107] F. C. Voogt, P. J. M. Smulders, G. H. Wijnja, L. Niesen, T. Fujii, M. A. James, and T. Hibma, *NO2-Assisted Molecular-Beam Epitaxy of Wustitelike and Magnetitelike Fe Oxynitride Films on MgO(100)*, Phys. Rev. B **63**, 125409 (2001).

[108] N. Izyumskaya, V. Avrutin, W. Schoch, A. El-Shaer, F. Reuß, Th. Gruber, and A. Waag, *Molecular Beam Epitaxy of High-Quality ZnO Using Hydrogen Peroxide as an Oxidant*, Journal of Crystal Growth **269**, 356 (2004).

[109] C. D. Theis and D. G. Schlom, *Cheap and Stable Titanium Source for Use in Oxide Molecular Beam Epitaxy Systems*, Journal of Vacuum Science & Technology A: Vacuum, Surfaces, and Films **14**, 2677 (1996).

[110] E. S. Hellman and E. H. Hartford, *Effects of Oxygen on the Sublimation of Alkaline Earths from Effusion Cells*, Journal of Vacuum Science & Technology B: Microelectronics and Nanometer Structures Processing, Measurement, and Phenomena **12**, 1178 (1994).

[111] J. R. Arthur, *Interaction of Ga and As $_2$ Molecular Beams with GaAs Surfaces*, Journal of Applied Physics **39**, 4032 (1968).

[112] C. D. Theis, J. Yeh, D. G. Schlom, M. E. Hawley, and G. W. Brown, *Adsorption-Controlled Growth of PbTiO3 by Reactive Molecular Beam Epitaxy*, Thin Solid Films **325**, 107 (1998).

[113] M. Brahlek, A. S. Gupta, J. Lapano, J. Roth, H.-T. Zhang, L. Zhang, R. Haislmaier, and R. Engel-Herbert, *Frontiers in the Growth of Complex Oxide Thin Films: Past, Present, and Future of Hybrid MBE*, Advanced Functional Materials **28**, 1702772 (2018).

[114] J. L. MacManus-Driscoll, M. P. Wells, C. Yun, J.-W. Lee, C.-B. Eom, and D. G. Schlom, *New Approaches for Achieving More Perfect Transition Metal Oxide Thin Films*, APL Materials **8**, 040904 (2020).

[115] B. Jalan, P. Moetakef, and S. Stemmer, *Molecular Beam Epitaxy of SrTiO3 with a Growth Window*, Appl. Phys. Lett. **95**, 032906 (2009).

[116] T. A. Cain, A. P. Kajdos, and S. Stemmer, *La-Doped SrTiO3 Films with Large Cryogenic Thermoelectric Power Factors*, Appl. Phys. Lett. **102**, 182101 (2013).

[117] O. N. Tufte and P. W. Chapman, *Electron Mobility in Semiconducting Strontium Titanate*, Phys. Rev. **155**, 796 (1967).

[118] Y. Kozuka, Y. Hikita, C. Bell, and H. Y. Hwang, *Dramatic Mobility Enhancements in Doped SrTiO3 Thin Films by Defect Management*, Appl. Phys. Lett. **97**, 012107 (2010).

[119] Y. Matsubara, K. S. Takahashi, Y. Tokura, and M. Kawasaki, *Single-Crystalline BaTiO3 Films Grown by Gas-Source Molecular Beam Epitaxy*, Appl. Phys. Express **7**, 125502 (2014).

[120] J. Roth, E. Arriaga, M. Brahlek, J. Lapano, and R. Engel-Herbert, *Temperature-Dependent Growth Window of CaTiO3 Films Grown by Hybrid Molecular Beam Epitaxy*, Journal of Vacuum Science & Technology A **36**, 020601 (2018).

[121] M. Brahlek, L. Zhang, C. Eaton, H.-T. Zhang, and R. Engel-Herbert, *Accessing a Growth Window for SrVO3 Thin Films*, Appl. Phys. Lett. **107**, 143108 (2015).

[122] A. P. Kajdos, D. G. Ouellette, T. A. Cain, and S. Stemmer, *Two-Dimensional Electron Gas in a Modulation-Doped SrTiO3/Sr(Ti, Zr)O3 Heterostructure*, Appl. Phys. Lett. **103**, 082120 (2013).

[123] B. Jalan, J. Cagnon, T. E. Mates, and S. Stemmer, *Analysis of Carbon in SrTiO3 Grown by Hybrid Molecular Beam Epitaxy*, Journal of Vacuum Science & Technology A: Vacuum, Surfaces, and Films **27**, 1365 (2009).

[124] F. C. Frank, J. H. van der Merwe, and N. F. Mott, *One-Dimensional Dislocations. I. Static Theory*, Proceedings of the Royal Society of London. Series A. Mathematical and Physical Sciences **198**, 205 (1949).

[125] W. Hong, H. N. Lee, M. Yoon, H. M. Christen, D. H. Lowndes, Z. Suo, and Z. Zhang, *Persistent Step-Flow Growth of Strained Films on Vicinal Substrates*, Phys. Rev. Lett. **95**, 095501 (2005).

[126] M. Ohring, *Materials Science of Thin Films* (Elsevier, 2001).

[127] R. J. Zeches, M. D. Rossell, J. X. Zhang, A. J. Hatt, Q. He, C.-H. Yang, A. Kumar, C. H. Wang, A. Melville, C. Adamo, G. Sheng, Y.-H. Chu, J. F. Ihlefeld, R. Erni, C. Ederer, V. Gopalan, L. Q. Chen, D. G. Schlom, N. A. Spaldin, L. W. Martin, and R. Ramesh, *A Strain-Driven Morphotropic Phase Boundary in BiFeO3*, Science **326**, 977 (2009).

[128] M. D. Rossell, R. Erni, M. P. Prange, J.-C. Idrobo, W. Luo, R. J. Zeches, S. T. Pantelides, and R. Ramesh, *Atomic Structure of Highly Strained BiFeO3 Thin Films*, Phys. Rev. Lett. **108**, 047601 (2012).

[129] I. C. Infante, S. Lisenkov, B. Dupé, M. Bibes, S. Fusil, E. Jacquet, G. Geneste, S. Petit, A. Courtial, J. Juraszek, L. Bellaiche, A. Barthélémy, and B. Dkhil, *Bridging Multiferroic Phase Transitions by Epitaxial Strain in BiFeO3*, Phys. Rev. Lett. **105**, 057601 (2010).

[130] T. Wang, K. Ganguly, P. Marshall, P. Xu, and B. Jalan, *Critical Thickness and Strain Relaxation in Molecular Beam Epitaxy-Grown SrTiO3 Films*, Applied Physics Letters **103**, 212904 (2013).

[131] C. Adamo, X. Ke, H. Q. Wang, H. L. Xin, T. Heeg, M. E. Hawley, W. Zander, J. Schubert, P. Schiffer, D. A. Muller, L. Maritato, and D. G. Schlom, *Effect of Biaxial Strain on the Electrical and Magnetic Properties of (001) La0.7Sr0.3MnO3 Thin Films*, Applied Physics Letters **95**, 112504 (2009).

[132] C. Ederer and N. A. Spaldin, *Effect of Epitaxial Strain on the Spontaneous Polarization of Thin Film Ferroelectrics*, Phys. Rev. Lett. **95**, 257601 (2005).

[133] J. E. Mahan, K. M. Geib, G. Y. Robinson, and R. G. Long, *A Review of the Geometrical Fundamentals of Reflection High-energy Electron Diffraction with Application to Silicon Surfaces*, Journal of Vacuum Science & Technology A **8**, 3692 (1990).

[134] F. Tang, T. Parker, G.-C. Wang, and T.-M. Lu, *Surface Texture Evolution of Polycrystalline and Nanostructured Films: RHEED Surface Pole Figure Analysis*, J. Phys. D: Appl. Phys. **40**, R427 (2007).

[135] A. P. Kajdos and S. Stemmer, *Surface Reconstructions in Molecular Beam Epitaxy of SrTiO3*, Appl. Phys. Lett. **105**, 191901 (2014).

[136] T. Frey, C. C. Chi, C. C. Tsuei, T. Shaw, and F. Bozso, *Effect of Atomic Oxygen on the Initial Growth Mode in Thin Epitaxial Cuprate Films*, Phys. Rev. B **49**, 3483 (1994).

[137] A. G. Cullis, D. J. Norris, T. Walther, M. A. Migliorato, and M. Hopkinson, *Stranski-Krastanow Transition and Epitaxial Island Growth*, Phys. Rev. B **66**, 081305 (2002).

[138] Y. R. Li, J. L. Li, Y. Zhang, X. H. Wei, X. W. Deng, and X. Z. Liu, *Control of Growth Mode in SrTiO3 Homoepitaxy under 500°C*, Journal of Applied Physics **96**, 1640 (2004).

[139] H. Hertz, *Ueber einen Einfluss des ultravioletten Lichtes auf die electrische Entladung*, Ann. Phys. Chem. **267**, 983 (1887).

[140] S. Thapa, R. Paudel, M. D. Blanchet, P. T. Gemperline, and R. B. Comes, *Probing Surfaces and Interfaces in Complex Oxide Films via in Situ X-Ray Photoelectron Spectroscopy*, Journal of Materials Research **36**, 26 (2021).

[141] N. Fairley, A. Carrick, and N. Fairley, *Recipes for XPS Data Processing* (Acolyte Science, Knutsford, 2005).

[142] D. R. Baer, K. Artyushkova, C. Richard Brundle, J. E. Castle, M. H. Engelhard, K. J. Gaskell, J. T. Grant, R. T. Haasch, M. R. Linford, C. J. Powell, A. G. Shard, P. M. A. Sherwood, and V. S. Smentkowski, *Practical Guides for X-Ray Photoelectron Spectroscopy: First Steps in Planning, Conducting, and Reporting XPS Measurements*, Journal of Vacuum Science & Technology A **37**, 031401 (2019).

[143] A. Segmüller, I. C. Noyan, and V. S. Speriosu, *X-Ray Diffraction Studies of Thin Films and Multilayer Structures*, Progress in Crystal Growth and Characterization **18**, 21 (1989).

[144] G. E. M. Jauncey, *The Scattering of X-Rays and Bragg's Law*, Proc Natl Acad Sci U S A **10**, 57 (1924).

[145] A. A. Bunaciu, E. gabriela Udriștioiu, and H. Y. Aboul-Enein, *X-Ray Diffraction: Instrumentation and Applications*, Critical Reviews in Analytical Chemistry **45**, 289 (2015).

[146] D. K. G. de Boer, A. J. G. Leenaers, and W. W. van den Hoogenhof, *Glancing-Incidence x-Ray Analysis of Thin-Layered Materials: A Review*, X-Ray Spectrometry **24**, 91 (1995).

[147] G. M. McClelland, R. Erlandsson, and S. Chiang, *Atomic Force Microscopy: General Principles and a New Implementation*, in *Review of Progress in Quantitative Nondestructive Evaluation*, edited by D. O. Thompson and D. E. Chimenti (Springer US, Boston, MA, 1987), pp. 1307–1314.

[148] S. Morita, F. J. Giessibl, E. Meyer, and R. Wiesendanger, *Noncontact Atomic Force Microscopy Volume 3 / Edited by Seizo Morita, Franz J. Giessibl, Ernst Meyer, Roland Wiesendanger.*, 1st ed. 2015. (Springer International Publishing : Imprint: Springer, Cham, 2015).

[149] P. Zimmermann, S. Peredkov, P. M. Abdala, S. DeBeer, M. Tromp, C. Müller, and J. A. van Bokhoven, *Modern X-Ray Spectroscopy: XAS and XES in the Laboratory*, Coordination Chemistry Reviews **423**, 213466 (2020).

[150] D. Nečas and P. Klapetek, *Gwyddion: An Open-Source Software for SPM Data Analysis*, Open Physics **10**, 181 (2012).

[151] R. M. Palomino, E. Stavitski, I. Waluyo, Y. K. Chen-Wiegart, M. Abeykoon, J. T. Sadowski, J. A. Rodriguez, A. I. Frenkel, and S. D. Senanayake, *New In-Situ and Operando Facilities for Catalysis Science at NSLS-II: The Deployment of Real-Time, Chemical, and Structure-Sensitive X-Ray Probes*, Synchrotron Radiation News **30**, 30 (2017).

[152] A. Ohtomo and H. Y. Hwang, *A High-Mobility Electron Gas at the LaAlO3/SrTiO3 Heterointerface*, Nature **427**, 423 (2004).

[153] S. A. Chambers, *Understanding the Mechanism of Conductivity at the LaAlO3/SrTiO3(001) Interface*, Surface Science **605**, 1133 (2011).

[154] S. R. Spurgeon, P. V. Sushko, S. A. Chambers, and R. B. Comes, *Dynamic Interface Rearrangement in LaFeO3/n-SrTiO3 Heterojunctions*, Phys. Rev. Materials **1**, 063401 (2017).

[155] M. Nakamura, F. Kagawa, T. Tanigaki, H. S. Park, T. Matsuda, D. Shindo, Y. Tokura, and M. Kawasaki, *Spontaneous Polarization and Bulk Photovoltaic Effect Driven by Polar Discontinuity in LaFeO3/SrTiO3 Heterojunctions*, Phys. Rev. Lett. **116**, 156801 (2016).

[156] R. Comes and S. Chambers, *Interface Structure, Band Alignment, and Built-In Potentials at LaFeO3/n-SrTiO3 Heterojunctions*, Physical Review Letters **117**, 226802 (2016).

[157] K. Nakamura, H. Mashiko, K. Yoshimatsu, and A. Ohtomo, *Impact of Built-in Potential across LaFeO3/SrTiO3 Heterojunctions on Photocatalytic Activity*, Applied Physics Letters **108**, 211605 (2016).

[158] J. H. Haeni, C. D. Theis, and D. G. Schlom, *RHEED Intensity Oscillations for the Stoichiometric Growth of SrTiO3 Thin Films by Reactive Molecular Beam Epitaxy*, Journal of Electroceramics **4**, 385 (2000).

[159] M. Brahlek, A. S. Gupta, J. Lapano, J. Roth, H.-T. Zhang, L. Zhang, R. Haislmaier, and R. Engel-Herbert, *Frontiers in the Growth of Complex Oxide Thin Films: Past, Present, and Future of Hybrid MBE*, Adv. Funct. Mater. **28**, 1702772 (2018).

[160] B. Jalan, R. Engel-Herbert, N. J. Wright, and S. Stemmer, *Growth of High-Quality SrTiO3 Films Using a Hybrid Molecular Beam Epitaxy*, Journal of Vacuum Science and Techology A **27**, 461 (2009).

[161] A. P. Kajdos and S. Stemmer, *Surface Reconstructions in Molecular Beam Epitaxy of SrTiO3*, Applied Physics Letters **105**, 191901 (2014).

[162] B. Jalan, J. Cagnon, T. E. Mates, and S. Stemmer, *Analysis of Carbon in SrTiO3 Grown by Hybrid Molecular Beam Epitaxy*, Journal of Vacuum Science & Technology A: Vacuum, Surfaces, and Films **27**, 1365 (2009).

[163] J. Son, P. Moetakef, B. Jalan, O. Bierwagen, N. J. Wright, R. Engel-Herbert, and S. Stemmer, *Epitaxial SrTiO3 Films with Electron Mobilities Exceeding 30,000 Cm2 V-1 s-1*, Nat Mater **9**, 482 (2010).

[164] B. Jalan, P. Moetakef, and S. Stemmer, *Molecular Beam Epitaxy of SrTiO3 with a Growth Window*, Applied Physics Letters **95**, 032906 (2009).

[165] M. Brahlek, L. Zhang, C. Eaton, H.-T. Zhang, and R. Engel-Herbert, *Accessing a Growth Window for SrVO3 Thin Films*, Appl. Phys. Lett. **107**, 143108 (2015).

[166] A. P. Kajdos, D. G. Ouellette, T. A. Cain, and S. Stemmer, *Two-Dimensional Electron Gas in a Modulation-Doped SrTiO3/Sr(Ti, Zr)O3 Heterostructure*, Applied Physics Letters **103**, 082120 (2013).

[167] B. Jalan, S. J. Allen, G. E. Beltz, P. Moetakef, and S. Stemmer, *Enhancing the Electron Mobility of SrTiO3 with Strain*, Appl. Phys. Lett. **98**, 132102 (2011).

[168] A. Prakash, P. Xu, X. Wu, G. Haugstad, X. Wang, and B. Jalan, *Adsorption-Controlled Growth and the Influence of Stoichiometry on Electronic Transport in Hybrid Molecular Beam Epitaxy-Grown BaSnO3 Films*, J. Mater. Chem. C **5**, 5730 (2017).

[169] J. M. LeBeau, R. Engel-Herbert, B. Jalan, J. Cagnon, P. Moetakef, S. Stemmer, and G. B. Stephenson, *Stoichiometry Optimization of Homoepitaxial Oxide Thin Films Using X-Ray Diffraction*, Applied Physics Letters **95**, 142905 (2009).

[170] J. Roth, E. Arriaga, M. Brahlek, J. Lapano, and R. Engel-Herbert, *Temperature-Dependent Growth Window of CaTiO3 Films Grown by Hybrid Molecular Beam Epitaxy*, Journal of Vacuum Science & Technology A **36**, 020601 (2017).

[171] L. R. Thoutam, J. Yue, P. Xu, and B. Jalan, *Hopping Transport in SrTiO3/Nd_{1-x}TiO3/SrTO3 Heterostructures*, Phys. Rev. Materials **3**, 065006 (2019).

[172] H. Yun, J. Held, A. Prakash, T. Wang, B. Jalan, and K. A. Mkhoyan, *Quantification of La Dopant Level in La:SrSnO3/SrSnO3/BaSnO3 Heterostructures with STEM-EELS*, Microscopy and Microanalysis **25**, 2110 (2019).

[173] P. Moetakef, T. A. Cain, D. G. Ouellette, J. Y. Zhang, D. O. Klenov, A. Janotti, C. G. V. de Walle, S. Rajan, S. J. Allen, and S. Stemmer, *Electrostatic Carrier Doping of GdTiO3/SrTiO3 Interfaces*, Applied Physics Letters **99**, 232116 (2011).

[174] S.-C. Lin, C.-T. Kuo, R. B. Comes, J. E. Rault, J.-P. Rueff, S. Nemšák, A. Taleb, J. B. Kortright, J. Meyer-Ilse, E. Gullikson, P. V. Sushko, S. R. Spurgeon, M. Gehlmann, M. E. Bowden, L. Plucinski, S. A. Chambers, and C. S. Fadley, *Interface Properties and Built-in Potential Profile of a LaCrO3/SrTiO3 Superlattice Determined by Standing-Wave Excited Photoemission Spectroscopy*, Phys. Rev. B **98**, 165124 (2018).

[175] N. Nakagawa, H. Y. Hwang, and D. A. Muller, *Why Some Interfaces Cannot Be Sharp*, Nat Mater **5**, 204 (2006).

[176] S. A. Chambers and P. V. Sushko, *Influence of Crystalline Order and Defects on the Absolute Work Functions and Electron Affinities of TiO2- and SrO-Terminated n-SrTiO3(001)*, Phys. Rev. Materials **3**, 125803 (2019).

[177] A. E. Becerra-Toledo, J. A. Enterkin, D. M. Kienzle, and L. D. Marks, *Water Adsorption on SrTiO3(001): II. Water, Water, Everywhere*, Surface Science **606**, 791 (2012).

[178] M. B. S. Hesselberth, S. J. van der Molen, and J. Aarts, *The Surface Structure of SrTiO3 at High Temperatures under Influence of Oxygen*, Appl. Phys. Lett. **104**, 051609 (2014).

[179] L. Aballe, S. Matencio, M. Foerster, E. Barrena, F. Sánchez, J. Fontcuberta, and C. Ocal, *Instability and Surface Potential Modulation of Self-Patterned (001)SrTiO3 Surfaces*, Chem. Mater. **27**, 6198 (2015).

[180] S. Thapa, R. Paudel, M. D. Blanchet, P. T. Gemperline, and R. B. Comes, *Probing Surfaces and Interfaces in Complex Oxide Films via in Situ X-Ray Photoelectron Spectroscopy*, Journal of Materials Research **36**, 26 (2021).

[181] M. Kawasaki, K. Takahashi, T. Maeda, R. Tsuchiya, M. Shinohara, O. Ishiyama, T. Yonezawa, M. Yoshimoto, and H. Koinuma, *Atomic Control of the SrTiO3 Crystal Surface*, Science **266**, 1540 (1994).

[182] Y.-S. Kim, N. Bansal, and S. Oh, *Crucible Aperture: An Effective Way to Reduce Source Oxidation in Oxide Molecular Beam Epitaxy Process*, Journal of Vacuum Science & Technology A **28**, 600 (2010).

[183] R. K. Vasudevan, A. Tselev, A. P. Baddorf, and S. V. Kalinin, *Big-Data Reflection High Energy Electron Diffraction Analysis for Understanding Epitaxial Film Growth Processes*, ACS Nano **8**, 10899 (2014).

[184] S. R. Provence, S. Thapa, R. Paudel, T. K. Truttmann, A. Prakash, B. Jalan, and R. B. Comes, *Machine Learning Analysis of Perovskite Oxides Grown by Molecular Beam Epitaxy*, Phys. Rev. Materials **4**, 083807 (2020).

[185] R. M. Palomino, E. Stavitski, I. Waluyo, Y. K. Chen-Wiegart, M. Abeykoon, J. T. Sadowski, J. A. Rodriguez, A. I. Frenkel, and S. D. Senanayake, *New In-Situ and Operando Facilities for Catalysis Science at NSLS-II: The Deployment of Real-Time, Chemical, and Structure-Sensitive X-Ray Probes*, Synchrotron Radiation News **30**, 30 (2017).

[186] W. Jin and R. M. Osgood, *Spectroscopic Photoemission and Low-Energy Electron Microscopy Studies of the Surface and Electronic Structure of Two-Dimensional Materials*, Advances in Physics: X **4**, 1688187 (2019).

[187] D. Nečas and P. Klapetek, *Gwyddion: An Open-Source Software for SPM Data Analysis*, Open Physics **10**, 181 (2012).

[188] A. Spinelli, M. A. Torija, C. Liu, C. Jan, and C. Leighton, *Electronic Transport in Doped SrTiO3: Conduction Mechanisms and Potential Applications*, Phys. Rev. B **81**, 155110 (2010).

[189] T. Orvis, H. Kumarasubramanian, M. Surendran, S. Kutagulla, A. Cunniff, and J. Ravichandran, *In Situ Monitoring of Composition and Sensitivity to Growth Parameters of Pulsed Laser Deposition*, ACS Appl. Electron. Mater. **3**, 1422 (2021).

[190] J. H. Lee, G. Luo, I. C. Tung, S. H. Chang, Z. Luo, M. Malshe, M. Gadre, A. Bhattacharya, S. M. Nakhmanson, J. A. Eastman, H. Hong, J. Jellinek, D. Morgan, D. D. Fong, and J. W. Freeland, *Dynamic Layer Rearrangement during Growth of Layered Oxide Films by Molecular Beam Epitaxy*, Nat Mater **13**, 879 (2014).

[191] Y. F. Nie, Y. Zhu, C.-H. Lee, L. F. Kourkoutis, J. A. Mundy, J. Junquera, P. Ghosez, D. J. Baek, S. Sung, X. X. Xi, K. M. Shen, D. A. Muller, and D. G. Schlom, *Atomically Precise Interfaces from Non-Stoichiometric Deposition*, Nat Commun **5**, (2014).

[192] K. A. Stoerzinger, R. Comes, S. R. Spurgeon, S. Thevuthasan, K. Ihm, E. J. Crumlin, and S. A. Chambers, *Influence of LaFeO3 Surface Termination on Water Reactivity*, J. Phys. Chem. Lett. **8**, 1038 (2017).

[193] J. Jobst, L. M. Boers, C. Yin, J. Aarts, R. M. Tromp, and S. J. van der Molen, *Quantifying Work Function Differences Using Low-Energy Electron Microscopy: The Case of Mixed-Terminated Strontium Titanate*, Ultramicroscopy **200**, 43 (2019).

[194] J. Krug, *On the Shape of Wedding Cakes*, J Stat Phys **87**, 505 (1997).

[195] M. Kalff, P. Šmilauer, G. Comsa, and T. Michely, *No Coarsening in Pt(111) Homoepitaxy*, Surface Science **426**, L447 (1999).

[196] R. K. Vasudevan, H. Dixit, A. Tselev, L. Qiao, T. L. Meyer, V. R. Cooper, A. P. Baddorf, H. N. Lee, P. Ganesh, and S. V. Kalinin, *Surface Reconstructions and Modified Surface States in $La_{1-x}Ca_xMnO3$*, Phys. Rev. Materials **2**, 104418 (2018).

[197] A. G. Gianfrancesco, A. Tselev, A. P. Baddorf, S. V. Kalinin, and R. K. Vasudevan, *The Ehrlich–Schwoebel Barrier on an Oxide Surface: A Combined Monte-Carlo Andin Situscanning Tunneling Microscopy Approach*, Nanotechnology **26**, 455705 (2015).

[198] A. Tselev, R. K. Vasudevan, A. G. Gianfrancesco, L. Qiao, T. L. Meyer, H. N. Lee, M. D. Biegalski, A. P. Baddorf, and S. V. Kalinin, *Growth Mode Transition in Complex Oxide Heteroepitaxy: Atomically Resolved Studies*, Crystal Growth & Design **16**, 2708 (2016).

[199] H.-J. Sung, Y. Mochizuki, and F. Oba, *Surface Reconstruction and Band Alignment of Nonmetallic A(II) B(IV)O3 Perovskites*, Phys. Rev. Materials **4**, 044606 (2020).

[200] A. Ohtomo and H. Y. Hwang, *A High-Mobility Electron Gas at the LaAlO3/SrTiO3 Heterointerface*, Nature **427**, 6973 (2004).

[201] D. Oka, Y. Hirose, S. Nakao, T. Fukumura, and T. Hasegawa, *Intrinsic High Electrical Conductivity of Stoichiometric SrNb O 3 Epitaxial Thin Films*, Phys. Rev. B **92**, 205102 (2015).

[202] Z. Zhong and P. Hansmann, *Band Alignment and Charge Transfer in Complex Oxide Interfaces*, Phys. Rev. X **7**, 011023 (2017).

[203] Z. Zhong and P. Hansmann, *Tuning the Work Function in Transition Metal Oxides and Their Heterostructures*, Phys. Rev. B **93**, 235116 (2016).

[204] D. Y. Wan, Y. L. Zhao, Y. Cai, T. C. Asmara, Z. Huang, J. Q. Chen, J. Hong, S. M. Yin, C. T. Nelson, M. R. Motapothula, B. X. Yan, D. Xiang, X. Chi, H. Zheng, W. Chen, R. Xu, Ariando, A. Rusydi, A. M. Minor, M. B. H. Breese, M. Sherburne, M. Asta, Q.-H. Xu, and T. Venkatesan, *Electron Transport and Visible Light Absorption in a Plasmonic Photocatalyst Based on Strontium Niobate*, Nature Communications **8**, 1 (2017).

[205] J. Roth, A. Paul, N. Goldner, A. Pogrebnyakov, K. Agueda, T. Birol, N. Alem, and R. Engel-Herbert, *Sputtered SrxNbO3 as a UV-Transparent Conducting Film*, ACS Appl. Mater. Interfaces **12**, 30520 (2020).

[206] Y. Park, J. Roth, D. Oka, Y. Hirose, T. Hasegawa, A. Paul, A. Pogrebnyakov, V. Gopalan, T. Birol, and R. Engel-Herbert, *SrNbO3 as a Transparent Conductor in the Visible and Ultraviolet Spectra*, Commun Phys **3**, 1 (2020).

[207] M. Mirjolet, M. Kataja, T. K. Hakala, P. Komissinskiy, L. Alff, G. Herranz, and J. Fontcuberta, *Optical Plasmon Excitation in Transparent Conducting SrNbO3 and SrVO3 Thin Films*, Advanced Optical Materials **9**, 2100520 (2021).

[208] J. M. Ok, N. Mohanta, J. Zhang, S. Yoon, S. Okamoto, E. S. Choi, H. Zhou, M. Briggeman, P. Irvin, A. R. Lupini, Y.-Y. Pai, E. Skoropata, C. Sohn, H. Li, H. Miao, B. Lawrie, W. S. Choi, G. Eres, J. Levy, and H. N. Lee, *Correlated Oxide Dirac Semimetal in the Extreme Quantum Limit*, Science Advances **7**, eabf9631 (2021).

[209] J. Zhang, J. M. Ok, Y.-Y. Pai, J. Lapano, E. Skoropata, A. R. Mazza, H. Li, A. Huon, S. Yoon, B. Lawrie, M. Brahlek, T. Z. Ward, G. Eres, H. Miao, and H. N. Lee, *Extremely Large*

Magnetoresistance in High-Mobility SrNbO3/SrTiO3 Heterostructures, Phys. Rev. B **104**, L161404 (2021).

[210] D. Oka, Y. Hirose, S. Nakao, T. Fukumura, and T. Hasegawa, *Intrinsic High Electrical Conductivity of Stoichiometric SrNbO3 Epitaxial Thin Films*, Phys. Rev. B **92**, 205102 (2015).

[211] C. Bigi, P. Orgiani, J. Sławińska, J. Fujii, J. T. Irvine, S. Picozzi, G. Panaccione, I. Vobornik, G. Rossi, D. Payne, and F. Borgatti, *Direct Insight into the Band Structure of SrNbO3*, Phys. Rev. Materials **4**, 025006 (2020).

[212] K. R. Balasubramaniam, Y. Cao, N. Patel, S. Havelia, P. J. Cox, E. C. Devlin, E. P. Yu, B. J. Close, P. M. Woodward, and P. A. Salvador, *Phase and Structural Characterization of Sr2Nb2O7 and SrNbO3 Thin Films Grown via Pulsed Laser Ablation in O2 or N2 Atmospheres*, Journal of Solid State Chemistry **181**, 705 (2008).

[213] C. Lin, A. Posadas, T. Hadamek, and A. A. Demkov, *Final-State Effect on x-Ray Photoelectron Spectrum of Nominally d^1 and n-Doped d^0 Transition-Metal Oxides*, Phys. Rev. B **92**, 035110 (2015).

[214] Z. H. Lim, N. F. Quackenbush, A. N. Penn, M. Chrysler, M. Bowden, Z. Zhu, J. M. Ablett, T.-L. Lee, J. M. LeBeau, J. C. Woicik, P. V. Sushko, S. A. Chambers, and J. H. Ngai, *Charge Transfer and Built-in Electric Fields between a Crystalline Oxide and Silicon*, Phys. Rev. Lett. **123**, 026805 (2019).

[215] C. Chen, Z. Wang, F. Lichtenberg, Y. Ikuhara, and J. G. Bednorz, *Patterning Oxide Nanopillars at the Atomic Scale by Phase Transformation*, Nano Lett. **15**, 6469 (2015).

[216] C. Chen, S. Lv, Z. Wang, K. Akagi, F. Lichtenberg, Y. Ikuhara, and J. G. Bednorz, *Atomic and Electronic Structure of the SrNbO3/SrNbO3.4 Interface*, Appl. Phys. Lett. **105**, 221602 (2014).

[217] P. Xu, Y. Ayino, C. Cheng, V. S. Pribiag, R. B. Comes, P. V. Sushko, S. A. Chambers, and B. Jalan, *Predictive Control over Charge Density in the Two-Dimensional Electron Gas at the Polar-Nonpolar NdTiO3/SrTiO3 Interface*, Phys. Rev. Lett. **117**, 106803 (2016).

[218] R. Aeschlimann, D. Preziosi, P. Scheiderer, M. Sing, S. Valencia, J. Santamaria, C. Luo, H. Ryll, F. Radu, R. Claessen, C. Piamonteze, and M. Bibes, *A Living-Dead Magnetic Layer at the Surface of Ferrimagnetic DyTiO3 Thin Films*, Advanced Materials **30**, 1707489 (2018).

[219] C. Rossel, M. Sousa, C. Marchiori, J. Fompeyrine, D. Webb, D. Caimi, B. Mereu, A. Ispas, J. P. Locquet, H. Siegwart, R. Germann, A. Tapponnier, and K. Babich, *SrHfO3 as Gate Dielectric for Future CMOS Technology*, Microelectronic Engineering **84**, 1869 (2007).

[220] M. Brahlek, A. S. Gupta, J. Lapano, J. Roth, H.-T. Zhang, L. Zhang, R. Haislmaier, and R. Engel-Herbert, *Frontiers in the Growth of Complex Oxide Thin Films: Past, Present, and Future of Hybrid MBE*, Advanced Functional Materials **28**, 1702772 (2018).

[221] C. Eaton, J. A. Moyer, H. M. Alipour, E. D. Grimley, M. Brahlek, J. M. LeBeau, and R. Engel-Herbert, *Growth of SrVO3 Thin Films by Hybrid Molecular Beam Epitaxy*, Journal of Vacuum Science & Technology A **33**, 061504 (2015).

[222] A. Prakash, T. Wang, R. Choudhary, G. Haugstad, W. L. Gladfelter, and B. Jalan, *Precursor Selection in Hybrid Molecular Beam Epitaxy of Alkaline-Earth Stannates*, Journal of Vacuum Science & Technology A **38**, 063410 (2020).

[223] B. Jalan, R. Engel-Herbert, N. J. Wright, and S. Stemmer, *Growth of High-Quality SrTiO3 Films Using a Hybrid Molecular Beam Epitaxy Approach*, Journal of Vacuum Science & Technology A **27**, 461 (2009).

[224] K. Kukli, M. Ritala, M. Leskelä, and R. Lappalainen, *Niobium Oxide Thin Films Grown by Atomic Layer Epitaxy*, Chemical Vapor Deposition **4**, 29 (1998).

[225] T. Blanquart, J. Niinistö, M. Heikkilä, T. Sajavaara, K. Kukli, E. Puukilainen, C. Xu, W. Hunks, M. Ritala, and M. Leskelä, *Evaluation and Comparison of Novel Precursors for Atomic Layer Deposition of Nb_2O_5 Thin Films*, Chem. Mater. **24**, 975 (2012).

[226] S. B. Basuvalingam, B. Macco, H. C. M. Knoops, J. Melskens, W. M. M. (Erwin) Kessels, and A. A. Bol, *Comparison of Thermal and Plasma-Enhanced Atomic Layer Deposition of Niobium Oxide Thin Films*, Journal of Vacuum Science & Technology A **36**, 041503 (2018).

[227] J. P. Perdew, K. Burke, and M. Ernzerhof, *Generalized Gradient Approximation Made Simple*, Phys. Rev. Lett. **77**, 3865 (1996).

[228] P. E. Blöchl, *Projector Augmented-Wave Method*, Phys. Rev. B **50**, 17953 (1994).

[229] P. Giannozzi, O. Andreussi, T. Brumme, O. Bunau, M. B. Nardelli, M. Calandra, R. Car, C. Cavazzoni, D. Ceresoli, M. Cococcioni, N. Colonna, I. Carnimeo, A. D. Corso, S. de Gironcoli, P. Delugas, R. A. DiStasio, A. Ferretti, A. Floris, G. Fratesi, G. Fugallo, R. Gebauer, U. Gerstmann, F. Giustino, T. Gorni, J. Jia, M. Kawamura, H.-Y. Ko, A. Kokalj, E. Küçükbenli, M. Lazzeri, M. Marsili, N. Marzari, F. Mauri, N. L. Nguyen, H.-V. Nguyen, A. Otero-de-la-Roza, L. Paulatto, S. Poncé, D. Rocca, R. Sabatini, B. Santra, M. Schlipf, A. P. Seitsonen, A. Smogunov, I. Timrov, T. Thonhauser, P. Umari, N. Vast, X. Wu, and S. Baroni, *Advanced Capabilities for Materials Modelling with Quantum ESPRESSO*, J. Phys.: Condens. Matter **29**, 465901 (2017).

[230] R. Engel-Herbert, Y. Hwang, and S. Stemmer, *Quantification of Trap Densities at Dielectric/III–V Semiconductor Interfaces*, Appl. Phys. Lett. **97**, 062905 (2010).

[231] Y. Wang, R. B. Comes, S. Kittiwatanakul, S. A. Wolf, and J. Lu, *Epitaxial Niobium Dioxide Thin Films by Reactive-Biased Target Ion Beam Deposition*, Journal of Vacuum Science & Technology A **33**, 021516 (2015).

[232] C. Marini, O. Noked, I. Kantor, B. Joseph, O. Mathon, R. Shuker, B. J. Kennedy, S. Pascarelli, and E. Sterer, *Nb K-Edge x-Ray Absorption Investigation of the Pressure Induced*

Amorphization in A-Site Deficient Double Perovskite La $_{1/3}$ NbO $_{3}$, J. Phys.: Condens. Matter **28**, 045401 (2016).

[233] Y. Chen and R. J. Green, *Progress and Perspectives of Atomically Engineered Perovskite Oxide Interfaces for Electronics and Electrocatalysts*, Advanced Materials Interfaces **6**, 1900547 (2019).

[234] J. Mannhart, D. H. A. Blank, H. Y. Hwang, A. J. Millis, and J.-M. Triscone, *Two-Dimensional Electron Gases at Oxide Interfaces*, MRS Bulletin **33**, 1027 (2008).

[235] X.-L. Shi, H. Wu, Q. Liu, W. Zhou, S. Lu, Z. Shao, M. Dargusch, and Z.-G. Chen, *SrTiO3-Based Thermoelectrics: Progress and Challenges*, Nano Energy **78**, 105195 (2020).

[236] J.-J. Zhou, O. Hellman, and M. Bernardi, *Electron-Phonon Scattering in the Presence of Soft Modes and Electron Mobility in SrTiO3 Perovskite from First Principles*, Phys. Rev. Lett. **121**, 226603 (2018).

[237] Z. Lebens-Higgins, D. O. Scanlon, H. Paik, S. Sallis, Y. Nie, M. Uchida, N. F. Quackenbush, M. J. Wahila, G. E. Sterbinsky, D. A. Arena, J. C. Woicik, D. G. Schlom, and L. F. J. Piper, *Direct Observation of Electrostatically Driven Band Gap Renormalization in a Degenerate Perovskite Transparent Conducting Oxide*, Phys. Rev. Lett. **116**, 027602 (2016).

[238] S. Sallis, D. O. Scanlon, S. C. Chae, N. F. Quackenbush, D. A. Fischer, J. C. Woicik, J.-H. Guo, S. W. Cheong, and L. F. J. Piper, *La-Doped BaSnO3—Degenerate Perovskite Transparent Conducting Oxide: Evidence from Synchrotron x-Ray Spectroscopy*, Appl. Phys. Lett. **103**, 042105 (2013).

[239] A. Prakash, P. Xu, A. Faghaninia, S. Shukla, J. W. Ager Iii, C. S. Lo, and B. Jalan, *Wide Bandgap $BaSnO_3$ Films with Room Temperature Conductivity Exceeding 10^4 S Cm^{-1}*, Nature Communications **8**, 15167 (2017).

[240] H. Paik, Z. Chen, E. Lochocki, A. Seidner H., A. Verma, N. Tanen, J. Park, M. Uchida, S. Shang, B.-C. Zhou, M. Brützam, R. Uecker, Z.-K. Liu, D. Jena, K. M. Shen, D. A. Muller, and D. G. Schlom, *Adsorption-Controlled Growth of La-Doped BaSnO3 by Molecular-Beam Epitaxy*, APL Materials **5**, 116107 (2017).

[241] K. Krishnaswamy, L. Bjaalie, B. Himmetoglu, A. Janotti, L. Gordon, and C. G. Van de Walle, *BaSnO3 as a Channel Material in Perovskite Oxide Heterostructures*, Appl. Phys. Lett. **108**, 083501 (2016).

[242] K. Krishnaswamy, B. Himmetoglu, Y. Kang, A. Janotti, and C. G. Van de Walle, *First-Principles Analysis of Electron Transport in BaSnO3*, Phys. Rev. B **95**, 205202 (2017).

[243] S. Kc, A. J. E. Rowberg, L. Weston, and C. G. Van de Walle, *First-Principles Study of Antisite Defects in Perovskite Stannates*, Journal of Applied Physics **126**, 195701 (2019).

[244] Y. Kim, S. Kim, H. Cho, Y. M. Kim, H. Ohta, and K. Char, *Transport Properties of the LaInO3/BaSnO3 Interface Analyzed by Poisson-Schrödinger Equation*, Phys. Rev. Applied **17**, 014031 (2022).

[245] J. Shin, Y. M. Kim, C. Park, and K. Char, *Remote Doping of the Two-Dimensional-Electron-Gas State at the LaInO3/BaSnO3 Polar Interface*, Phys. Rev. Applied **13**, 064066 (2020).

[246] H. Cho, D. Song, Y. Kim, B. Kim, and K. Char, *High-Mobility Field-Effect Transistor Using 2-Dimensional Electron Gas at the LaScO3/BaSnO3 Interface*, ACS Appl. Electron. Mater. **4**, 356 (2022).

[247] T. R. Paudel and E. Y. Tsymbal, *Prediction of a Mobile Two-Dimensional Electron Gas at the LaScO3/BaSnO3(001) Interface*, Phys. Rev. B **96**, 245423 (2017).

[248] A. Prakash, N. F. Quackenbush, H. Yun, J. Held, T. Wang, T. Truttmann, J. M. Ablett, C. Weiland, T.-L. Lee, J. C. Woicik, K. A. Mkhoyan, and B. Jalan, *Separating Electrons and Donors in BaSnO3 via Band Engineering*, Nano Lett. **19**, 8920 (2019).

[249] J. John, S. R. Chalana, R. Prabhu, and V. P. Mahadevan Pillai, *Effect of Oxygen Pressure on the Structural and Optical Properties of BaSnO3 Films Prepared by Pulsed Laser Deposition Method*, Appl. Phys. A **125**, 155 (2019).

[250] M. L. Lee, E. A. Fitzgerald, M. T. Bulsara, M. T. Currie, and A. Lochtefeld, *Strained Si, SiGe, and Ge Channels for High-Mobility Metal-Oxide-Semiconductor Field-Effect Transistors*, Journal of Applied Physics **97**, 011101 (2005).

[251] R. J. Terry, N. Combs, C. D. McMillen, S. Stemmer, and J. W. Kolis, *Hydrothermal Growth of BaSnO3 Single Crystals for Wide Bandgap Applications*, Journal of Crystal Growth **536**, 125529 (2020).

[252] C. Guguschev, D. Klimm, M. Brützam, T. M. Gesing, M. Gogolin, H. Paik, A. Dittmar, V. J. Fratello, and D. G. Schlom, *Single Crystal Growth and Characterization of Ba2ScNbO6 – A Novel Substrate for BaSnO3 Films*, Journal of Crystal Growth **528**, 125263 (2019).

[253] K. Ganguly, P. Ambwani, P. Xu, J. S. Jeong, K. A. Mkhoyan, C. Leighton, and B. Jalan, *Structure and Transport in High Pressure Oxygen Sputter-Deposited BaSnO3−δ*, APL Materials **3**, 062509 (2015).

[254] K. Krishnaswamy, B. Himmetoglu, Y. Kang, A. Janotti, and C. G. Van de Walle, *First-Principles Analysis of Electron Transport in BaSnO 3*, Phys. Rev. B **95**, 205202 (2017).

[255] S. Mahatara, S. Thapa, R. B. Comes, and B. Kiefer, *High Mobility Two-Dimensional Electron Gas at the BaSnO3/SrNbO3 Interface*, In Preparation (n.d.).

[256] L. Weston, L. Bjaalie, K. Krishnaswamy, and C. G. Van de Walle, *Origins of n-Type Doping Difficulties in Perovskite Stannates*, Phys. Rev. B **97**, 054112 (2018).

Appendices

Appendix A

Correlating surface stoichiometry and termination in $SrTiO_3$ films grown by hybrid molecular beam epitaxy

Suresh Thapa[1], Sydney R. Provence[1], Devin Jessup[2], Jason Lapano[3], Matthew Brahlek[3], Jerzy T. Sadowski[4], Petra Reinke[2], Wencan Jin[1], and Ryan B. Comes[1,a]

[1]Physics Department, Auburn University, Auburn, AL, 36849, USA

[2]Department of Materials Science and Engineering, University of Virginia, Charlottesville, VA 22904

[3]Materials Science and Technology Division, Oak Ridge National Laboratory, Oak Ridge, TN, 37830

[4]Center for Functional Nanomaterials, Brookhaven National Laboratory, Upton, NY, 11973

[a)] Electronic mail: ryan.comes@auburn.edu

Supporting Information

I. Ti 2*p*:Sr 3*d* peak area ratio

In order to understand how much shift in Ti 2*p* : Sr 3*d* peak area ratio could occur from experimental result if the film has completely either terminations, a simple theoretical model was created. In this model, an intensity *I*(*z)* of SrO and TiO_2 layer in a STO film was calculated by assuming complete ($A_{SrO/TiO_2} = 1$) SrO and TiO_2 termination in each half a unit cell STO film depth (*z*) alternately up-to 5 nm. For the x-ray incident angle (θ) of 45°and wavelength (λ) 1.5 nm, all the calculated intensities

are summed and evaluated the ratio of $I_{TiO_2}(z)$ to $I_{SrO}(z)$. In comparison to the STO substrate the area ratio shifts up-to ~20% depending upon the type of termination.

$$I(z) = A_{SrO/TiO_2} e^{-z/\lambda cos\theta} \quad (1)$$

II. Carbon contamination

Figure S1 shows the core level XPS scan of a representative film with photoelectrons takeoff angle at 45°. The C 1s peak is negligibly small in comparison with the nearby Sr 3p peaks.

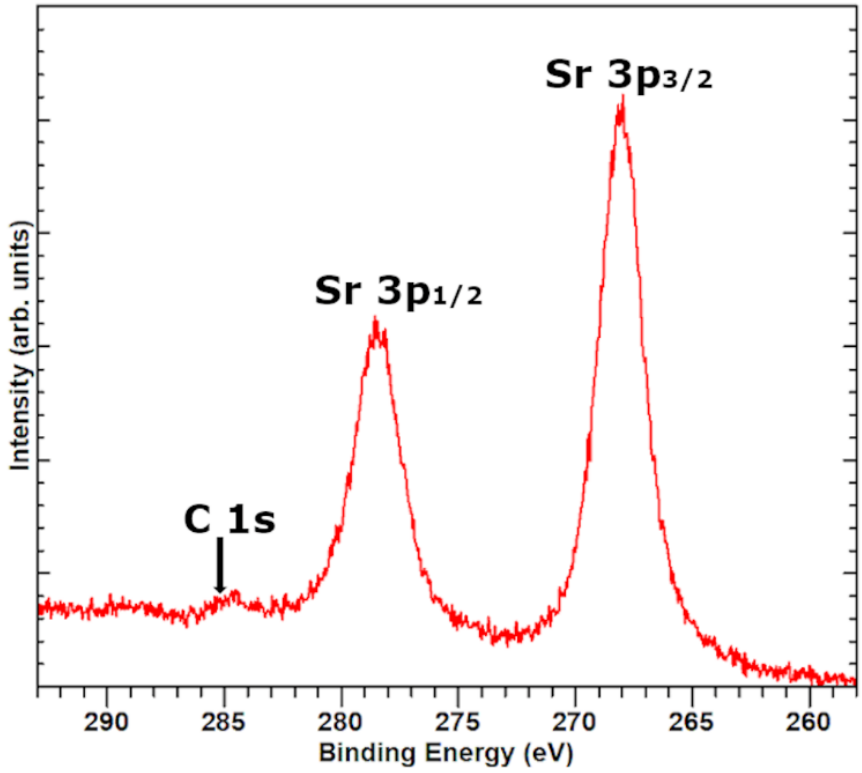

Figure S1: C1s core level with x-ray incident angle 45°.

III. Principal Component Analysis

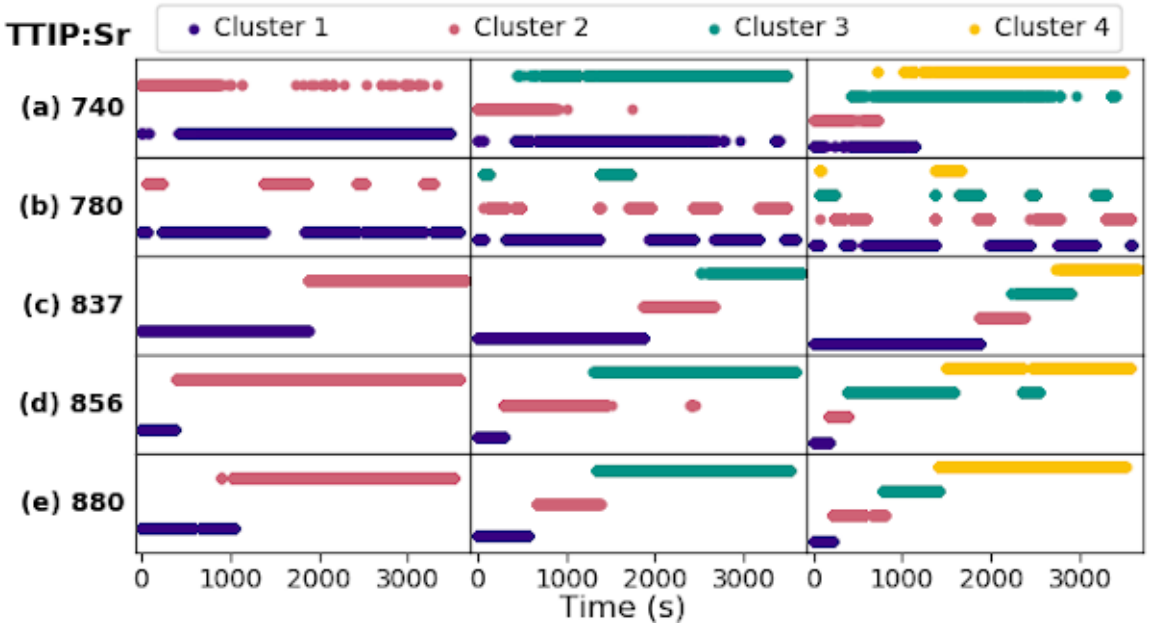

Figure S2: K-means clustering for samples (a)-(e) using 2-4 clusters.

Figure S2 shows K-means clustering for the 5 samples, with clear trends between the stoichiometric samples (740 and 780) and those that are non-stoichiometric (837, 856, and 880). The stoichiometric samples exhibit minimal changes to the RHEED pattern during growth, with the only apparent change in the clustering occurring in Sample 740 after transitioning to the step-flow growth regime. Meanwhile, the off-stoichiometric samples have abrupt changes in clustering, which suggests an accumulation of defects over the course of the growth due to excess Ti flux.

IV. RHEED and XPS data for sample 740 on Nb-doped STO

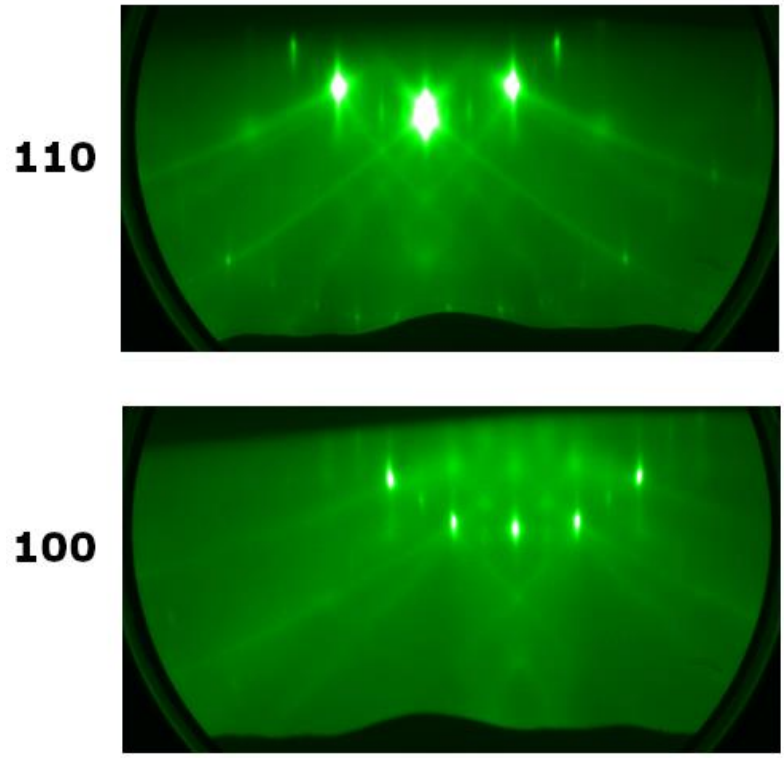

Figure S3: RHEED patterns along (110) and (100) azimuth for STO film on Nb doped STO substrate.

Figure S3 is a RHEED pattern for the sample grown on the Nb-doped STO substrate with the same nominal stoichiometry and cation ratio (~0.6) from the XPS analysis as Sample 740. Surface reconstructions are more visible compared to 740 sample along either azimuth. Reconstruction peaks indicate that a c(2×2) reconstruction and (2×2) reconstruction are present, in agreement with the observations by LEED and LEEM.

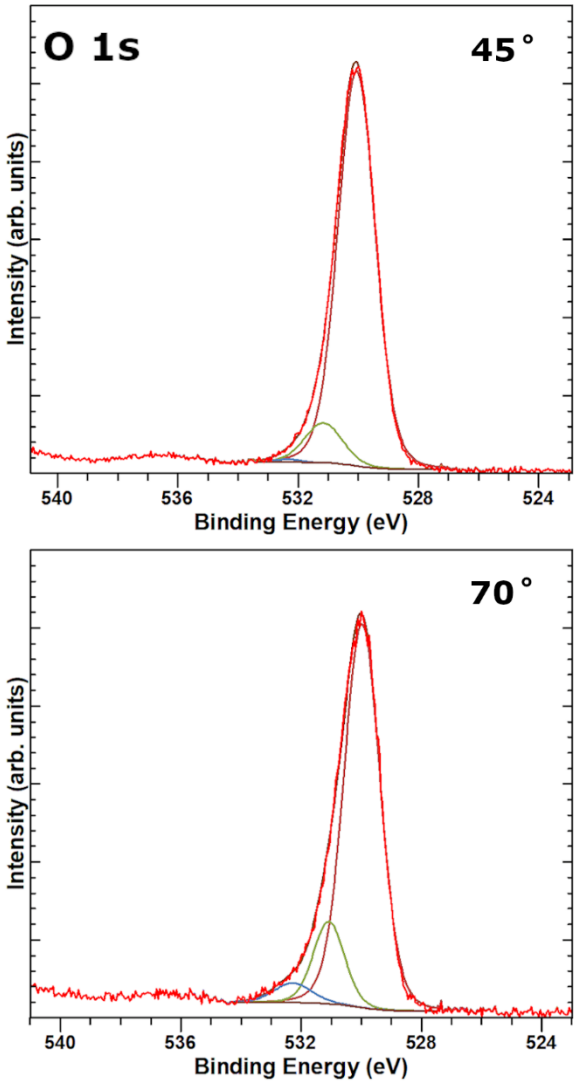

Figure S4: O1s core level with x-ray incident angle 45° and 70° for STO film on Nb doped STO substrate.

Figure S4 shows the O 1s the equivalent deconvolution with constraints as described in the main text for the LEEM/LEED sample grown with the same nominal stoichiometry and cation ratio (~0.6) from the XPS analysis as Sample 740 on a Nb-doped STO substrate. As with Samples 740 and 780, this deconvolution shows that the surface oxygen peak at 532.3 eV is more pronounced by relatively surface sensitive orientation of the XPS measurement. The magnitude of the surface

component is nearly same as that for the 740 sample. A comparable cation area ratio along with O 1s peak deconvolution reflects same surface chemistry as 740 sample.

IV. RHEED and XPS data for SrO-terminated STO

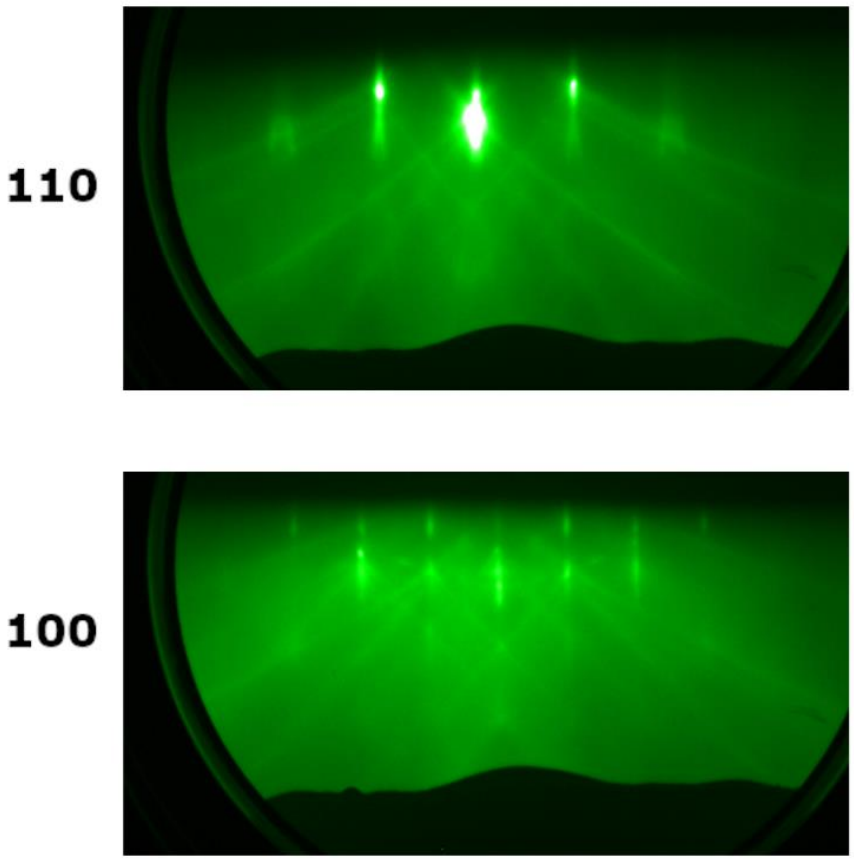

Figure S5: RHEED patterns along (110) and (100) azimuth for SrO-terminated STO.

Figure S5 is a RHEED pattern for the SrO terminated STO substrate.

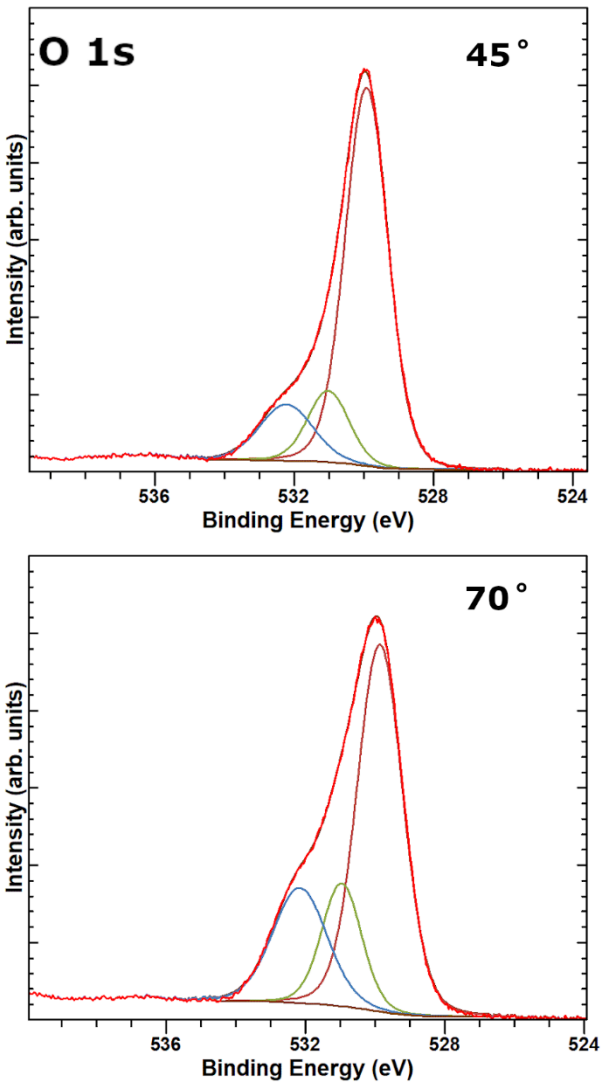

Figure S6: O1s core level with x-ray incident angle 45° and 70° for SrO-terminated STO.

Figure S6 shows the O 1s the equivalent deconvolution with constraints as described in the main text for the SrO-terminated STO substrate. As with Samples 740 and 780, this deconvolution shows that the surface oxygen peak at 532.3 eV is more pronounced by relatively surface sensitive orientation of the XPS measurement. A comparable cation area ratio along with O 1s peak deconvolution reflects same surface chemistry as 740 sample.

V. Angle-resolved XPS Single Crystal Reference Data

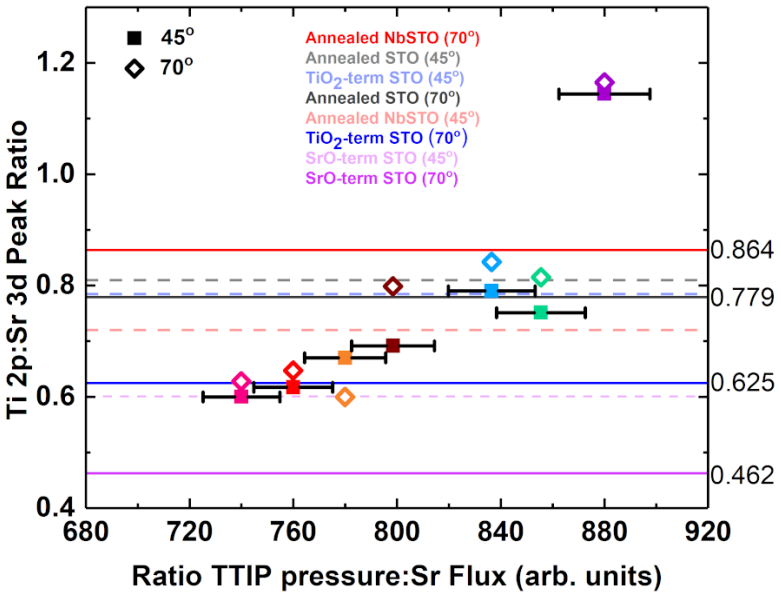

Figure S7: Replication of Figure 5.2a including angle-resolved data for single crystal substrates.

VI. Ti 2*p* XPS Comparison

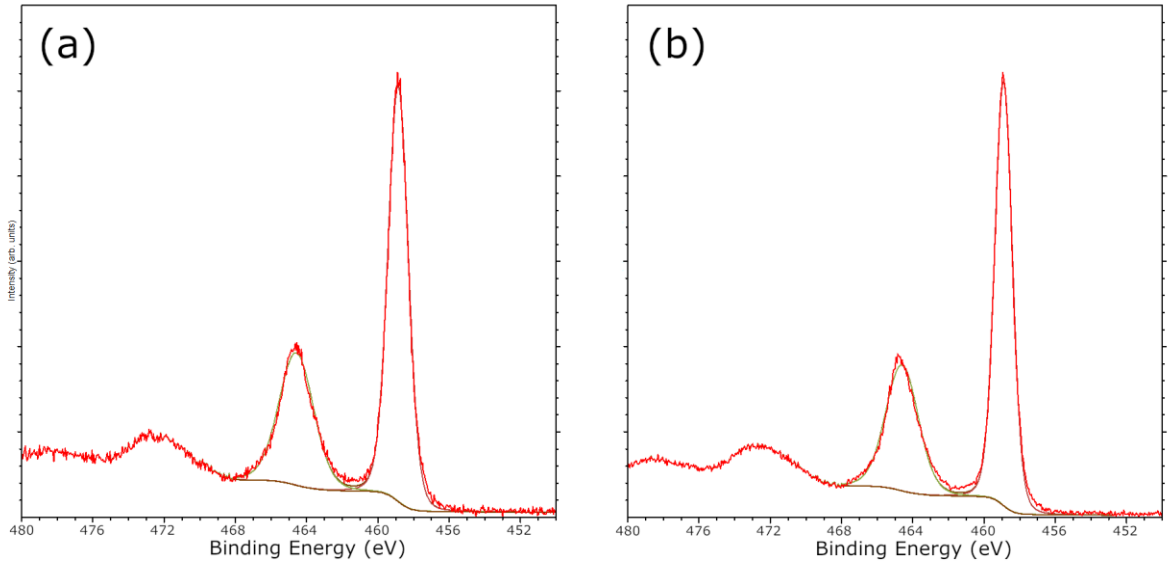

Figure S8: Comparison of Ti 2*p* spectra for (a) Sample 798 and (b) Sample 740.

Figure S8 shows Ti 2*p* spectra for the off-stoichiometric Sample 798 and stoichiometric Sample 740. Fits to the data by assuming only a Ti^{4+} valence for both samples are essentially identical, suggesting that differences in oxygen vacancy concentrations between samples are not responsible for the differences in XRD patterns. Both spectra were acquired at 45° electron emission angles.

VII. $SrTiO_3$ Films Atomic Force Microscopy

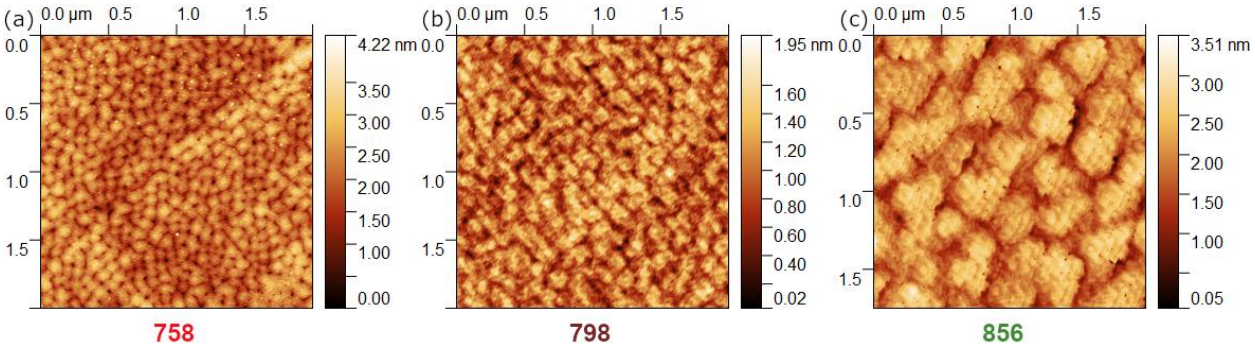

Figure S9: Atomic force microscopy images of $SrTiO_3$ homoepitaxial films with flux ratios (a) 758; (b) 798; (c) 856.

Figure S9 shows atomic force microscopy images of selected $SrTiO_3$ homoepitaxial films with varying cation flux ratios. The films exhibit similar wedding cake morphologies, albeit with slightly feature size. The morphology is analogous to what is observed by scanning tunneling microscopy reported in the main text.

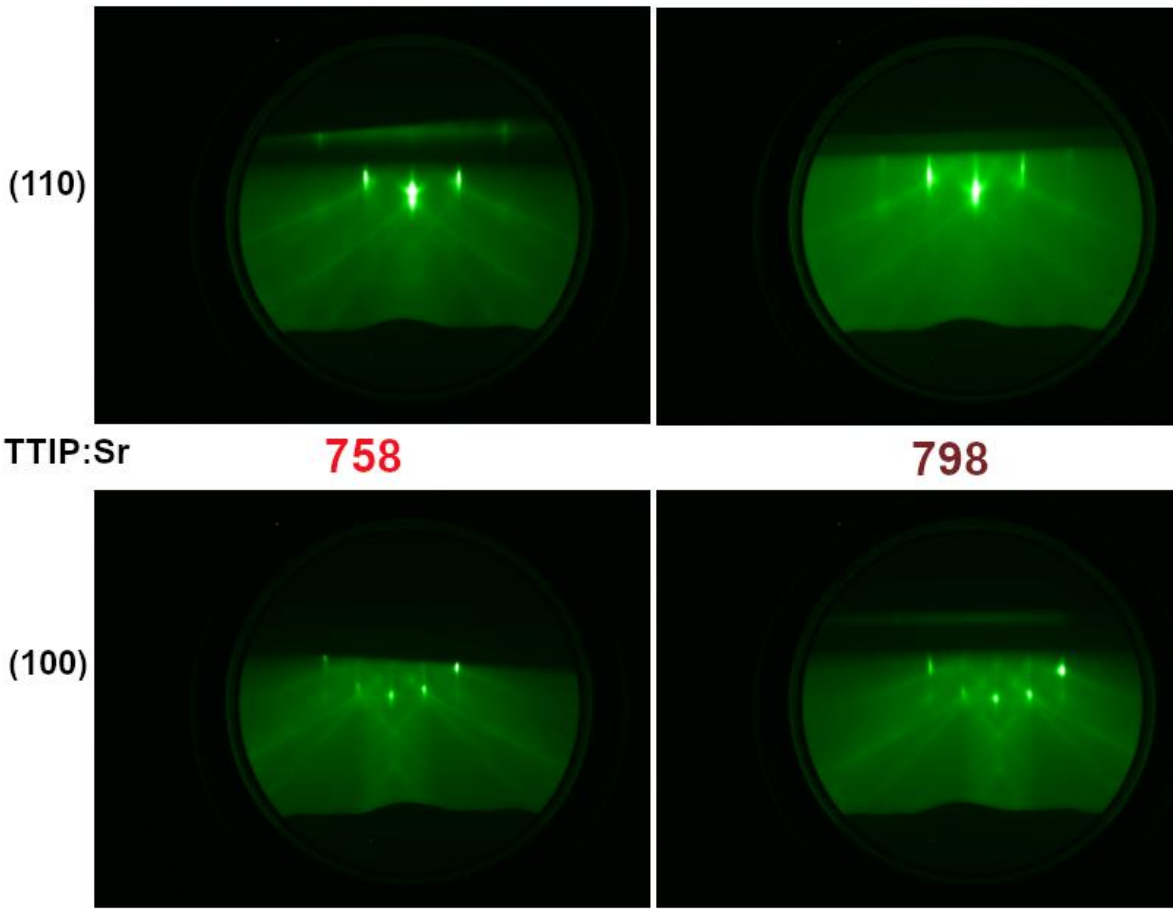

Figure S10: RHEED patterns along (110) and (100) azimuth for samples 758 and 798.

Figure S10 shows the RHEED patterns for sample 758 and 798.

Appendix B

Surface Stability of $SrNbO_{3+\delta}$ Grown by Hybrid Molecular Beam Epitaxy

Suresh Thapa[1], Sydney Provence[1], Steve M. Heald[2], Marcelo A. Kuroda[1], and Ryan B. Comes[1]

[1]Department of Physics, Auburn University, Auburn, AL 36830, USA

[2]Advanced Photon Source, Argonne National Laboratory, Argonne, IL 60439, USA

Supplemental Information:

Table S1: Position constraints for Nb3*d* core level deconvolution

Sample ID	Position Constraints (eV)			
	Nb 5+ Spin-orbit splitting (black/brown)	Nb 4+ Spin-orbit splitting (red/orange)	Hf 4+ (grey/green)	Hf satellite peaks relative to primary Hf 4+ (blue/violet)
Uncapped $SrNbO_3$	2.7	2.65	-	-
Capped samples	3.05	3.4	Unconstrained	7.0

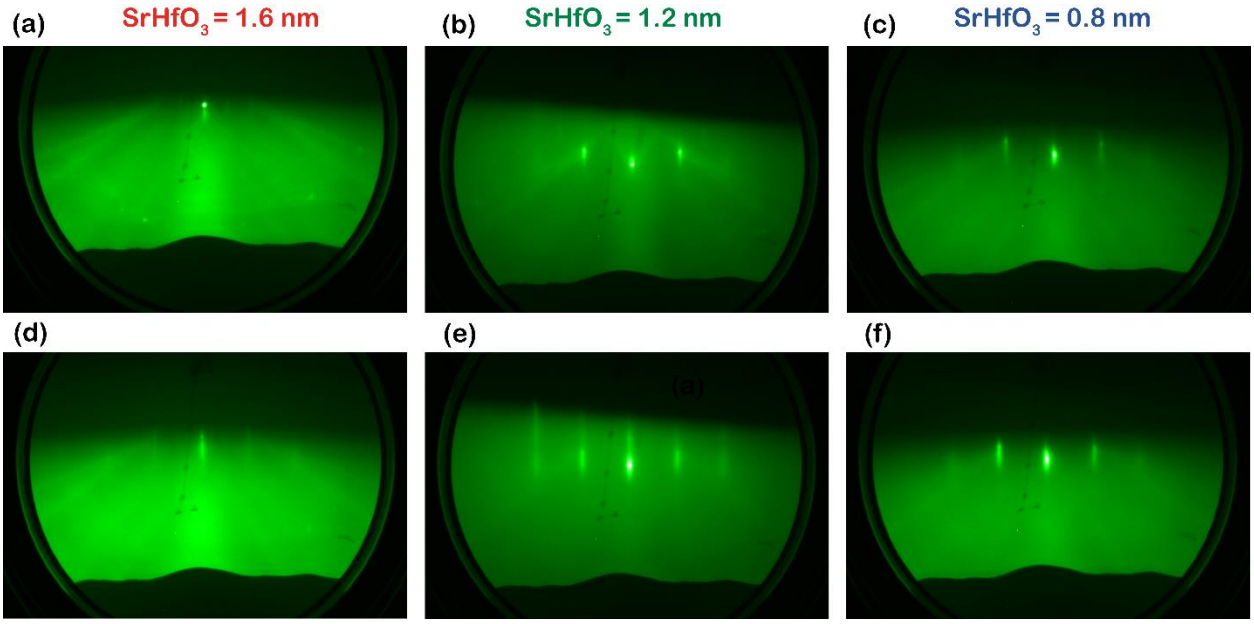

Figure S1: RHEED images along 110 azimuths during hot for $SrNbO_3$ films before (top) and after (bottom) $SrHfO_3$ capping of (left) 2 unit cells, (middle) 3 unit cells, and (right) 4 unit cells.

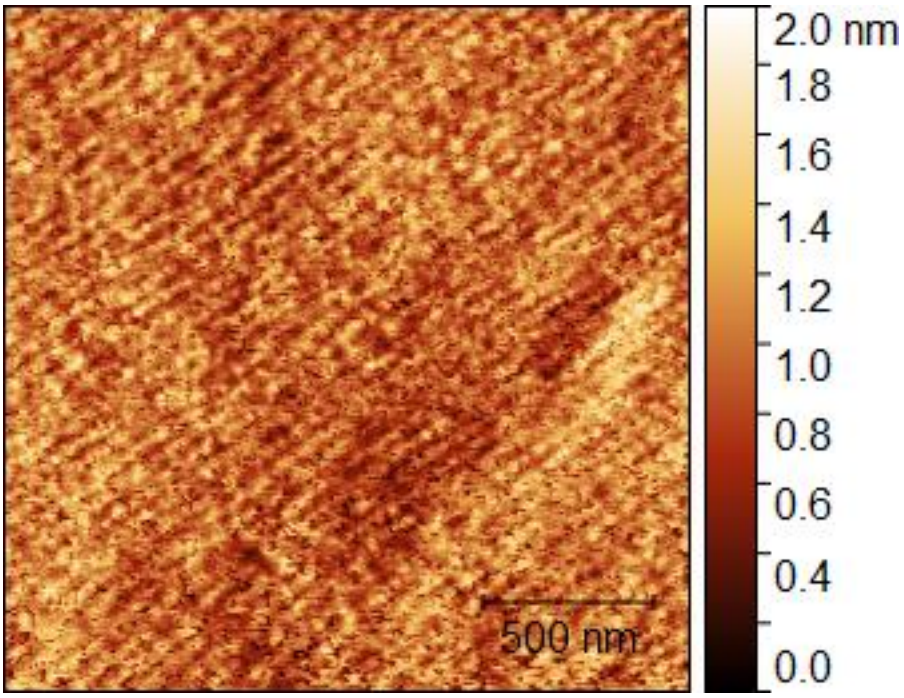

Figure S2: AFM topography of $SrHfO_3$ film

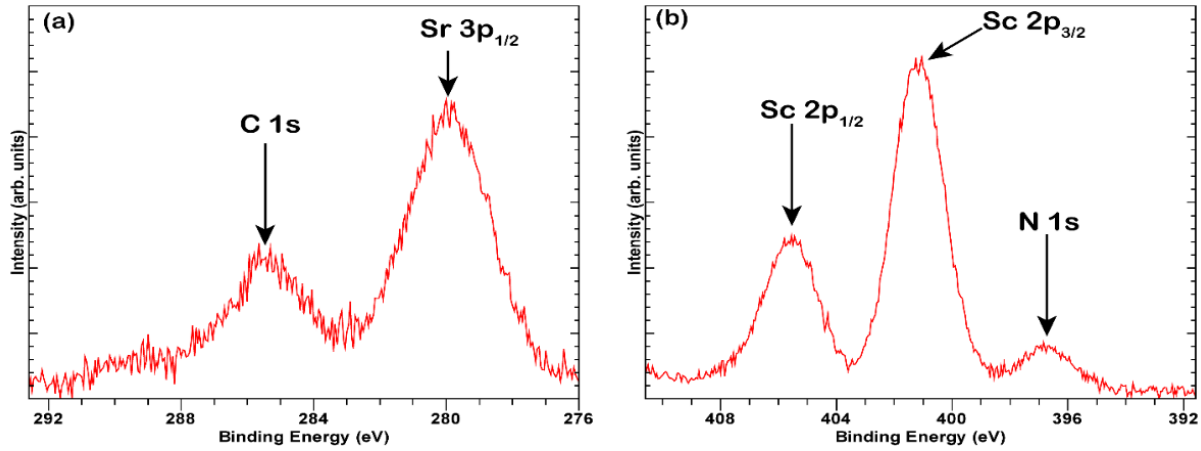

Figure S3: (a) C 1s and (b) N 1s on uncapped SNO sample

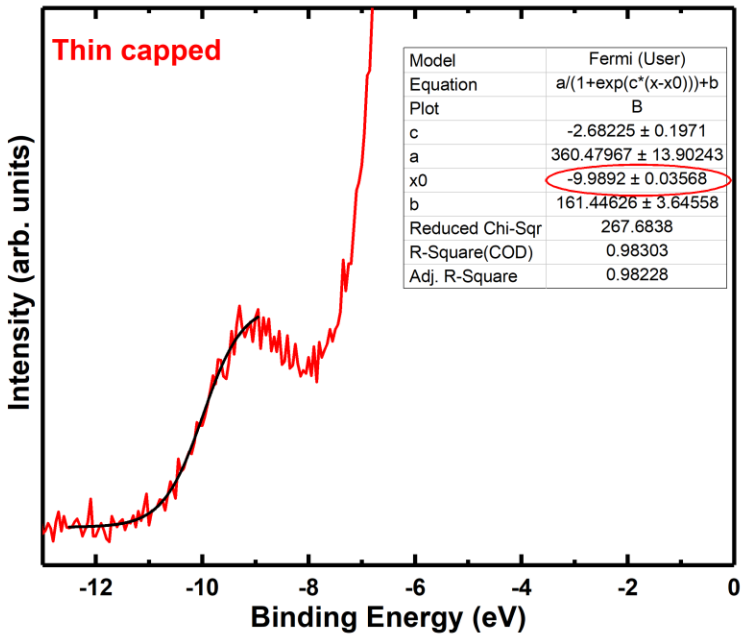

Figure S4: XPS valence band spectra of a thin capped sample fitted with Fermi-Dirac function

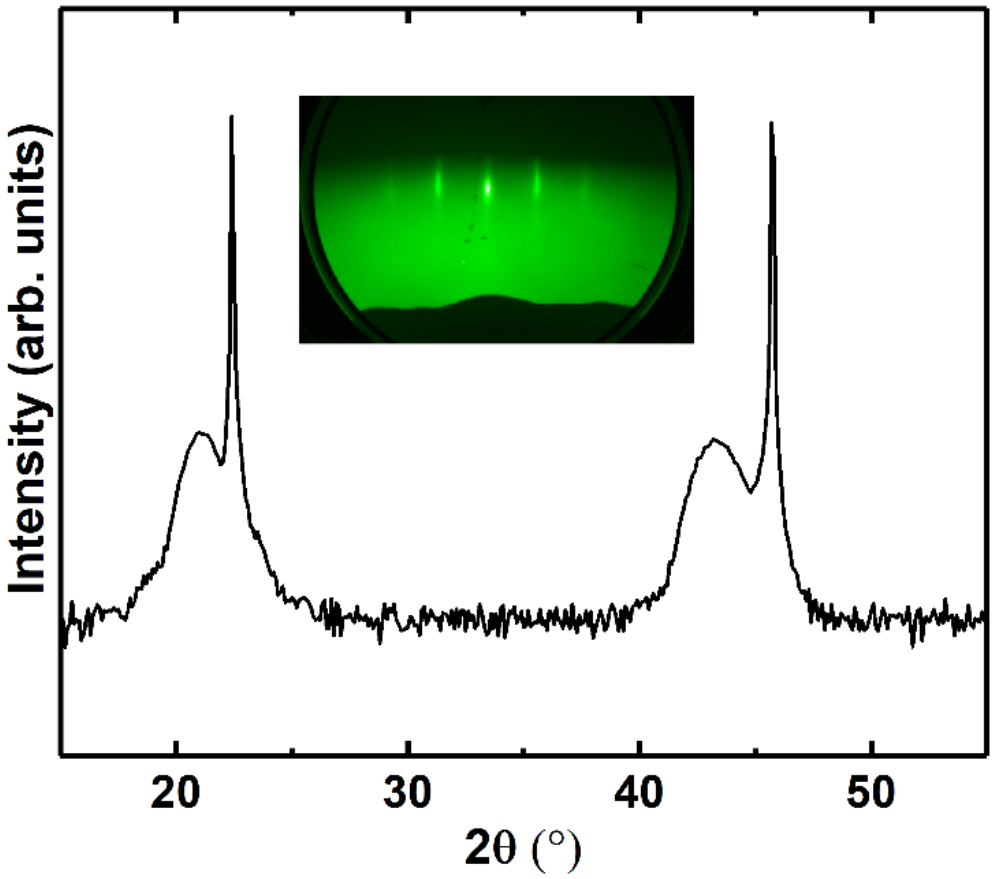

Figure S5: XRD of $SrHfO_3$ on $GdScO_3$ and RHEED (inset)